國立交通大學

物理研究所

博士論文

大亞灣反應堆微中子實驗
利用慢信號中子被氫捕獲訊號測量微中子振盪混合角

The Measurement of Mixing Angle θ_{13} from Delayed Neutron Capture on Hydrogen in The Daya Bay Reactor Neutrino Experiment

研究生：胡貝禎

指導教授：林貴林 教授
王 喆 副教授

中華民國一零三年六月

大亞灣反應堆微中子實驗
利用慢信號中子被氫捕獲訊號測量微中子振盪混合角

The Measurement of Mixing Angle θ_{13} from Delayed Neutron Capture on Hydrogen in The Daya Bay Reactor Neutrino Experiment

研究生：胡貝禎
指導教授：林貴林
王喆

Student: Bei-Zhen Hu
Advisor: Guey-Lin Lin
Zhe Wang

國立交通大學
物理研究所
博士論文

A Thesis
Submitted to Institute of Physics
National Chiao Tung University
in Partial Fulfillment of the Requirements
for the Degree of
Doctor in Philosophy
in
Physics
June, 2014
Hsinchu, Taiwan

中華民國一零三年六月

大亞灣反應堆微中子實驗
利用慢信號中子被氫捕獲訊號測量微中子振盪混合角

學生：胡貝禎　　　　　　　　　　指導教授：林貴林
王　喆

國立交通大學物理研究所

摘　要

目前已知的微中子有三種類型：電子微中子、緲子微中子和濤子微中子。微中子在傳播的過程中會由一類轉變成另外兩類，此現象稱爲微中子震盪（neutrino oscillation）現象。

微中子弱作用態(weak interaction state)是質量本征態（mass eigenstate）和矩陣（unitary matrix）的線性組合。這個矩陣帶有四個參數分別是三個混合角（mixing angle− θ_{12}，θ_{23}，θ_{13}）以及一個CP破壞相位角(CP-violating phase, δ_{CP})。微中子震盪實驗目標是測量這四個參數以及另外兩個與微中子質量相關的參數（mass-squared differences, Δm^2_{32}，Δm^2_{21}）。一般預測，混合角 θ_{13} 非常小，能夠精準的測量混合角 θ_{13} 在物理的研究上是非常重要的，它可幫助我們了解混合矩陣以及測量CP破壞相位角，進而解開現今物理未知的領域！

反應堆微中子實驗是利用反 β 衰變（Inverse-beta decay, IBD）來量測微中子的事例。反 β 衰變（Inverse-beta decay, IBD）的過程是一個反電子微中子（electron anti-neutrino）與探測器中的質子反應產生一個正電子 (positron, e^+) 與一個中子。正電子在極短時間內透過正負電子的煙滅效應（annihilation process）放出兩道伽瑪（γ），此信號是判別微中子的快信號(prompt signal)。另外一方面，中子可被氫或釓捕獲放出另一道伽瑪，能量分別爲 2.2 MeV 或 8 MeV ，此信號則爲慢信號(delayed signal)。

大亞灣反應堆微中子實驗是爲了測量混合角 θ_{13} 而設計的，目標是測量精準度達到 0.01 或是 $\sin^2 2\theta_{13}$ 在百分之九十的信心水準之上。在二零一二年三月期間，大亞灣合作組發表了混合角 θ_{13} 的測量結果：$\sin^2 2\theta_{13} = 0.092 \pm 0.016(\text{stat.}) \pm 0.005(\text{syst.})$，利用釓捕獲的訊號以及 55 天的數據分析而達到 5.2的標準偏差，因此可以排除 θ_{13} 爲零的可能性，是一項重要的結果！同年六月，大亞灣再度更新測量結果 $\sin^2 2\theta_{13} = 0.089 \pm 0.010(stat.) \pm 0.005(syst.)$。

本篇論文，利用中子被氫捕獲的訊號進行混合角 θ_{13} 的測量。此方法有別於釓捕獲的分析，由於中子被氫捕獲時所產生的能量較低，因此容易受到許多低能量的輻射影響；其次，中子被氫捕獲所需的時間較長，因此也引入了不少雜訊。上述的種種因素，爲此分析增加了不少挑戰！爲解決這些因素，我們使用許多不同於釓捕獲分析的方法。目前，氫捕獲的分析結果是 $\sin^2 2\theta_{13} = 0.083 \pm 0.018$，結合兩種分析方式，混合角則爲 $\sin^2 2\theta_{13} = 0.089 \pm 0.008$。

The Measurement of Mixing Angle θ_{13} from Delayed Neutron Capture on Hydrogen in The Daya Bay Reactor Neutrino Experiment

Student: Bei-Zhen Hu
Advisor: Guey-Lin Lin
Zhe Wang

Submitted to Institute of Physics
National Chiao Tung University

ABSTRACT

The neutrino oscillation arises because the neutrino weak interaction states are the linear combination of the mass eigenstates with a unitary matrix. The matrix contains four parameters, three mixing angles $(\theta_{12}, \theta_{23}, \theta_{13})$ and a CP-violating phase δ_{CP}. Neutrino oscillation experiments are expected to determine these parameters and two mass-squared differences Δm^2_{32} and Δm^2_{21}. θ_{13} was predicted to be very small. The precision measurement of θ_{13} is very important for the understanding of neutrino mixing matrix and the measurement of the CP-violating phase δ_{CP}.

The reactor neutrino measurement is performed via the inverse-beta decay (IBD) process, $\overline{\nu_e} + p \to n + p^+$. The positron-electron annihilation emits gammas, which is the prompt signal in the IBD process. The delayed signal is from neutron capture on Gadolinium or Hydrogen and emits gamma with approximately 8 MeV or 2.2 MeV energies, respectively.

The Daya Bay Reactor Neutrino Experiment was designed to measure the mixing angle θ_{13} with a sensitivity at 0.01 or better in $\sin^2 2\theta_{13}$ at the 90% confidence level. By using the 55-days antineutrino data, the Daya Bay Experiment first published the non-zero result of the mixing angle θ_{13}, $\sin^2 2\theta_{13} = 0.092 \pm 0.016(\text{stat.}) \pm 0.005(\text{syst.})$, with the significance of 5.2 standard deviations in March 2012 and updated the result in June

2012 with $\sin^2 2\theta_{13} = 0.089 \pm 0.010(stat.) \pm 0.005(syst.)$.

In this thesis, the θ_{13} mixing angle is measured by an independent method, which is based on the neutron capture on hydrogen signals. Several new techniques are developed to meet challenges from the higher background and different systematics, such as those due to the lower neutron capture energy (2.2 MeV), the longer capture time (200 μs), and the energy loss at the detector boundary.

With 217 days of antineutrino data, from December 24, 2011 to July 28, 2012, the rate-only analysis for the neutron capture on hydrogen gives $\sin^2 2\theta_{13} = 0.083 \pm 0.018$. The combination with the gadolinium-capture result provides the double statistics to the θ_{13} measurement. The combined measurement gives $\sin^2 2\theta_{13} = 0.089 \pm 0.008$.

誌　謝

誠如陳之藩先生的「謝天」一文所提：「因爲需要感謝的人太多了，就感謝天罷。」

感謝 天恩師德

感謝 父母的愛、家人的支持，讓我能一路走到今天。

感謝 林貴林老師這幾年來的指導與鼓勵。

感謝 臺灣大學熊怡老師、聯合大學王正祥老師、北京清華大學陳少敏老師、王喆老師平時的指導。

感謝 在這段日子裡一起合作夥伴，南開大學季向盼同學、北京清華大學魏瀚宇、張一鳴、Logan Lebanowski。很開心能夠和你們一起共事、一起學習。以及北京清華劉卿樓 801、802 辦公室的同學們，感謝你們平日的照顧。

感謝 大亞灣合作組裡的所有同仁，很榮幸能與你們一起共事、一起完成這項重要的科學研究。

感謝 交大物理所的老師、所辦小姐們的照顧。

感謝 宇宙射線實驗室的學長、學姊們以及學弟妹們，感謝你們經常給予我許多建議、鼓勵。

感謝 我身邊的朋友們，謝謝你們陪我一起走過這一段『博士班的天堂路』！

Contents

List of Figures

List of Tables

Chapter 1

Introduction

"Neutrino" was proposed for explaining the phenomenon of the β-decay experiment. J. Chadwick discovered a continuous spectrum in β-decay. It was a surprising result, so there were many postulations to explain this phenomenon. W. Pauli first proposed that there is a new particle with spin-$\frac{1}{2}$, which carries away the energy. This proposal simultaneously explained the energy-momentum conservation and angular momentum conservation in the β-decay process. Later, E. Fermi named this particle as neutrino, ν, and proposed the theory of weak interaction.

In the early 1950's, F. Reynes ad C. Cowan first detected the electron antineutrino via the inverse beta decay (IBD) process [1] ,

$$\overline{\nu_e} + p \rightarrow e^+ + n. \tag{1.1}$$

In 1962, L. Lederman, M. Schwartz and J. Steinberger detected the muon neutrino [1]. Later, in 2000, the tau neutrino was discovered at the Fermilab [1].

1.1 Neutrino Oscillation

The idea of the neutrino oscillation was first proposed by B. Pontecorvo. In 1964, R. Davis Jr. and J. N. Bahcall proposed an experiment to detect neutrinos from the Sun [2] [3]. In 1968, the Homestake [4] solar neutrino experiment measured the electron neutrino flux from the Sun, but the flux was smaller than the theoretical prediction. This results was referred to as the solar neutrino problem. To explain this flux deficit, Maki, Nakagawa and Sakata [5] developed Pontecorvo's idea.

In 1998, Super-Kamiokande collaboration announced the first evidence of neutrino oscillations which consists the theory of the neutrino non-zero mass [6].

1.1.1 Neutrino Oscillation Probability

This can be expressed as neutrino flavor eigenstates are linear combination of the mass eigenstates,

$$|\nu_\alpha\rangle = \sum_k U^*_{\alpha k}|\nu_k\rangle, \tag{1.2}$$

where α represents the neutrino flavors, k represents the mass states, e, μ, τ, U is the mixing matrix.

The mass eigenstate $|\nu_k\rangle$ is the eigenstate of the Hamiltonian with the eigenvalues $E_k = \sqrt{\overrightarrow{p}^2 + m_k^2}$,

$$\mathcal{H}|\nu_k\rangle = E_k|\nu_k\rangle. \tag{1.3}$$

From the Schrodinger equation,

$$i\frac{\mathrm{d}}{\mathrm{dt}}|\nu_k(t)\rangle = \mathcal{H}|\nu_k(t)\rangle, \tag{1.4}$$

we obtain the time evolution of massive neutrino eigenstates,

$$|\nu_k(t)\rangle = \mathrm{e}^{-iE_kt}|\nu_k\rangle. \tag{1.5}$$

From, Eqs (1.2) and (1.5), we have,

$$|\nu_\alpha(t)\rangle = \sum_k U^*_{\alpha k}\mathrm{e}^{-iE_kt}|\nu_k\rangle. \tag{1.6}$$

For $t = 0$, $|\nu_\alpha(t = 0)\rangle = |\nu_\alpha\rangle$.

By the unitarity relation, Eq (1.2) can be rewritten as

$$|\nu_k\rangle = \sum U_{\alpha k}|\nu_\alpha\rangle. \tag{1.7}$$

Then, Eq (1.6) becomes

$$|\nu_\alpha(t)\rangle = \sum_\beta \left(\sum_k U^*_{\alpha k} \mathrm{e}^{-iE_k t} U_{\beta k} \right) |\nu_\alpha\rangle. \tag{1.8}$$

The transition amplitude for $\nu_\alpha \to \nu_\beta$ given by

$$\mathcal{A}_{\nu_\alpha \to \nu_\beta}(t) \equiv \langle \nu_\beta | \nu_\alpha(t) \rangle = \sum_k U^*_{\alpha k} U_{\beta k} \mathrm{e}^{-iE_k t}. \tag{1.9}$$

Therefore, the probability for ν_α oscillating into ν_β is

$$P_{\nu_\alpha \to \nu_\beta}(t) = |\mathcal{A}_{\nu_\alpha \to \nu_\beta}(t)|^2 = \sum_{kj} U^*_{\alpha k} U_{\beta k} U_{\alpha j} U^*_{\beta j} \mathrm{e}^{-i(E_k - E_j)t}. \tag{1.10}$$

For ultrarelativistic neutrinos, they propagate at the light speed, so we can assume $m_k \ll p$ and the energy can be approximated with $E = |\overrightarrow{p}|$ and $E_k \simeq E + \frac{m_k^2}{2E}$. We then obtain

$$P_{\nu_\alpha \to \nu_\beta}(t) = \sum_{kj} U^*_{\alpha k} U_{\beta k} U_{\alpha j} U^*_{\beta j} \exp(-i \frac{\Delta m^2_{kj} t}{2E}), \tag{1.11}$$

with $\Delta m^2_{kj} \equiv m_k^2 - m_j^2$.

Since $v_\nu \sim c$, we take the approximation $t = L$, where L is the distance between the source and the detector. Hence

$$P_{\nu_\alpha \to \nu_\beta}(L, E) = \sum_{kj} U^*_{\alpha k} U_{\beta k} U_{\alpha j} U^*_{\beta j} \exp(-i \frac{\Delta m^2_{kj} L}{2E}). \tag{1.12}$$

Using the unitarity relation,

$$\sum_k |U_{\alpha k}|^2 |U_{\beta k}|^2 = \delta_{\alpha\beta} - 2 \sum_{kj} \Re[U^*_{\alpha k} U_{\beta k} U_{\alpha j} U^*_{\beta j}], \tag{1.13}$$

we rewrite Eq (1.12) into [7]

$$\begin{aligned} P_{\nu_\alpha \to \nu_\beta}(L, E) = \delta_{\alpha\beta} \quad & - \quad 4 \sum_{k>j} \Re[U^*_{\alpha k} U_{\beta k} U_{\alpha j} U^*_{\beta j}] \sin^2(\frac{\Delta m^2_{kj} L}{4E}) \\ & + \quad 2 \sum_{k>j} \Im[U^*_{\alpha k} U_{\beta k} U_{\alpha j} U^*_{\beta j}] \sin(\frac{\Delta m^2_{kj} L}{2E}) \end{aligned} \tag{1.14}$$

For the antineutrino case, $\overline{\nu}_\alpha$, one has

$$|\overline{\nu}_\alpha\rangle = \sum_k U_{\alpha k}|\overline{\nu}_k\rangle. \tag{1.15}$$

Hence the probability for the oscillation $\overline{\nu}_\alpha \to \overline{\nu}_\beta$ is

$$\begin{aligned} P_{\overline{\nu}_\alpha\to\overline{\nu}_\beta}(L,E) = \delta_{\alpha\beta} &- 4\sum_{k>j}\Re[U^*_{\alpha k}U_{\beta k}U_{\alpha j}U^*_{\beta j}]\sin^2(\frac{\Delta m^2_{kj}L}{4E}) \\ &- 2\sum_{k>j}\Im[U^*_{\alpha k}U_{\beta k}U_{\alpha j}U^*_{\beta j}]\sin(\frac{\Delta m^2_{kj}L}{2E}). \end{aligned} \tag{1.16}$$

The above probability is named as survival probability for $\alpha = \beta$ while it is transition probability for $\alpha \neq \beta$.

For three neutrino flavors, the matrix expression of Eq (1.2) is

$$\begin{pmatrix}\nu_e\\ \nu_\mu\\ \nu_\tau\end{pmatrix} = U_{PMNS}\begin{pmatrix}\nu_1\\ \nu_2\\ \nu_3\end{pmatrix}, \tag{1.17}$$

where U_{PMNS} is the mixing matrix is known as Pontecorvo-Maki-Nakagawa-Sakata matrix,

$$\begin{aligned} U_{PMNS} &= \begin{pmatrix} U_{e1} & U_{e2} & U_{e3}\\ U_{\mu 1} & U_{\mu 2} & U_{\mu 3}\\ U_{\tau 1} & U_{\tau 2} & U_{\tau 3}\end{pmatrix} \\ &= \begin{pmatrix}1 & 0 & 0\\ 0 & C_{23} & S_{23}\\ 0 & -S_{23} & C_{23}\end{pmatrix}\begin{pmatrix} C_{13} & 0 & S_{13}e^{-i\delta_{CP}}\\ 0 & 1 & 0\\ -S_{13}e^{i\delta_{CP}} & 0 & C_{13}\end{pmatrix}\begin{pmatrix} C_{12} & S_{12} & 0\\ -S_{12} & C_{12} & 0\\ 0 & 0 & 1\end{pmatrix} \\ &= \begin{pmatrix} C_{13}C_{12} & C_{13}S_{12} & S_{13}e^{-i\delta}\\ -C_{23}S_{12} - S_{13}C_{12}S_{23}e^{i\delta} & C_{23}C_{12} - S_{13}S_{12}S_{23}e^{-i\delta} & C_{13}S_{23}\\ S_{23}S_{12} - S_{13}C_{12}C_{23}e^{i\delta} & -S_{23}C_{12} - S_{13}S_{12}S_{23}e^{i\delta} & C_{13}C_{23}\end{pmatrix}, \end{aligned} \tag{1.18}$$

where $C_{jk} = \cos\theta_{jk}$, $S_{jk} = \sin\theta_{jk}$.

In Eq (1.18), there are six parameters to describe the mixing matrix of the three flavor neutrino oscillation, which are three mixing angle, θ_{jk}, two mass-squared differences, $\Delta m^2_{jk} \equiv m^2_j - m^2_k$, and one CP-violation phase, δ_{CP}. From the current experiments, $\sin^2\theta_{23}$ and $\sin^2\theta_{12}$ are about $0.386^{+0.024}_{-0.021}$ and $0.307^{+0.018}_{-0.016}$ [8], which were determined by the atmospheric neutrino experiment and solar neutrino experiment; while Δm^2_{21} is $7.50^{+0.19}_{-0.20} \times 10^{-5}\text{eV}^2$ and Δm^2_{31} is $(2.4 \pm 0.1) \times 10^{-3}\text{eV}^2$.

For reactor neutrino experiment, we take $\alpha = e$ and $\beta = e$ such that

$$\begin{aligned} P_{\overline{\nu}_e \to \overline{\nu}_e}(L,E) = 1 &- 4\sum_{k>j} \Re[U^*_{ek}U_{ek}U_{ej}U^*_{ej}]\sin^2(\frac{\Delta m^2_{kj}L}{4E}) \\ = 1 &- \sin^2 2\theta_{13}\left[\sin^2\theta_{12}\sin^2(\frac{\Delta m^2_{32}L}{4E}) + \cos^2\theta_{12}\sin^2(\frac{\Delta m^2_{31}L}{4E})\right] \\ &- \cos^4\theta_{13}\sin^2 2\theta_{12}\sin^2(\frac{\Delta m^2_{21}L}{4E}) \end{aligned} \tag{1.19}$$

For the realistic unit, $\frac{\Delta m^2_{kj}L}{4E}$ is rewrite as $\frac{\Delta m^2_{kj}c^4}{4\hbar c} \cdot \frac{L}{E}$, where $\hbar c = 197.33 \times 10^{-9}$ eV $\cdot$ m, such that

$$\frac{\Delta m^2_{kj}c^4}{4\hbar c} \cdot \frac{L}{E} = \frac{\Delta m^2_{kj}c^4}{4 \cdot 197 \times 10^{-9}} \cdot \frac{L}{E} \sim 1.267 \cdot \frac{\Delta m^2_{kj}(\text{eV}^2)\ L(\text{km})}{E(\text{GeV})} \tag{1.20}$$

Considering $E = 3.5$ MeV, $\Delta m^2_{31} \sim \Delta m^2_{32} = 2.32 \times 10^{-3}$ eV^2, $\Delta m^2_{21} = 7.59 \times 10^{-5}$ eV^2 and $\sin^2 2\theta_{12} = 0.861$ [9], the relation between survival probability and the distance are shown in Fig 1.1. The mixing angle θ_{13} can be extracted by the deficit of reactor antineutrinos at about 2 km.

1.2 Neutrino Oscillation Experiments

According to Eq (1.16), one can categorize neutrino oscillation experiments into appearance experiments and disappearance experiments [7]. The former corresponds to $\alpha \neq \beta$ and the latter corresponds to $\alpha = \beta$.

In the mixing matrix, U_{PMNS}, the mixing angles θ_{23} and θ_{12} have been measured by atmospheric and solar - neutrino experiments [6], respectively. The θ_{13} is the last measured mixing angle.

There are two channels to measure θ_{13}:

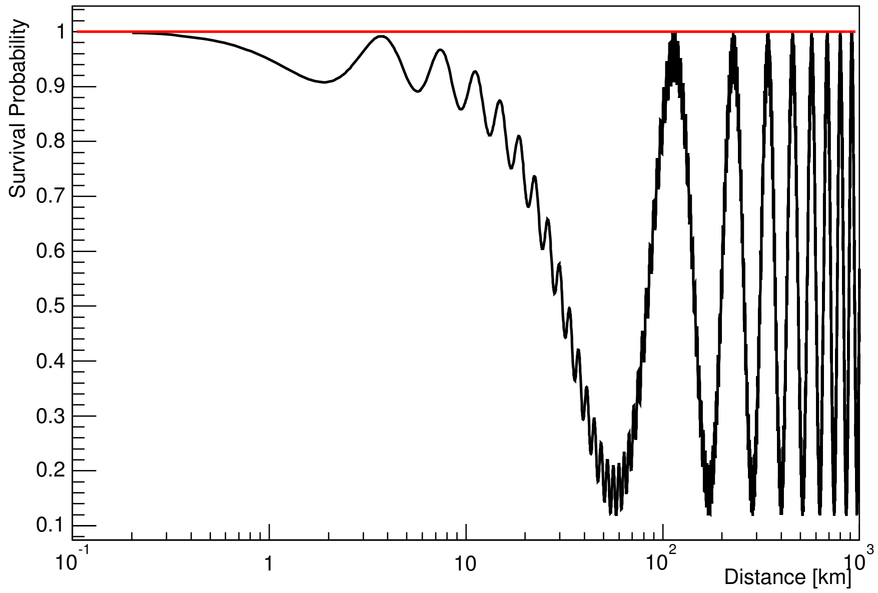

Figure 1.1: Survival probability vs Distance.

Appearance channel: $\nu_\mu \rightarrow \nu_e$

The transition probability is

$$\begin{aligned} P_{\nu_\mu \rightarrow \nu_e} &\simeq \sin^2 2\theta_{13} \sin^2 \theta_{23} \sin^2 \frac{\Delta m^2_{31} L}{4E} \\ &- \frac{\sin 2\theta_{12} \sin 2\theta_{23}}{2 \sin \theta_{13}} \sin \frac{\Delta m^2_{21} L}{4E} \sin^2 2\theta_{13} \sin^2 \frac{\Delta m^2_{31} L}{4E} \sin \delta_{CP} \\ &+ (\text{CP even term}, \text{solar term}, \text{matter effect term}), \end{aligned} \tag{1.21}$$

where L is the distance between the source and the detector and E is the neutrino energy.

These experiments are accelerator-based, such as MINOS (Main Injector Neutrino Oscillation Search) [10] [11], NOνA (NuMI Off-Axis ν_e Appearance) [12] and T2K (Tokai to Kamioka, Japan) [13] [14]. Neutrino beam is generated by the accelerator and one looks for the appearance of electron neutrinos in a muon neutrino beam. The appearance is sensitive to the mass hierarchy and the CP-violating phase. This experiment requires much longer baselines (about hundred of kms) and very large detectors ($>$ 10 ktons) and powerful beams (about 1 MW[1]).

---

[1] W is a symbol of Watt, which is the unit of power.

Disappearance channel: $\overline{\nu}_e \rightarrow \overline{\nu}_e$

The survival probability is given by the Eq (1.19). These experiments are known as the reactor-based experiments, such as Daya Bay [15], Double CHOOZ [16] and RENO (Reactor Experiment for Neutrino Oscillations) [17]. The anti-neutrinos are from the nuclear reactors and one looks for the disappearance of electron anti-neutrinos. The reactor can produce the $\overline{\nu}_e$ beam and it is an intense source ($> 10^{20}\ \overline{\nu}_e/s$). Another advantage for using reactor neutrino is because that it allows a clean detection and its oscillation is independent of the CP-violating phase and the matter effect.

1.2.1 MINOS

The MINOS experiment is designed to measure the neutrino oscillations $\nu_\mu \rightarrow \nu_\mu$ and $\nu_\mu \rightarrow \nu_e$. There are two identical detectors located at Fermilab and the Soudan Underground Laboratory in Northern Minnesota. The former is the near site detector and the later one is the far site detector. Both detectors are tracking-sampling calorimeters (steel-scintillating sampling calorimeters). The 2.54 cm thick steel planes are magnetized for charge identification and to determine the momentum. The wavelength shifting (WLS) fiber is connected to the strip of plastic scintillator to collect the light.

The neutrino beam is provided by the NuMI (Neutrinos at the Main Injector) facility. The protons are accelerated to 120GeV/c by the Main Injector and strike the graphite target. The hadrons, such as pions and kaons, are produced from this process. The positive charged hadrons are focused into one beam and processed to the long decay pipe. They decay to muons and muon neutrinos with the latter travelling to the near and far detectors.

The survival probability of ν_μ is measured by comparing the energy spectrum of the charge current (CC) ν_μ interactions at the near and the far detectors. The current results for MINOS is $|\Delta m^2| = \left(2.32^{+0.12}_{-0.08}\right) \times 10^{-3}$ eV^2 for the atmospheric mass splitting [18].

1.2.2 NOνA

The NOνA experiment is designed to answer the questions on neutrino oscillation, mass hierarchy and CPV in ν sectors . This experiment also has two detector sites, both located 14.5 mead off the axis of the NuMI beam line. A 222 ton near detector locating at the Fermilab is used to measure the inherent beam backgrounds. The 14 kiloton far detector is composed of about 38500 cells of the PVC plastic and filled with the liquid scintillator, which is located at near Ash River, Minnesota.

1.2.3 T2K

T2K experiment is one of the long-baseline experiment for the neutrino oscillation research. The off-axis neutrino beam is provided by the J-PARC accelerator. The near detector, ND280, is 280 meters from the graphite target and measures the neutrino energy spectrum, flux and flavor content. It consists of the time projection chambers (TPC), fine-grained detectors (FGDs), Pi zero detector, side muon range detector (SMRD) and electromagnetic calorimeter (ECAL). The far site detector is the massive Super Kamiokande detector, which consists of 50 kilotons of pure water and about 11200 photomultiplier tubes.

1.2.4 Double CHOOZ

The Double CHOOZ experiment is designed to measure the neutron oscillation mixing angle, θ_{13}. The electron anti-neutrino sources are from the CHOOZ reactor power plant in France, which provided 8.5 $\mathrm{GW_{th}}$. There are two detectors for near site and far site measurements. The detectors are composed of the neutrino target (Gd-load liquid scintillator), gamma catcher (liquid scintillator), buffer (mineral oil), inner veto (liquid scintillator), outer veto (plastic scintillator strips) and 10 inch photomultiplier tubes (PMTs). The distance from the reactor cores to the near and far sites are 400 meter and 1050 meter, respectively.

1.2.5 RENO

The six 2.8 $\mathrm{GW_{th}}$ reactors at the Yonggwang Nuclear Power Plant in Korea provide the RENO experiment to measure the neutrino oscillation mixing angle, θ_{13}. Two detectors are located at 290 meter and 1380 meter from the reactors.

1.2.6 The Race for Hunting Mixing Angle θ_{13}

In 2003, CHOOZ measured $\sin^2 2\theta_{13} < 0.15$ [19]. Figure 1.2 shows the recent results from each experiment. In 2011, T2K published a non-zero θ_{13} result which is $0.03(0.04) <$

$\sin^2 2\theta_{13} < 0.28(0.24)$ [21] at 90% C.L. for normal(inverted) neutrino mass hierarchy. In the same year, MINOS measured $2\sin^2\theta_{23}\sin^2 2\theta_{13} = 0.041^{+0.047}_{-0.031}$ [22].

In 2012, the Daya Bay collaboration published the first result for non-zero θ_{13}, $\sin^2 2\theta_{13} = 0.092 \pm 0.016(stat) \pm 0.005(syst)$, which has a significance of 5.2 standard deviations [23].

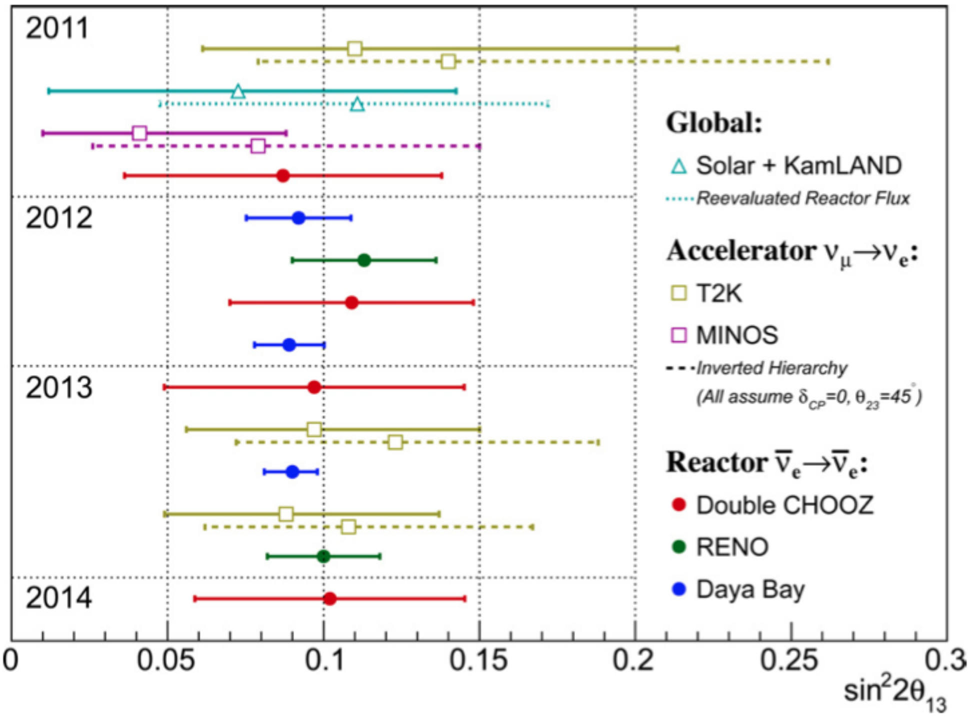

Figure 1.2: The status of the mixing angle θ_{13} measurement [20].

1.3 The Measurement Strategy of Daya Bay Experiment

The Daya Bay reactor antineutrino experiment aims to determine the neutrino mixing angle θ_{13}. It was designed to measure $\sin^2 2\theta_{13}$ to better than 0.01 at 90 % C.L. [15]. To achieve this, there are three basic requirements, the baseline optimization, high statistics and the reduction of systematic errors.

The detector baselines are optimized based upon the survival probability. To have a high statistics, the experimental sites are near the power plant complex, Daya Bay Power Plant Complex, which can produce 17.4 GW thermal power. We have identically designed antineutrino detectors (ADs) and good calibration system and calibration processes. The systematic errors can be reduced by comparing the near site and far site detections,

$$\frac{N_f}{N_n} = \left(\frac{N_{p,f}}{N_{p,n}}\right)\left(\frac{L_n}{L_f}\right)^2\left(\frac{\varepsilon_f}{\varepsilon_n}\right)\left(\frac{P_{sur}(E, L_f)}{P_{sur}(E, L_n)}\right), \tag{1.22}$$

where $N_{f(n)}$ is the number of IBD events detected in the far (near) site detectors, $N_{p,f(n)}$ is the number of target protons in the far (near) site detectors, $L_{f(n)}$ is the distance between the reactors and far (near) site detectors, $\varepsilon_{f(n)}$ is the efficiency for far (near) site detector, and $P_{sur}(E, L_{f/n})$ is the survival probability at far/near sites.

1.4 The Antineutrino Detection via the Delayed Neutron Capture on Hydrogen

The antineutrino interacts with the proton in the detector, which produces a positron and a neutron. This reaction is known as the inverse beta decay process, as shown by Eq (1.1). The positron first annihilates with electron in a very short time and emits two gammas. This process is known as the prompt signal. The neutron is first thermalized and then captured by Gadolinium or Hydrogen with the emission of $\sim$ 8 MeV gammas in the former case or the emission of ~2.2 MeV gammas in the latter case. This signal is referred to as delayed signal.

The advantage to use the Gadolinium doped liquid scintillator is to avoid the low energy backgrounds. However, using the delayed signal from the neutron capture on hydrogen can provide a separate measurement of θ_{13} and improve the overall sensitivity of θ_{13} measurement. In addition, there are several new techniques developed to meet the challenges arising from higher background and different systematics, such as those due to the lower neutron capture energy (2.2 MeV), the longer capture time (200 μs), and the larger energy leakage at the detector boundary.

1.5 My contribution to the Daya Bay experiment

During the construction period of the experiment, I have been involving in the fabrication of the inner acrylic vessel, such as the assembling, particle content measurement and the quality control process. After these, I was at the Daya Bay experimental site for the detector assembling, which includes the PMT cabling, assembling with the electromagnetic shielding and the testing of light leakage at the water pool.

Since the commissioning of the experiment, I have been working on the Calibration Working Group in the Daya Bay experiment. I have been studying various properties of PMTs, such as the ringing effect with improved algorithms. Currently, I am still responsible for the PMT gain calibration and monitoring issues. Finally, my thesis topic is on the measurement of θ_{13} with the IBD neutron captured by Hydrogen., as stated in the previous session.

In Chap. 2, we introduce the Daya Bay experiment, which includes the experimental layout, the structure of antineutrino detectors and the muon detectors. Chapter 3 introduces the data production processes. We describe the PMT calibration methods and the energy reconstruction procedures in details. These works are very crucial for the precise measurements in Daya Bay experiment. Chapter 4 introduces the selection criteria for the IBD candidates in the delayed neutron capture on hydrogen analysis. The backgrounds estimation and background subtraction processes are discussed in Chapter 5. Finally, the efficiencies and the uncertainties are presented in Chapter 6. At the end of Chapter 6, the θ_{13} will be extracted with the χ^2 fitting method. We present our conclusions in Chapter 7.

Chapter 2

Daya Bay Experiment

2.1 Layout

The Daya Bay experimental site is located at the southern part of China near the Shenzhen city. The Daya Bay nuclear power complex consists of six reactor cores groups into three nuclear power plants (NPPs): Daya Bay NPPs, Ling Ao NPPs and Ling Ao II NPPs. The distance between near two reactors is about 90 m. All of the reactor cores are functionally identical which pressurized water reactors of 2.9 GW thermal power. They provide 17.4 GW thermal power [24].

There are three underground experimental halls (EHs). Two of them are near halls and the third one is far hall, shown in Figure 2.1. The location of the experimental halls (baselines) had been optimized, shows in the Table 2.1. The connection of each experimental halls are by horizontal tunnels and the total length of the tunnel system is 3100 m. For near halls, each hall contains two detectors for determining the reactor neutrino flux; for far site, there are four detectors for measuring the neutrino oscillations. The detectors are shielded by the water pool and covered resistance plate chambers (RPCs). Figure 2.3 shows the schematics of the near experimental hall.

2.2 Antineutrino Detector

The antineutrino detectors (ADs) are functionally-identical. Each one consists of three zones, target, catcher and buffer zones. These three zones are separated by the acrylic

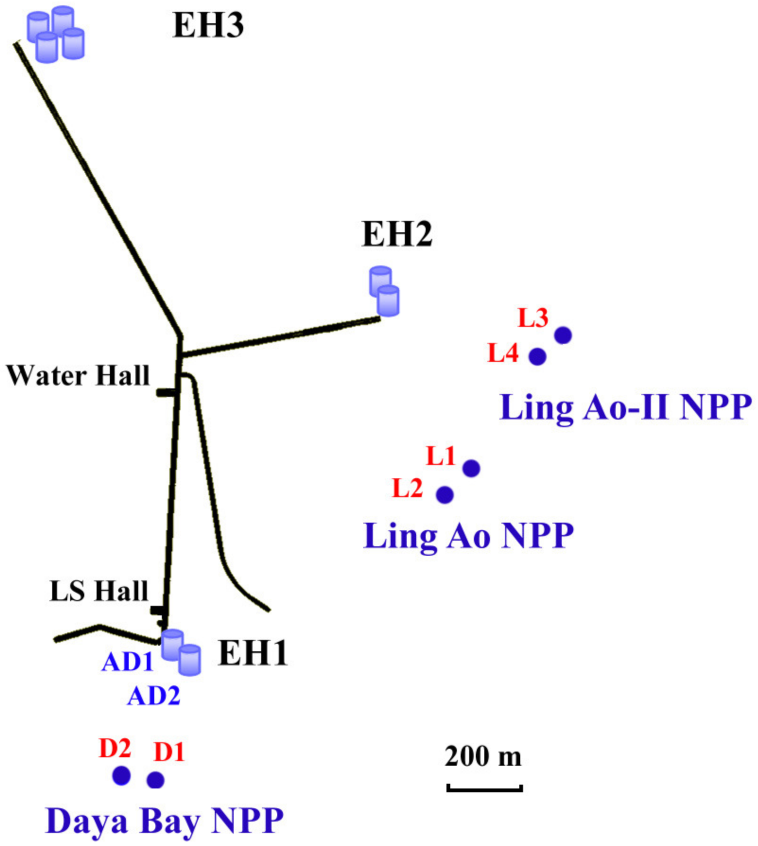

Figure 2.1: Daya Bay experimental site layout [23].

	EH1	EH2	EH3
Overburden (m.v.e)	280	300	80
DYB cores	360	1350	1910
Distance to LA I cores	860	480	1540
LA II cores	1310	1540	1550

Table 2.1: The approximated values for the overburden and distance between the experimental halls and the nuclear power plants [24].

vessel. The reflectors are placed on the top and the bottom to increase the detection efficiency. The photomultiplier tubes are setting at the buffer zone to capture the visible light from the center detector. The automatically calibration units located on the top of the stainless steel vessel. Figure 2.2 is a cross-sectional view of an AD.

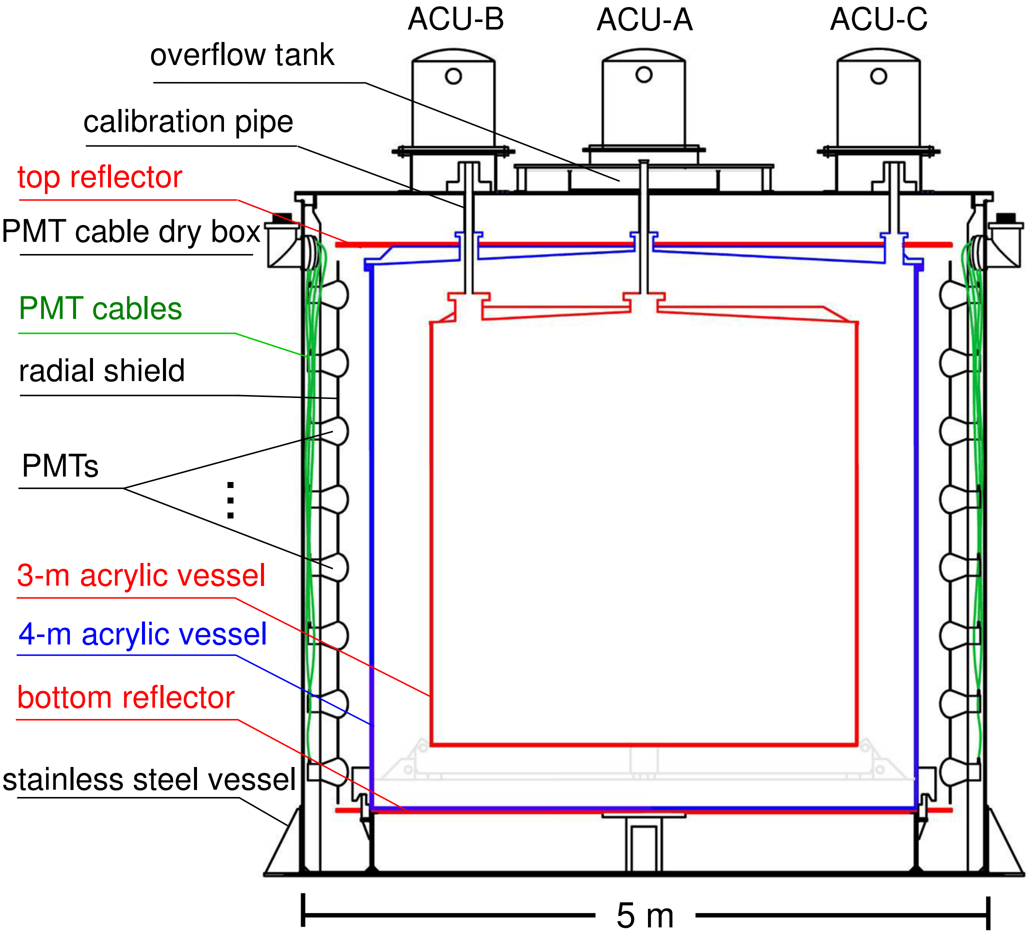

Figure 2.2: The cross-sectional view of an antineutrino detector [24].

2.2.1 Three Zones detector

2.2.1.1 Antineutrino Target

The inner zone is the antineutrino target which contains 20 tons of 1%-doped gadolinium-loaded liquid scintillator(GdLS). The solvent of GdLS is the organic scintillator linear alkyl benzene (LAB), which has the low volatility, high flash point and good compatibility with many materials. The 1%-doped gadolinium is from Gd(TMHA)$_3$ complex, which can increase the neutron capture efficiency. In addition, the 2,5-diphenyloxazole (PPO) and

1,4-bis[2-methylstyryl]benzene (bis-MSB) are for the fluor and wavelength-shifter. They shift the visible light to the wavelength between 400 and 450 nm. The density of GdLS is 0.86 g/ml. The diameter of inner acrylic vessel (IAV) is 3.1 meter and the wall thickness is 10 mm; Both IAV and OAV are made of UV-transparent acrylic.

2.2.1.2 Gamma Catcher Area

The middle zone contains 20 tons of liquid scintillator (LS) for detecting the gammas escaping from the target volume. Except the Gd, the contents are almost same as GdLS and the density of GdLS is 0.859 g/ml. It improves the energy resolution and reduces the efficiency uncertainties. The recipe of LS is the same as GdLS except the Gd-doped. For outer acrylic vessel (OAV), the diameter is 4 meter and the wall thickness is 18 mm. To increase the photon statistics and improve the uniformity of the energy responses, two reflective panels are placed on the top and bottom of OAV, respectively. The reflective panels are composed of a reflect film, ESR (Vikuiti Enhanced Specular Reflector), and two acrylic panels.

2.2.1.3 Shielding

The outer zone contains 40 tons of mineral oil (MO) for shielding the radioactive background. The density of MO is 0.851 g/ml. There are 192 8" PMTs (Hamamatsu R5912) in each AD and 2" PMTs (Hamamatsu R7724) at top and bottom to monitor the attenuation length of GdLS and LS. The 8" PMTs are mounted on eight ladders, each ladder contents three columns and eight rings. The conical magnetic shields are wrapped on each PMTs to protect from the terrestrial magnetic field. The black Tyvek panels are covered in front of the ladder to shield the reflections from the unexpected way such as the cables, ladders and so on.

2.2.2 Automatic calibration units (ACUs)

There are three automatic calibration units (ACUs), which are the enclosing stainless steel shells, on the top of the detector. ACU-A locates at the central axis of the detector, ACU-B is at the radius of 135.0 cm and ACU-C is at the radius of 177.25 cm which is the gamma catcher area. Each ACU has an LED and three sources (^{68}Ge, ^{60}Co and $^{241}Am -^{13}C$), shown in Table 2.2. The sources are mounted by cables and controlled by

Source	Type	Energy	Half-life	Rate [Hz]
LED	visible light	430 nm	-	500 (adjustable)
^{68}Ge	e^{+}	1.022 MeV	270.95 days	10
^{60}Co	γ	2.5 MeV	1925.28 days	100
$^{241}Am-^{13}C$	n	~8 MeV	432.6 years	$\sim$ 0.5

Table 2.2: List of calibration source [25].

the stepper motors. We have the calibration time once a week. During the calibration, the sources are hanged in the detector and scanning the different vertical positions.

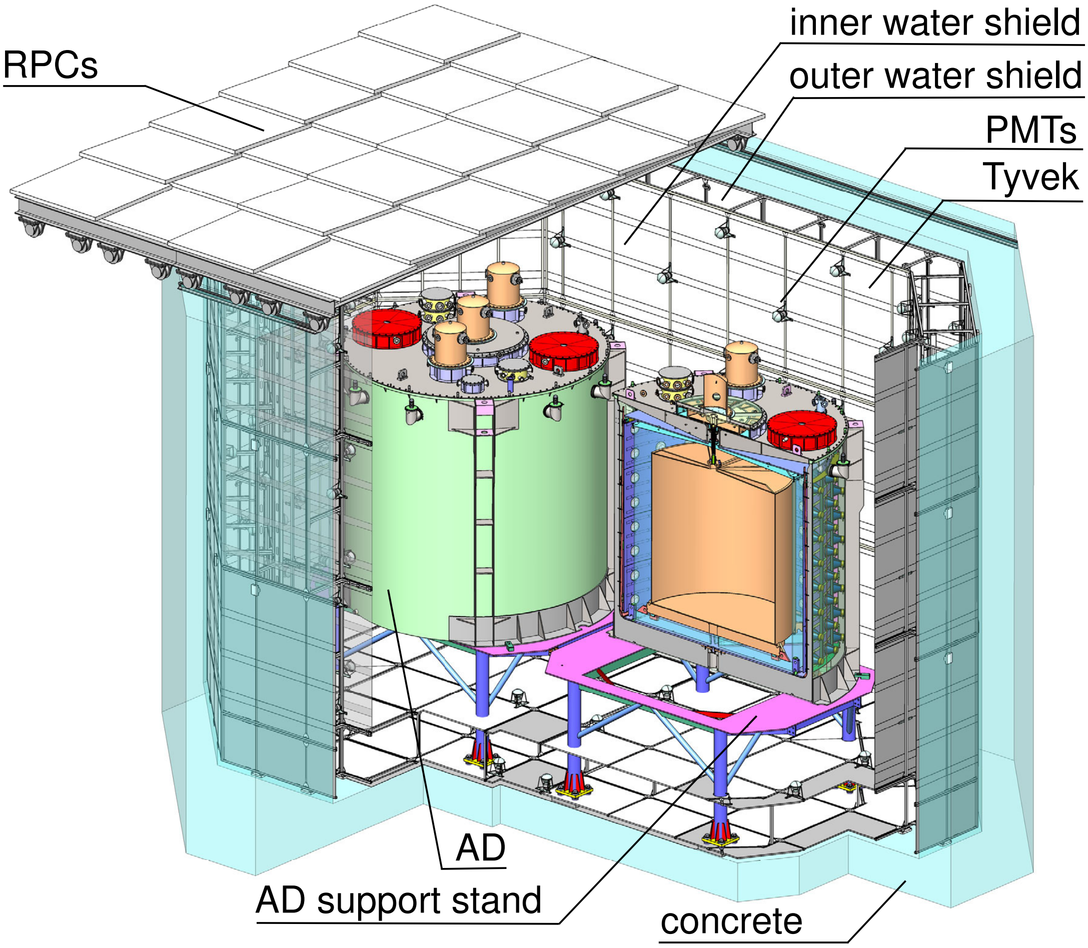

Figure 2.3: The cross-sectional view of near site [24].

2.3 Muon Veto System

For Daya Bay experiment, the mainly background is cosmic ray muon. To suppress this, we have the muon tagging system, which consists of the water Cherenkov detector and resistive plate chambers (RPCs). Figure 2.3 is a schematic of a near site experimental hall.

The water Cherenkov detector is composed of the water pool and PMTs. The water is purified water produced at 18 M-cm. The antineutrino detectors are merged in the water pool, and they have at least 2.5 m of water surrounding. The water pool contents inner water pool (IWP) and outer water pool (OWP), which are separated by white Tyvek. In IWP, the PMTs are face into the water pool. In OWP, the PMTs which are along the pool wall face into the water pool, and the PMTs on the separated shelf face out the pool wall.

In Daya Bay experiment, the resistive plate chamber (RPC) modules are used as the muon tracking devices. Each RPC module is 2.17 m × 2.20 m × 8 cm and is composed of the 4 layer RPCs, and each layer contains 8 readout strips. There are 54 modules are installed in each near site experimental hall and 81 in the far site.

The efficiency of the muon tagging is greater than 99%.

Chapter 3

Data Production

In this chapter, we discuss how we process the data.

Fig 3.1 is an illustration. Let us denote the real energy of a particle as E_{real}. When the particle enters the detector, it interacts with electrons in the scintillator and turns the molecules into excited states. As a result, photons are emitted. When photons propagate in the detector, they can be absorbed, reemitted, reflected, etc. During this process, the energy of the particle converts into visible light with energy, E_{vis}.

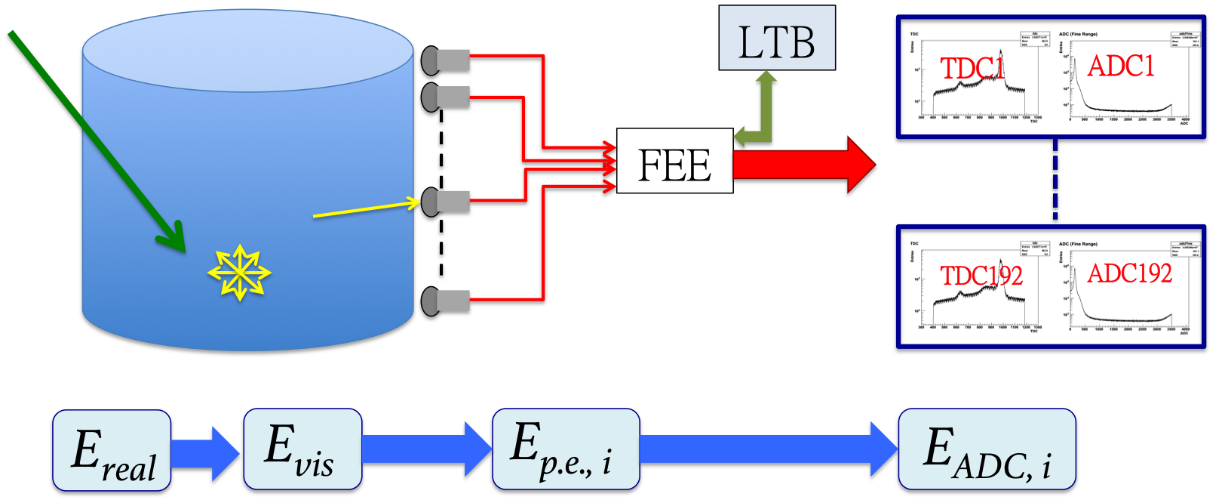

Figure 3.1: An event flow chart

When photons hit on PMTs, electrons are emitted by the photoelectron effect. Photoelectrons are amplified in the PMTs and sent to Front-End Electronics (FEE) board. There are 16 channels for each board and each one is connected to one PMT. At first, FEE identifies over-threshold channels. The threshold is set to be 0.25 photoelectrons (p.e.). Once the signal passes the threshold, the charged is measured, and the ADC values as well as the timing information, TDC, are recorded. FEE also counts the number of coincident PMT hits every 100 ns, NHIT, and the sum of each board, ESUM. These information is sent to the local trigger board (LTB) for the triggering process.

From the above, a PMT records a hit information with a pair of ADC and TDC values. A trigger consists of many hits which are in the same detector with close timings. An inverse beta decay (IBD) event contains two triggers in a coincident window. In fact, in the process of converting particle's energy to the visible light, there are energy leakage, non-uniformity, non-linearity and quenching effects so that $E_{real} \neq E_{vis}$. One can establish the relation E_{vis} and E_{real} by using calibration source or spallation neutrons. The energy leakage and non-uniformity are position dependent, thus the vertex reconstruction is necessary in the analysis. In addition, in the process of recording visible light signals by the electronics system, including PMT and FEE, the photon coverage and gain constants are different for each PMT. In summary, the process of estimating the position and energy of a physical process is referred to as reconstruction, as shown in Fig 3.2. The calibration constants, include the PMT gain constants and the energy calibration factors, are recorded in the Daya Bay database to be used in the analysis.

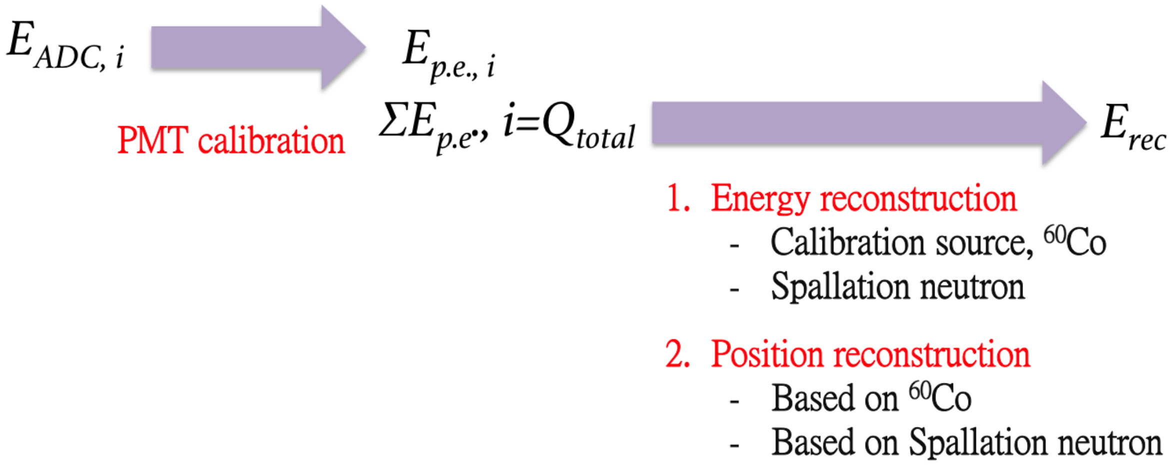

Figure 3.2: The flowchart for reconstruction process.

3.1 PMT Calibration

PMTs are crucial components of the anti-neutrino detectors. Daya Bay experiment has a good process to monitor PMT quality, which includes PMT gain, relative efficiency and channel linearity. In addition, PMT ringing and flashing have been understood.

3.1.1 Gain

The PMT gain is the conversion constant from ADC to PMT output charge in p.e. (photoelectron). We use two photon sources, low intensity LED and PMT dark noise, to measure the single photoelectron (SPE) spectrum. Three functions, simple gauss function, full model and simple full model, are used for the SPE fit. The full model is described in the later subsection, which discusses PMT pedestal, noise, SPE and multi PEs. The simple full model only considers the SPE and multi PEs.

PMT dark noise

PMT dark noises are caused by the leakage current between the electrodes and the PMT surface or the thermal emission of single electron from the cathode. They exist in the normal data taking, so this calibration process can be performed any time and it does not need to stop a run.

The signal range is for TDC value larger than 1070, as shown in Fig 3.3. First, it requires the removal of 40 MHz noise and the peak-cycle[1] are between 4 and 6. The criteria for signal selection are as follows:

- Time to previous trigger is larger than 20 μs.
- Only one hit per channel.
- Signals must be in fine gain range.
- |preAdc − avePreAdc| is less than 20.

Low intensity LED

The LED calibration is performed once a week. It is an independent process for obtaining the PMT conversion constant. To reduce the double or multiple photoelectron hits on PMT, the first criteria is that the occupancy of the PMT hits should be lower than 13%

of the total triggers. The signal range is located at TDC values between 950 and 1050, which separates the signal from the dark noise and after-pulses, as shown in Fig 3.4. The peak-cycles are between 3 and 8 and it requires the removal of 40 MHz noise. The disadvantage of this method is the need to stop the physics run, so it cannot monitor the gain fluctuation during the data taking. Therefore, this method only be used for cross check.

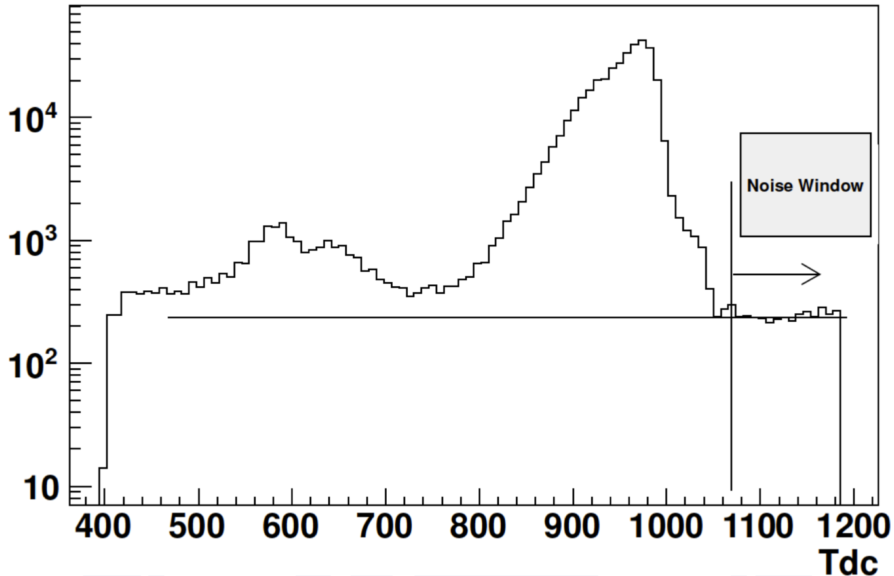

Figure 3.3: TDC distribution from the normal data taking run.

3.1.1.1 Single Photo-Electron (SPE) Fitting Model: Full Model

The fitting model for single photo-electron is from Ref. [26]. Here, we can treat the photomultiplier as an instrument with two parts, photo-electron detector and amplifier.

For simplicity, the light source illuminating on the photo-electron detector can be treated as stable, so the average number of photons hitting on PMT is a constant. However, not every photon hitting on the PMT can be converted into electron. Only part of those photons are collected by PMT, which is referred to as quantum efficiency. The process is a random binary process. The convolution of Poisson and binary processes

---

[1] Peak-cycle: When a channel has a hit, it starts to look for a 'peak' in the ADC. It will look at each ADC (every 25ns) in a window from 0 to 350ns. The peak cycle is the time of the peak; with each count equals to 25ns.

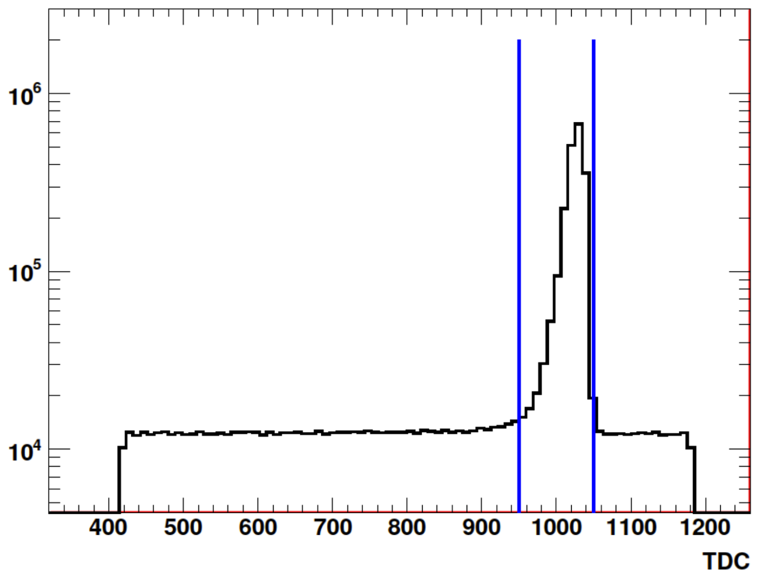

Figure 3.4: TDC distribution from the LED trigger events.

gives rise to a Poisson distribution,

$$P(n;\mu) = \frac{\mu^n e^{-\mu}}{n!}, \tag{3.1}$$

where μ is the mean value of the photo-electrons collected by the first dynode and $P(n;\mu)$ is the probability that n photo-electrons are observed when the mean value is μ.

In the amplifier part of the PMT, the charge amplification by the dynode system follows Poisson distribution. However, if the first dynode is large (more than 4), the response function can be approximated by a Gaussian distribution:

$$G_1(x) = \frac{1}{\sigma_1\sqrt{2\pi}}\exp(-\frac{(x-Q_1)^2}{2\sigma_1^2}), \tag{3.2}$$

where x is the charge variable, Q_1 is the average charge of the PMT output when one electron is collected by the first dynode, and σ_1 is the corresponding standard deviation of the charge distribution.

When more than one photo-electron are collected by the first dynode, the response function is a convolution of n single electron case:

$$G_n(x) = \frac{1}{\sigma_1\sqrt{2n\pi}}exp(-\frac{(x-nQ_1)^2}{2n\sigma_1^2}) \tag{3.3}$$

Combining these two parts, the response of an ideal noiseless PMT is given by

$$S_{ideal}(x) = P(n;\mu) \bigotimes G_n(x) = \frac{\mu^n e^{-\mu}}{n!} \frac{1}{\sigma_1\sqrt{2n\pi}} exp(-\frac{(x-nQ_1)^2}{2n\sigma_1^2}). \tag{3.4}$$

For the real PMT, the noise has to be taken into account. The noise sources include thermo-electric emissions from the photocathode or dynode, leakage current in the PMT, electron auto-emission of the electrodes, etc. There are two contributions to the background term. The first one is known as 'pedestal', which can be approximated as Gaussian function. The second contribution is the noise background. One can parameterize the background term as

$$B(x) = \frac{1-w}{\sigma_0\sqrt{2\pi}} exp(-\frac{x^2}{2\sigma_0^2}) + w\theta(x)\alpha exp(-\alpha x). \tag{3.5}$$

where σ_0 is the standard deviation for the pedestal, w, α and θ describe the background noise. w is the probability and α is the coefficient of the exponential, θ is the step function.

In Daya Bay experiment, the simple full model is the current official method for the PMT gain fit. The pedestal was first subtracted from the SPE spectrum and fitted with the simple full model. Figures 3.5 and 3.6 are the fitted PMT responses from the single photon-electron (SPE) measurement with dark noise and LED light source, respectively.

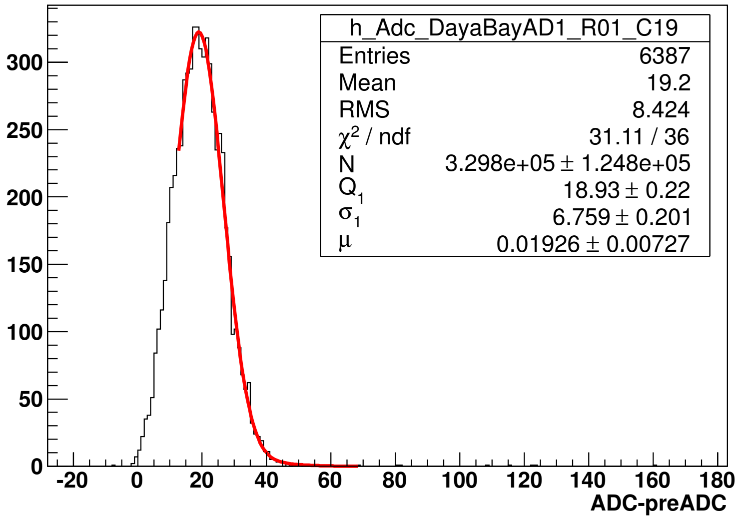

Figure 3.5: Fitting to the distribution of ADC-preADC from the PMT dark noise events with Eq. (3.4).

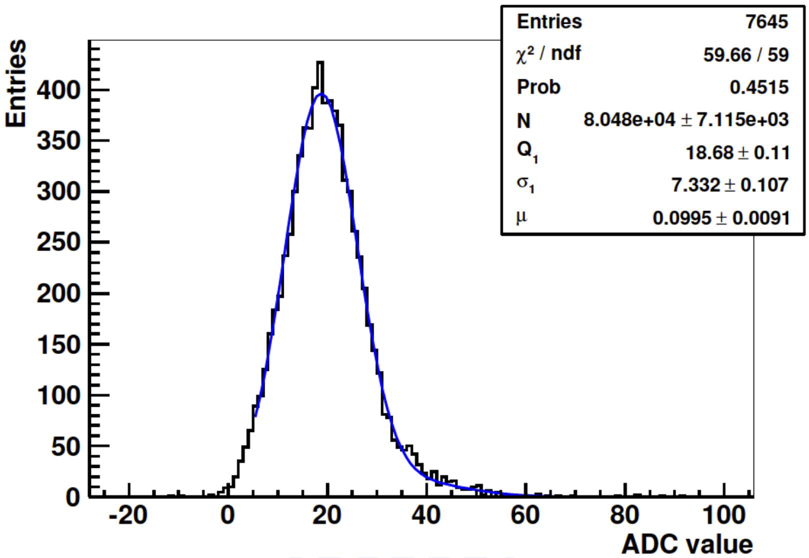

Figure 3.6: Fitting to the distribution of ADC-preADC from the LED events with Eq. (3.4).

3.1.1.2 Monitoring the conversion constant

PMT gain (ADC/SPE) is determined and monitored by the dark noise results and cross-checked with the LED calibration. Figs 3.7 and 3.8 show the current status of conversion constant.

3.1.2 Linearity

The PMT hit charge is measured by the FEE and recorded as ADC value. There are two ADC ranges, low charge (”fine”) range and higher charge (”coarse”) range. The channel charges of the former is up to about 200 p.e. at a gain of 1×10^7 and the later is from 200 p.e. up to 3000 p.e. The IBD events are in the fine gain range and the higher energy events, like muon, are in the coarse gain range.

3.1.3 Ringing

The large signals induces a large noise in the electronic response after the primary pulse, called ringing. It could effects the experimental results; such as the fake signals or duplicated hits. One example is given in Fig 3.11.

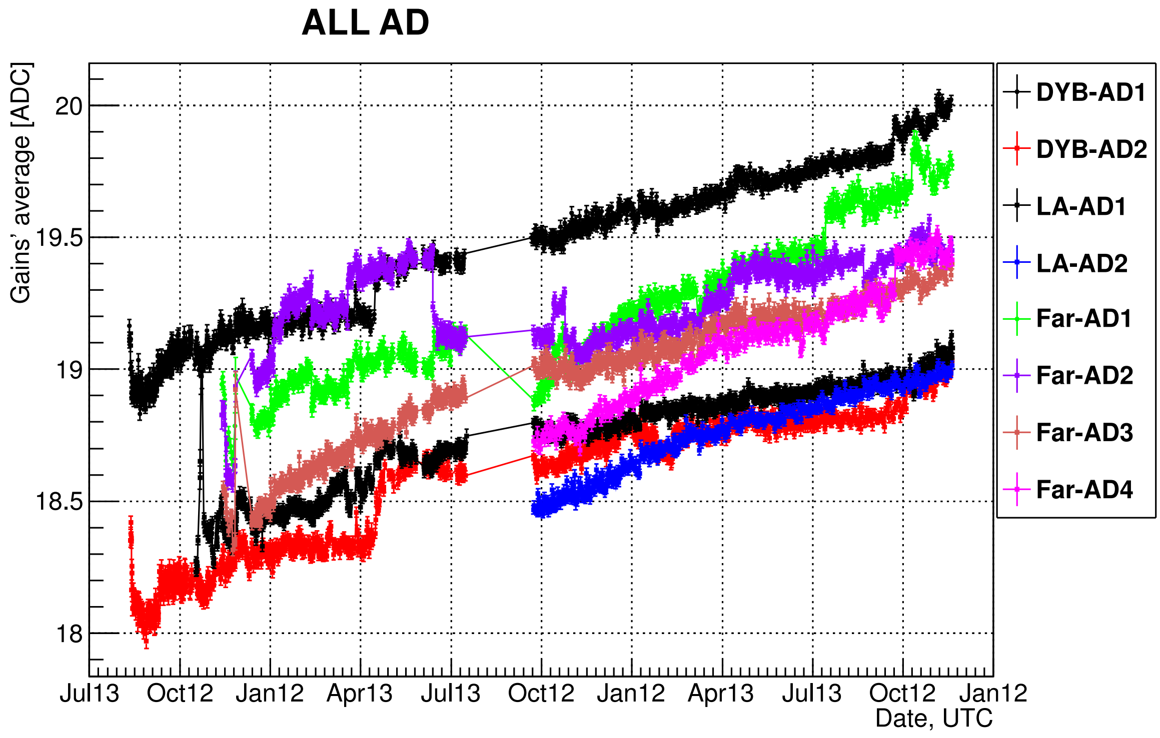

Figure 3.7: PMT gain for all ADs via the dark noise measurement from Aug 24, 2011 to Dec 31, 2013.

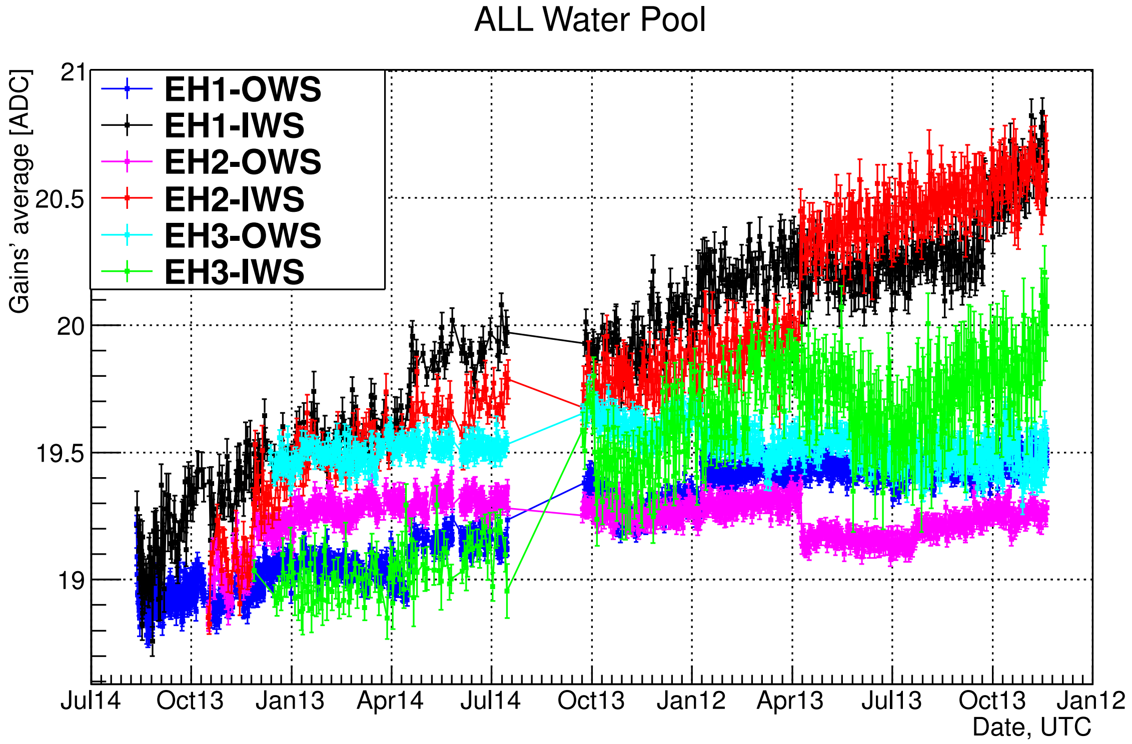

Figure 3.8: PMT gain for all WPs via the dark noise measurement from Aug 24, 2011 to Dec 31, 2013.

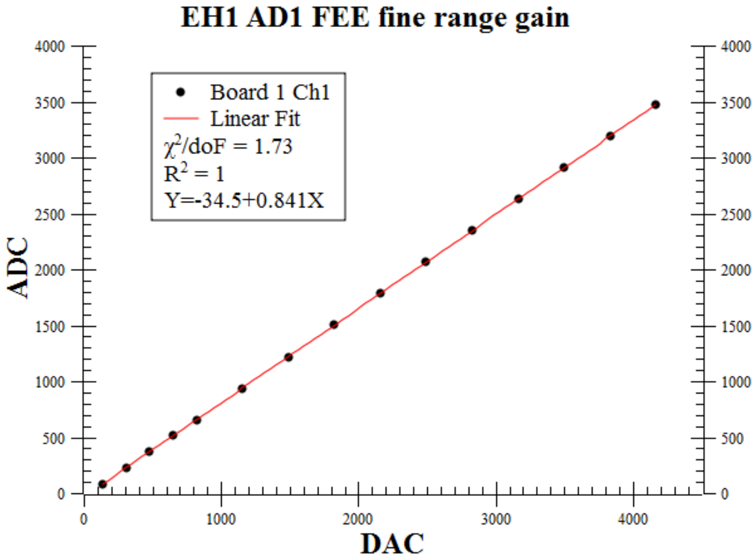

Figure 3.9: The linearity between fine gain ADC and DAC (input charge).

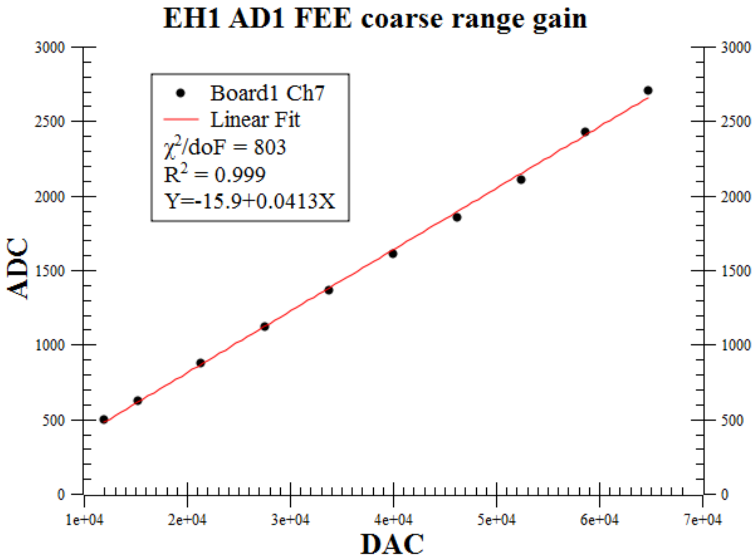

Figure 3.10: The linearity between coarse gain ADC and DAC (input charge).

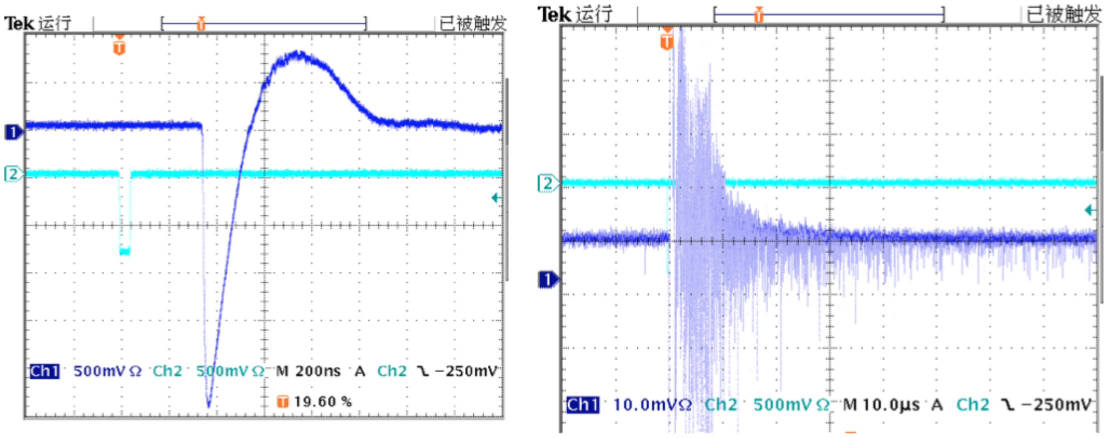

Channel 1(blue): signal;
ampl =500mV/div; t=200ns/div
Signal amplitude: ~3.4V ~800PE;
the maximum amplitude of PMT signal output,
and signal width increased

Channel 1(blue): signal;
ampl =10mV/div; t=10us/div
Signal amplitude: ~3.4V ;
Baseline recover time to less than 10mV: <10us;
Baseline recover time to less than 5mV: <15us;

Figure 3.11: Monitoring PMT ringing from the scope. PMT signal output with the scale of 500 mV/div and 200 ns/div (left) and the scale of 10 mV/div and 10 us/div (right).

The LED calibration data was used to study the feature of PMT ringing. To find the correlation between ringing and the amplitude of the primary pulse, which is also related to the hit charge, we verified the LED drive voltage and monitored the charge and the time interval between ringing and primary pulse, as shown in Fig 3.12 and Fig 3.13.

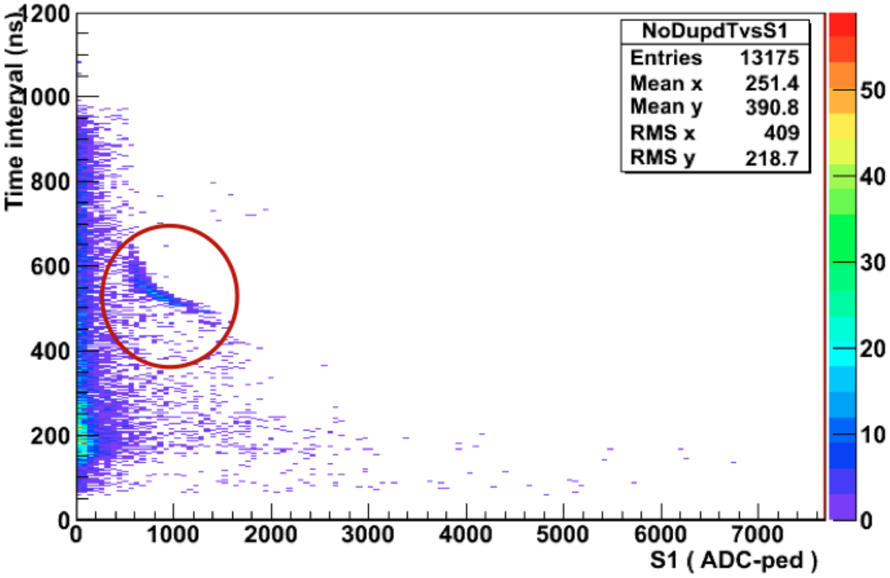

Figure 3.12: The time interval between first and second pulse versus the first charge (ADC-pedestal).

From these results, we can conclude that the ringing becomes obvious for pulses with amplitudes greater than about 800 mV. The minimum time interval between the primary

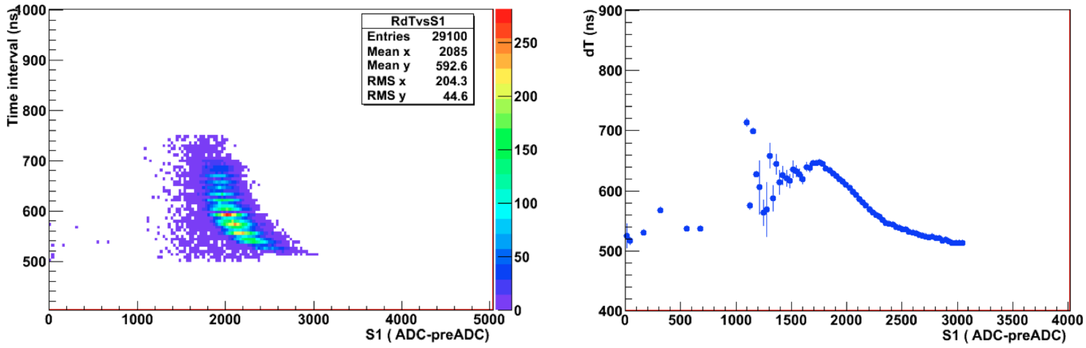

(a) The time interval between first and second signals versus the first charge (ADC-pedestal) for LED drive voltage at 7.4v

(b) The projection from the left figure.

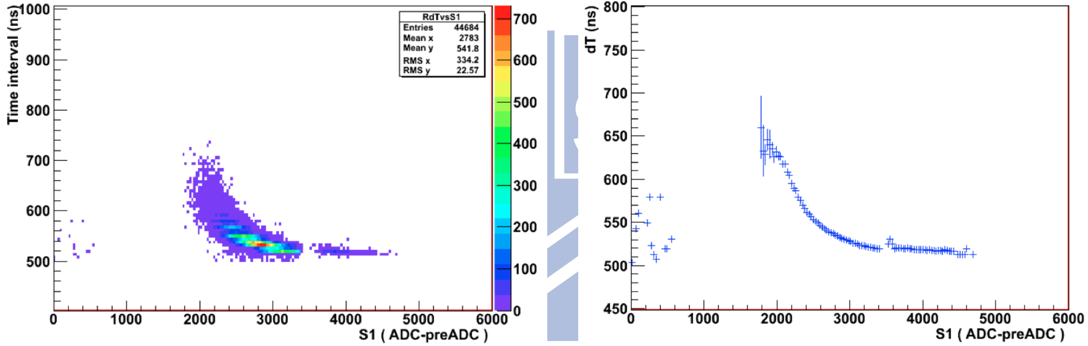

(c) The time interval between first and second signals versus the first charge (ADC-pedestal) for LED drive voltage at 7.7v

(d) The projection from the left figure.

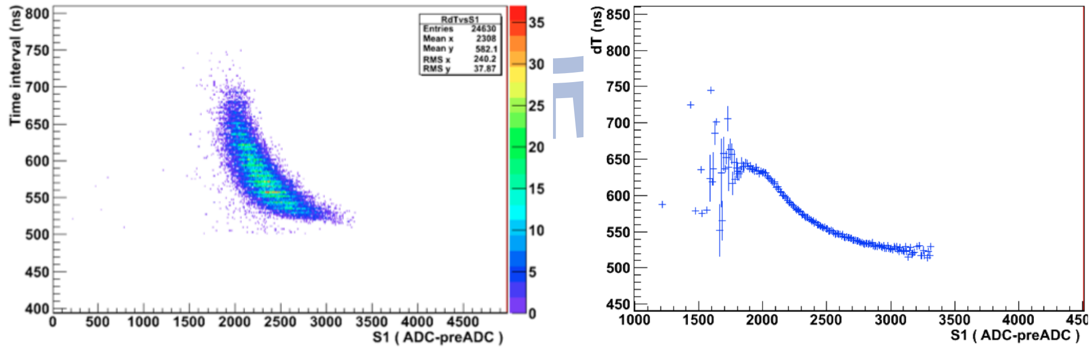

(e) The time interval between first and second signals versus the first charge (ADC-pedestal) for LED drive voltage at 7.9v

(f) The projection from the left figure.

Figure 3.13: The ringing cases

pulse and the beginning of ringing is around 510 ns.

3.1.4 Duplicated Hits

When the channel has a hit, FEE starts the ADC peak-finding process. Sometimes, it records the same ADC value, which is called duplicated hits, as shown in the Fig 3.14. These cases are caused by the closely hits. Fig 3.15 are the electronic simulation for the closely spaced hits. In the left panels of Fig 3.15, the charge for each pulse is one p.e.. The right panels are the shaped signals. The blue and red lines are the peak-finding range. There are four methods to improve the hit charge calculation:

- Second hit kept, preADC2 unchanged.
- Second hit kept, set preADC2 = preADC1.
- Second hit charge-corrected.
- Second hit discarded.

The reconstructed and true charge ratio are calculated and shown in Fig 3.16. Fig 3.17 shows the algorithms for the judgment process.

3.2 Vertex Reconstruction

The energy reconstruction process is used to correct the non-uniformity effect. In Daya Bay experiment, we have two methods for the event reconstruction, charged-weighted mean and charge templates. For the charged-weighted mean method, the weekly calibration source ^{60}Co was placed at different positions along the ACUA, ACUB and ACUC to study the energy response versus vertex; while the charge templates are based on simulation method and verified by the calibration source, ^{60}Co, and spallation neutrons.

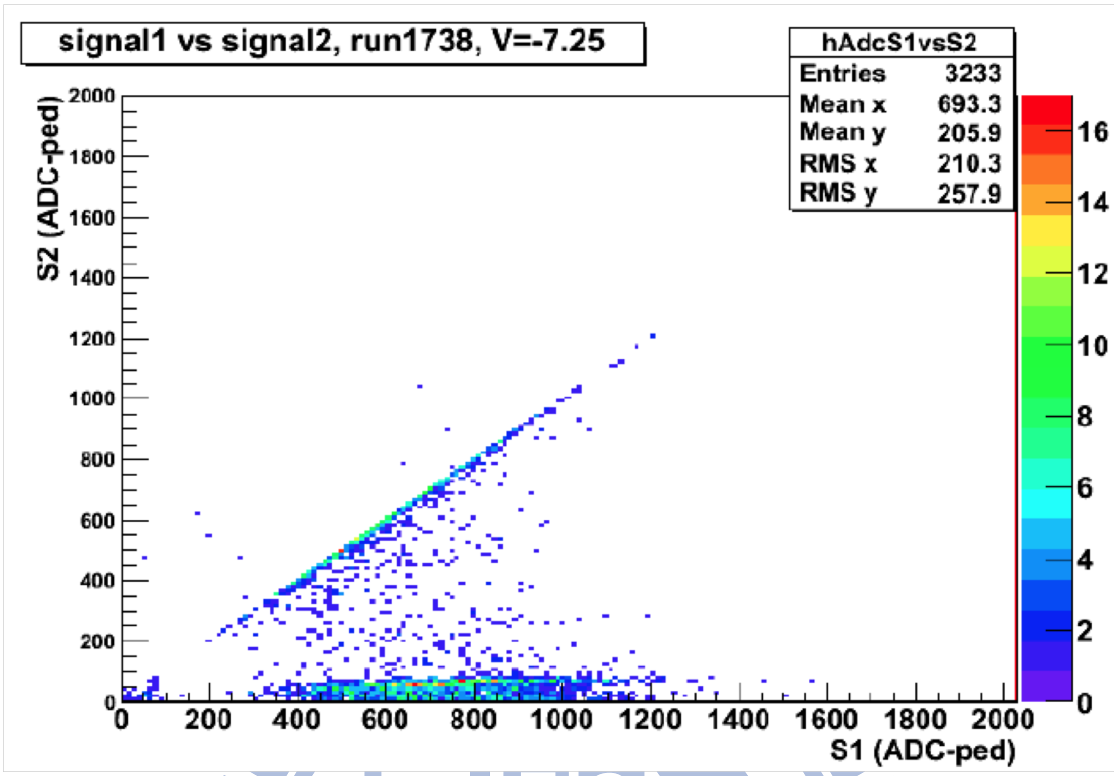

Figure 3.14: The second pulse versus first pulse.

3.2.1 The vertex reconstruction by charged-weighted mean (charge center) [28]

The definition of the charged-weighted mean is given by

$$x_{COC} = \frac{\sum_i^{PMTs} Q_i x_i}{\sum_i^{PMTs} Q_i}, \tag{3.6}$$

where i is the index of 8" PMTs in AD, which runs from 1 to 192, Q_i is the charge detected at each PMT, and x_i is the location of each PMT in AD.

However, there exists a large bias in this definition. This bias can be corrected by the an empirical model obtained from the Monte-Carlo simulations.

The reconstructed vertex is

$$R_{rec} = C_1 \times R_{COC} - C_2 \times R_{COC}^2, \tag{3.7}$$

$$Z_{rec} = (Z_{COC} - C_3 \times Z_{COC}^3) \times (C_4 - C_5 \times R_{COC}). \tag{3.8}$$

with $R_{rec} = \sqrt{x^2 + y^2}$ and $Z_{rec} = z$, the parameters, C_i, are obtained by performing fitting

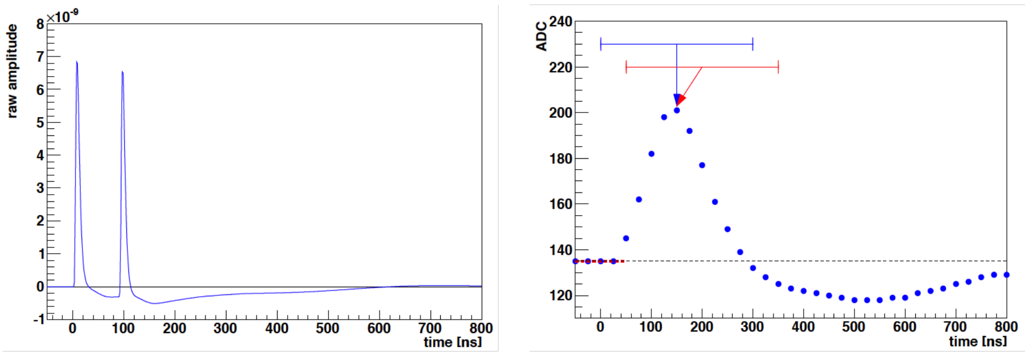

(a) Raw signals at $\Delta t = 50\ ns$ (b) Shaped signals at $\Delta t = 50\ ns$

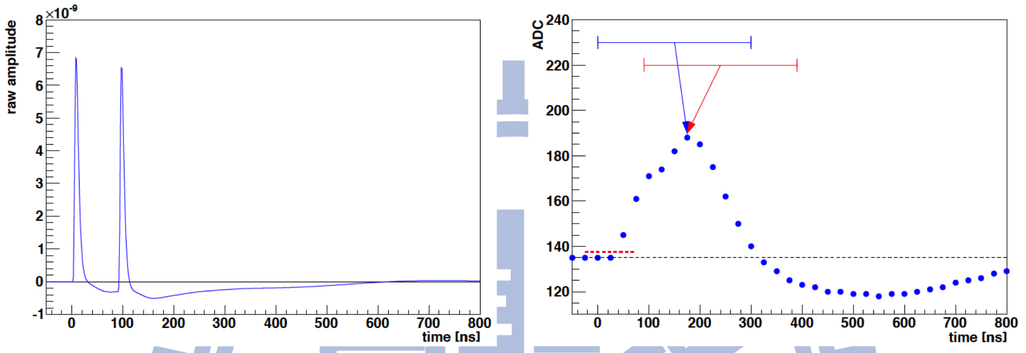

(c) Raw signals at $\Delta t = 90\ ns$ (d) Shaped signals at $\Delta t = 90\ ns$

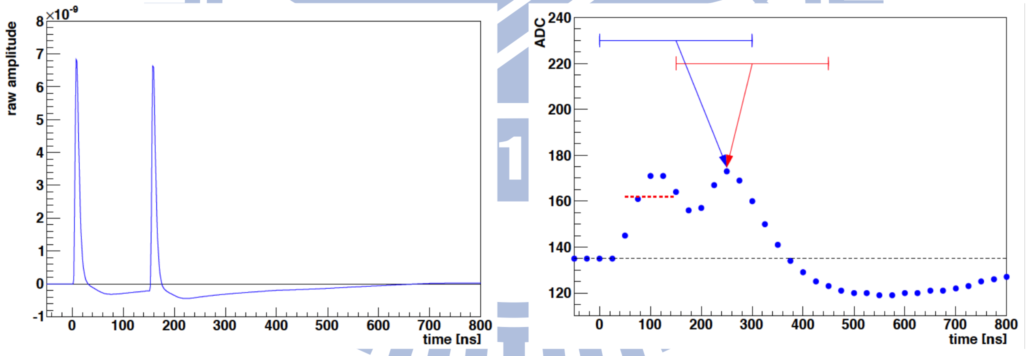

(e) Raw signals at $\Delta t = 150\ ns$ (f) Shaped signals at $\Delta t = 150\ ns$

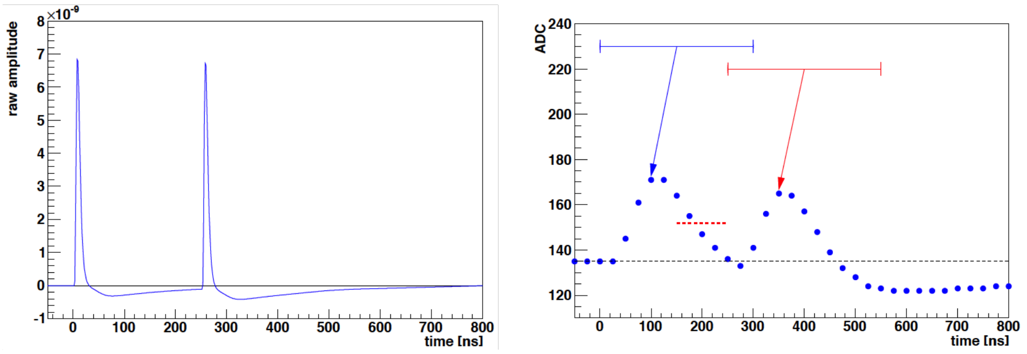

(g) Raw signals at $\Delta t = 250\ ns$ (h) Shaped signals at $\Delta t = 250\ ns$

Figure 3.15: Raw signals versus shaped signal for different hit separation times.

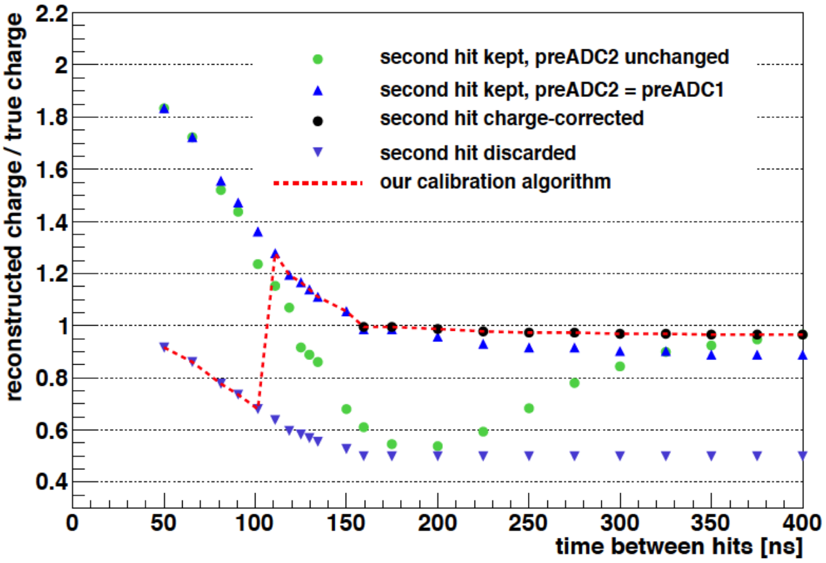

Figure 3.16: The performance of the different calibration algorithms.

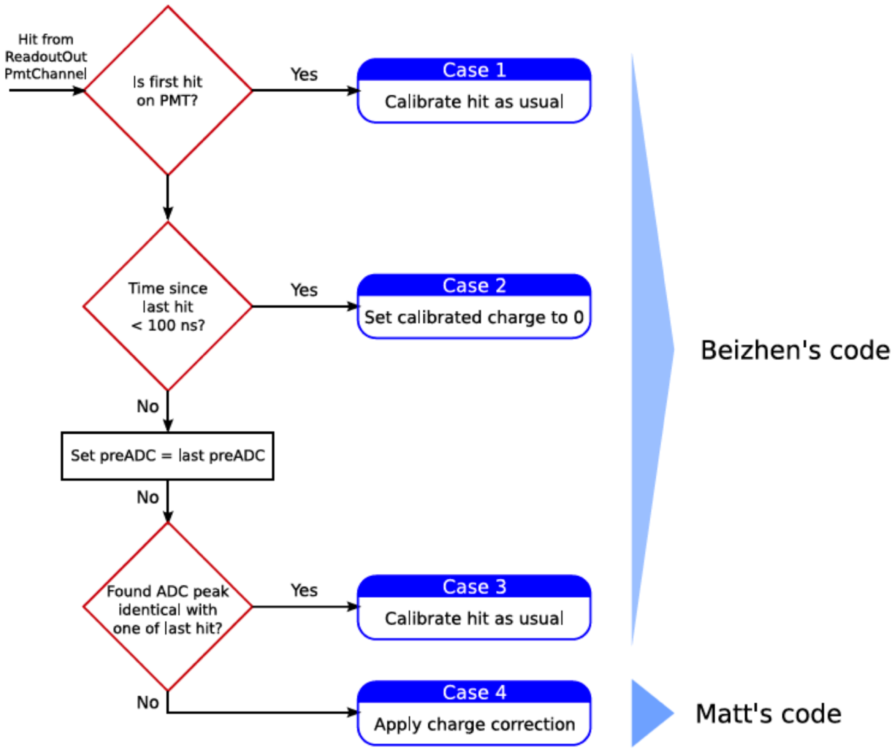

Figure 3.17: The algorithms for the different closely hits. There are four cases. The first condition is to judge if the current signal is the first hit on PMT. If the first conditions are satisfied(Case1), then the signal will be calibrated as usual. If "NOT", it then judges the time interval since last hit. If the time interval is smaller than 100 ns(Case2), than set the calibrated charge to 0. If the time interval is larger than 100 ns, it then judges whether the two signals are identical or not. If the ADC value for two signals are the same(Case3), the calibration process is as usual. If ADC values are different, it then applies the charge correction.

to the ^{60}Co calibration data at different positions and taking the average for different ADs.

So, the energy correction function is

$$f(R,Z) = (1 + C_R \times R^2) \times (C_{Z1} + C_{Z2} \times Z + C_{Z3} \times Z^2 + C_{Z4} \times Z^3), \tag{3.9}$$

with $C_R = 3.3762 \times 10^{-8}$, $C_{Z1} = 1.0005$, $C_{Z2} = -1.002 \times 10^{-5}$, $C_{Z3} = -1.894 \times 10^{-8}$, and $C_{Z4} = -1.758 \times 10^{-13}$. Figure 3.18 shows the relation between correction factor and the vertex.

3.2.2 The vertex reconstruction by charge templates [29]

The independent method is looking the charge distribution on each PMT. These distributions are described by three parameters, (r^2, z, ϕ), and divided into $20 \times 20 \times 40$ bins, where $r^2 = x^2 + y^2$ and $\phi = \arctan(y/x)$, as shown in Fig 3.19. The IBD events are simulated in the inner and outer acrylic vessels, 3 m and 4 m regions, of Daya Bay near site detector. The positron events are selected with the time interval between trigger and the true neutrino interaction time less than 0.5 μs.

The reconstruction vertex is estimated by the interpolation of the χ^2 distribution, as shown in Fig 3.20. Such a χ^2 value is defined as

$$\chi^2 = 2 \sum_i^{PMTs} [N_i^{exp} - N_i^{obs} + N_i^{obs} \ln(\frac{N_i^{obs}}{N_i^{exp}})], \tag{3.10}$$

where N_i^{obs} is the observed number of photo-electrons and $N_i^{exp}(r^2, z, \phi)$ is the expected number of photo-electrons from the simulation. To find the best fit for the vertex point, the first step is to find the minimum value of the χ^2. Then, the interpolation process for the χ^2 at the neighboring grid points are applied. The best fit of the vertex is used to put into the energy reconstruction formula. The expected resolution for charge templates are $\sim$ 7 cm for r and $\sim$ 9 cm for z.

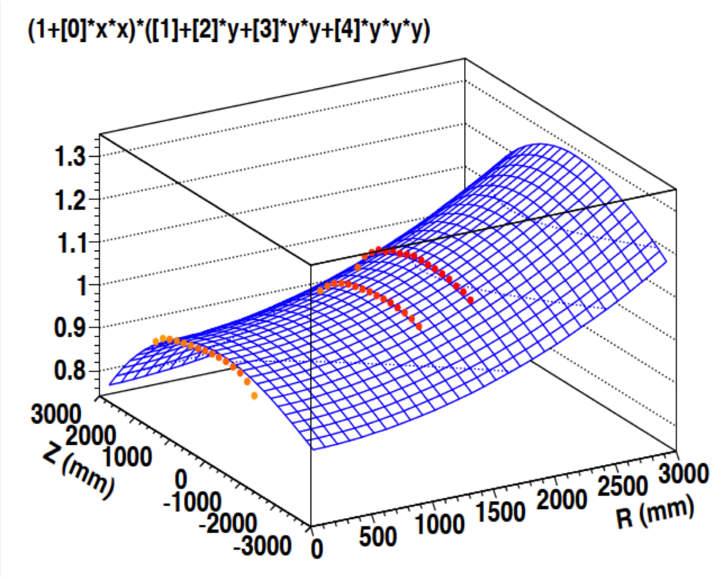

Figure 3.18: The relation between energy correction function and vertex. [28]

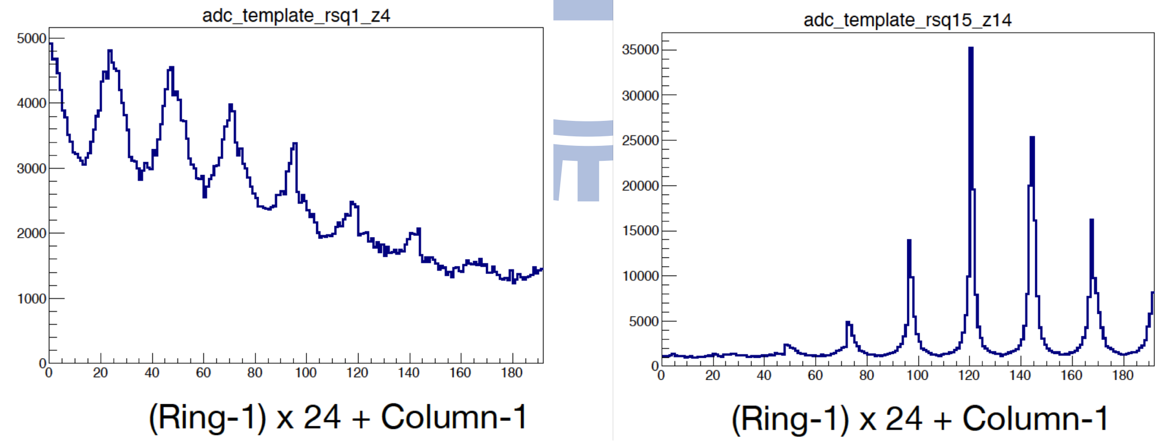

Figure 3.19: Examples of charge templates. The left one is the charge distribution on each PMT, which is named by $(Ring\ no.\ -1)\times 24\ +\ Column\ no.$ The left sample is for $0.2 < r^2 < 0.4\ m^2$ and $-1.2 < z < -1.0$m. The right sample is for $3.0 < r^2 < 3.2\ m^2$ and $0.8 < z < 1.0$ m [29].

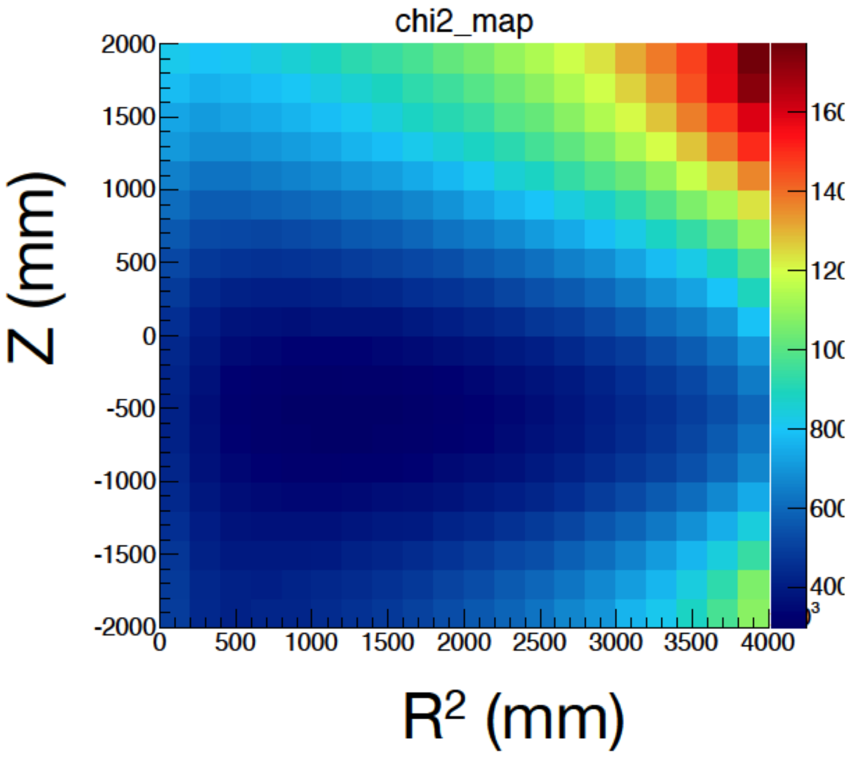

Figure 3.20: An example of the χ^2 distribution for each grid point [29].

3.3 Energy Reconstruction

To obtain the reconstructed energy, E_{rec}, the first step is to convert the ADC values from each PMT into the p.e. unit by the PMT calibration constant. The total charge, Q_{total}, deposited in AD is calculated by the first hits on each PMT, which arrive in the time window between -1650 and -1250 ns. These charges are converted into a physical energy scale by the visible energy calibration constant, C. The relation function is

$$E_{vis} = \frac{Q_{total}}{C} \tag{3.11}$$

Finally, the correction to the detector non-uniformities is applied on the visible energy. In Daya Bay experiment, there are two independent reconstruction algorithms, one is based on the ^{60}Co source, another is based on the spallation neutrons.

3.3.1 Energy reconstruction based on ^{60}Co source

As mentioned in the previous chapter, there are three automatic calibration units (ACUs) on the top of the AD detector. These instruments can be used to scan the vertical positions for the non-uniformity study. After the background subtraction, the ^{60}Co spectrum is fitted with a Crystal ball function plus a Gaussian. The visible energy calibration constant can be calculated by dividing the peak position in p.e. by 2.506 MeV. The calibration constant is around 162 p.e./MeV.

For different particles, the energy responses are different. Therefore, the energy reconstruction functions are different. For the neutron energy scale, the energy reconstruction function is

$$E_{rec} = C_n^{Co} \cdot \frac{E_{vis}}{f(R, Z)}, \tag{3.12}$$

where E_{vis} is defined by Eq (3.11), C_n^{Co} is a constant determined by the ratio of the neutron peak of the Am-^{13}C source to the ^{60}Co peak.

3.3.2 Energy reconstruction based on spallation neutrons

Spallation neutrons are one type of products from cosmic muons. They can be captured on hydrogen or gadolinium and emit 2.22 MeV and 8.05 MeV gammas, respectively. Such a gamma emission is uniform within each AD. Hence the spallation neutron is a good source for the relative energy scale calibration.

To select the spallation neutron events, the instrumental background from the spontaneous light emission of PMT should be rejected. This procedure will be described in the next chapter. The readout signal is tagged as a muon if the nominal charge is greater than 4000 p.e. or if the number of inner water pool or outer water pool PMT hits are greater than 10 or 12, respectively. The timing criteria requires that the signal time window is between 20 μs and 1000 μs after the muon event; for the background, these are within 1020 μs and 2000 μs after the muon event. The energy spectrum of the spallation neutron is obtained by subtracting the background spectrum from the signal spectrum. The peak value of the neutron capture on the gadolinium is from the spectrum fitting with a double Crystal Ball function. Then, the visible energy calibration constant can be calculated by dividing the peak value by 8.05 MeV. The value is around 168 p.e./MeV.

The corrected energy (E^{corr}) is defined by [30]

$$E^{corr} = \frac{8.05}{R(r)} \times \frac{8.05}{R(z)} \times E_{vis}^{raw}, \tag{3.13}$$

where $R(r)$ and $R(z)$ are the energy response function,

$$R(r) = 7.74687 - 0.129958r + 0.3355034r^2 - 0.0337577r^3, \tag{3.14}$$

$$R(z) = 8.09949 - 0.11702z - 0.124515z^2 + 0.024570z^3, \tag{3.15}$$

r and z are from the best fit of the charge template results.

3.4 Energy resolution

The resolution of the energy reconstruction is evaluated around the peak position of the calibration sources, ^{60}Co, ^{68}Gd and AmC. The resolution curve is shown in Fig 3.21 which is fitted to be $(7.5/\sqrt{E_{rec}(MeV)} + 0.9)\%$.

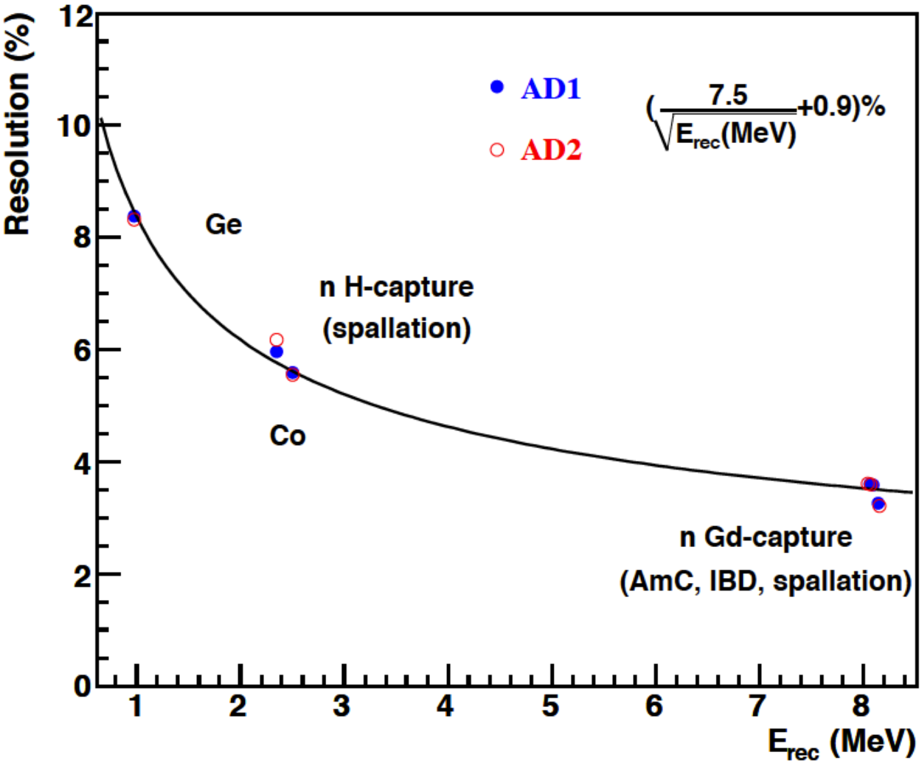

Figure 3.21: The energy resolution in the Daya Bay antineutrino detector [24].

Chapter 4

Event Selection

The IBD candidates are selected by the prompt-delayed coincident signals. The prompt signals are between 1.5 MeV and 12 MeV and the delayed signals are within the 3 σ range around the neutron capture peak. Before selecting the coincident pairs, the instrumental background from the spontaneous light emission by PMTs (“flasher”) is removed from the data. We then remove the muon background. Finally, the IBD pairs are selected and the selection criteria for the distance between the prompt and delayed signals are applied. The IBD event selection criteria are shown in Table 4.1.

Trigger		NHit or ESum
Instrumental background-Flasher	8 inch PMT	Ellipse cut
	2 inch PMT	MaxQ/2InchQ <100
Muon veto	Pool muon	400 μs
	AD muon	800 μs
	Shower muon	$1s$
Event selection window T_c		400 μs
Prompt Energy E_p		[1.5, 12] MeV
Delayed Energy E_d		3 σ
Distance cut		500 mm

Table 4.1: The summary of the IBD event selection.

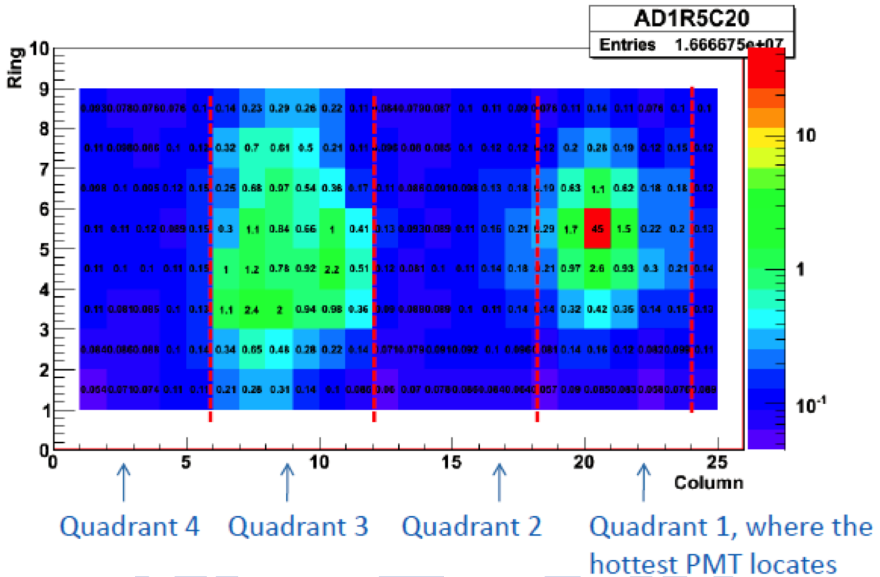

Figure 4.1: The flasher events on PMT pattern [24].

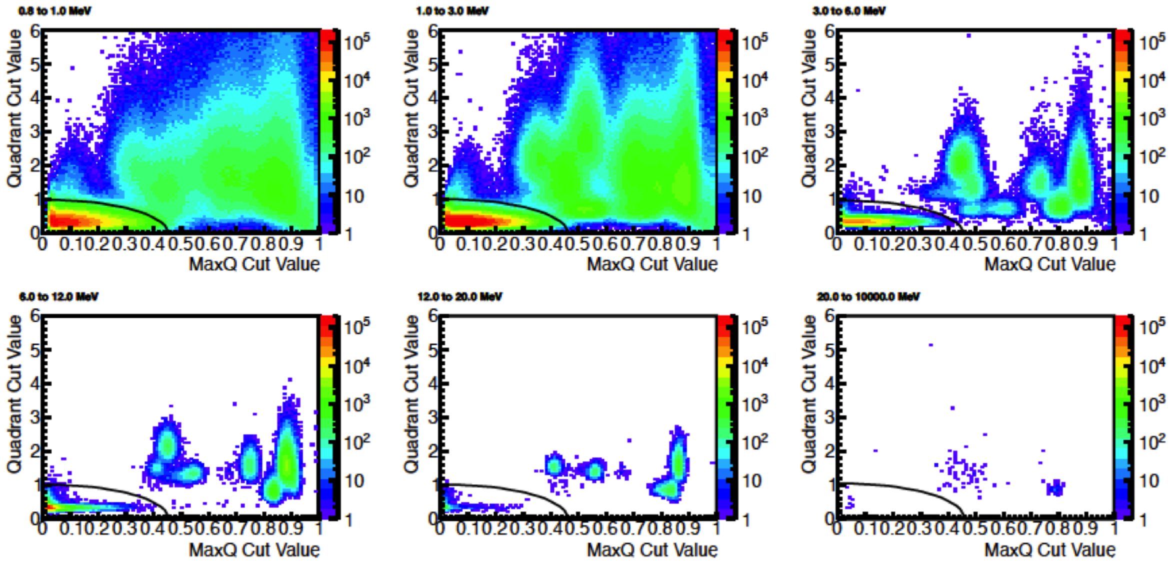

Figure 4.2: The distribution of $Q_{quadrant}$ versus $MaxQ$ for different energy ranges [31].

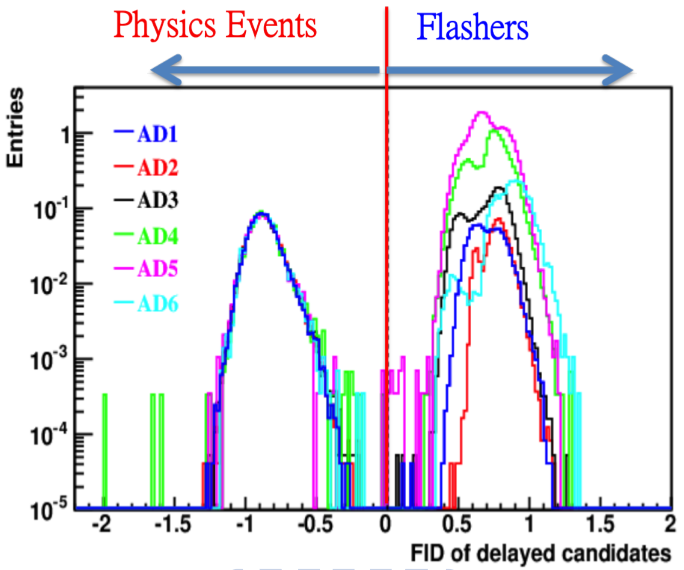

Figure 4.3: The events with FID smaller than 0 are treated as the physics event and those with FID larger than 0 are flasher events [24].

4.1 Flasher Cut

There are about 5% instrumental background events from the PMT. Some PMTs emit light spontaneously due to the electronic discharge in dynodes, which is referred to as "flasher". The observed energy for these events is between threshold and 100 MeV.

One can reject these backgrounds with their features. As it is shown in Figure 4.1, there are two hot PMT clusters in the hit map. The flashing PMT has the largest charge. We can define a factor $MaxQ = Q_{max}/Q_{total}$ and name the flasher area as Quadrant1(Q_1) and the others as Q_2, Q_3 and Q_4, respectively. The second hot area is Q_3. One may define another factor $Q_{quadrant} = Q_3/(Q_2 + Q_4)$.

$Q_{quadrant}$ versus $MaxQ$ are shown in Figure 4.2 for different energy ranges. Based on these, the flashers are identified as

$$\frac{Q^2_{quadrant}}{1.0} + (\frac{MaxQ}{0.45})^2 < 1, \tag{4.1}$$

which is known as "Ellipse Cuts". One can also use an equivalent criterion for flashers,

$$FID \equiv log_{10}(\frac{Q^2_{quadrant}}{1.0} + (\frac{MaxQ}{0.45})^2) < 0, \tag{4.2}$$

as shown in Figure 4.3.

After the flasher rejection, the inefficiency of antineutrino candidates is $0.024\% \pm 0.006\%$ $(stat)$.

4.2 Muon Veto

Cosmic muons produce backgrounds which fake IBD events. The secondary particles of the cosmic muons, such as spallation neutrons, ^{8}He and ^{9}Li, could mimic the antineutrino events. These muon-related events are rejected by vetoing the coincident windows. The muon types such as water pool muon (μ_{WP}), AD muon (μ_{AD}) and shower muon (μ_{shower}), are defined as follows:

- Water Pool Muon: the number of inner water pool (IWP) PMT hit is greater than 12 or the number of outer water pool (OWP) PMT hit is greater than 15.
- AD muon: the total visible energy deposit is more than 20 MeV in an AD
- Shower muon: the total visible energy deposit is more than 2.5 GeV in an AD

The muon veto windows depend on muon types. Any triggers in AD which are after μ_{WP} are vetoed by 400 μs. For μ_{AD}, the veto window is 600 μs; for μ_{shower}, the veto window is 1 s.

We disregard those events with muons occurring in the event selection window, as shown in the Figure 4.4(a). So, the total dead time (veto time) is veto window plus the event selection window, which will be described in the next section. If muon events occur very close in time, as illustrated by Figure 4.4(b), the effective veto window is between the first muon and the end of the second muon veto window. We then treat these two muon events as a "net" muon event. The muon veto efficiency is defined by

$$\varepsilon_m = 1 - \frac{\text{Veto Time}}{\text{Full time}}. \tag{4.3}$$

The muon event rate is defined by

$$R_\mu = 1 - \frac{\text{Total Net } \mu}{\text{Live time (Full time} - \text{Veto Time)}}. \tag{4.4}$$

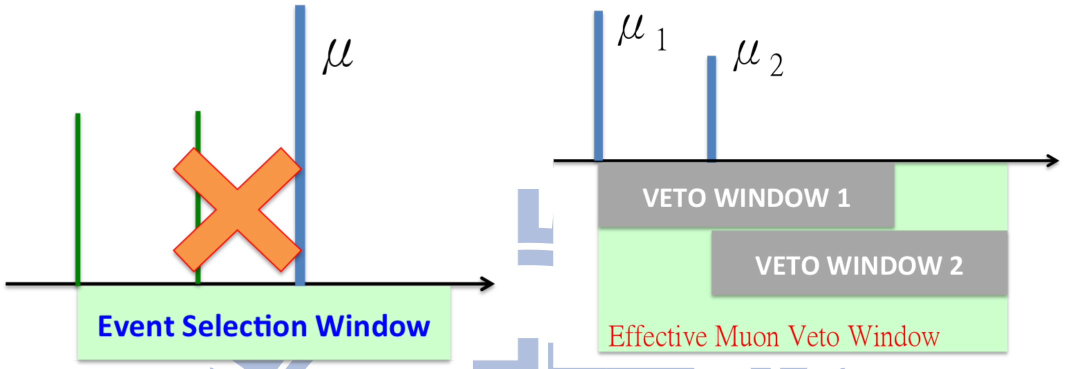

(a) A muon is in the event selection window.

(b) A latter muon is in the veto time window of the earlier one.

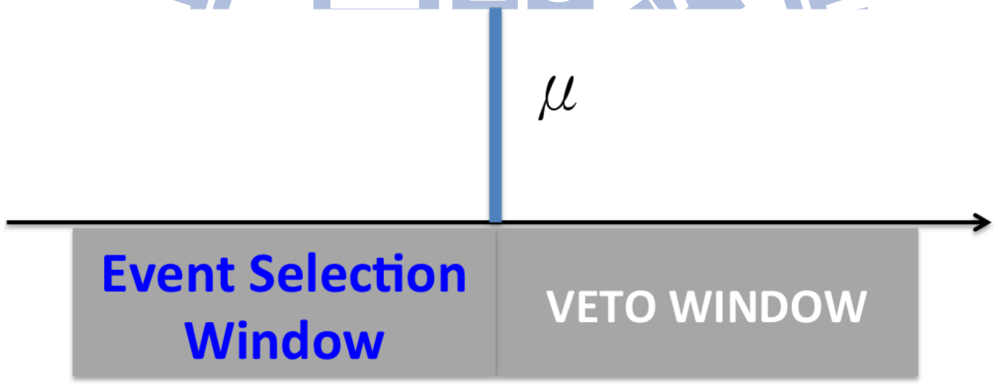

(c) The muon veto range

Figure 4.4: The green lines denote good events; the blue lines denote muon events. (a) Muon occurs within the event selection window. This type of events are disregarded in our analysis. (b) Two or more muons arrive very close in time, the later muon arriving in the veto window of the previous muon. In this case, we treat these two muons as a net muon. (c) The total dead time (veto time) is veto window plus the event selection window.

Figure 4.5 and Figure 4.6 are the muon veto efficiencies and the muon rate in all ADs from Dec 24, 2011 to Nov. 30, 2013.

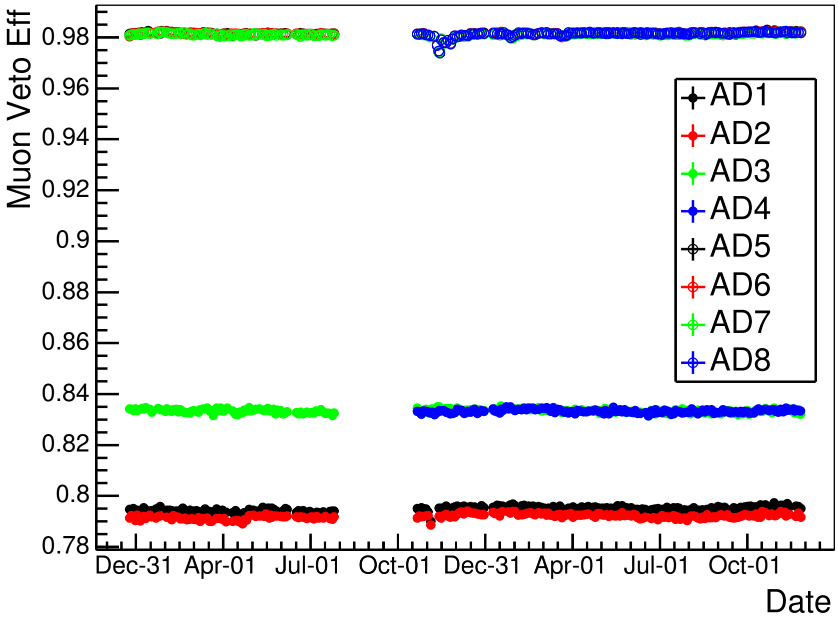

Figure 4.5: Muon veto efficiency for different ADs from Dec. 24, 2011 to Nov. 30, 2013.

4.3 Coincident Pair

An IBD event contains two sub-events, prompt and delayed sub-events. After removing the flashers, low energy events and muon veto, we treat the survival signals as 'good AD sub-events'. After finding the first 'good AD sub-event', the event selection window, T_s, is set to be 400 μs. Figure 4.7 illustrates the three cases. Only one sub-event appearing in the event selection window is called single. Two sub-events is called delay-coincident pair. Events consist of more than two sub-events are called multi-coincident events. Figure 4.12 shows the distribution of the prompt and delayed coincidence pairs in EH1. The signals of 8 MeV neutron capture on Gd can be clearly seen in the plot, and the signals of 2.2 MeV neutron capture on H can be identified when the prompt energy is greater than 3.5 MeV.

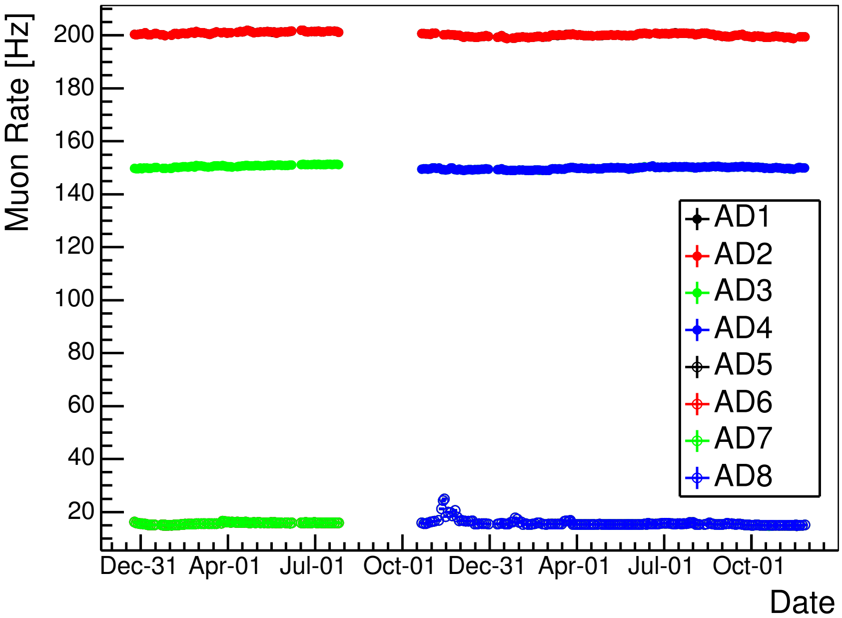

Figure 4.6: Muon rate from Dec. 24, 2011 to Nov. 30, 2013.

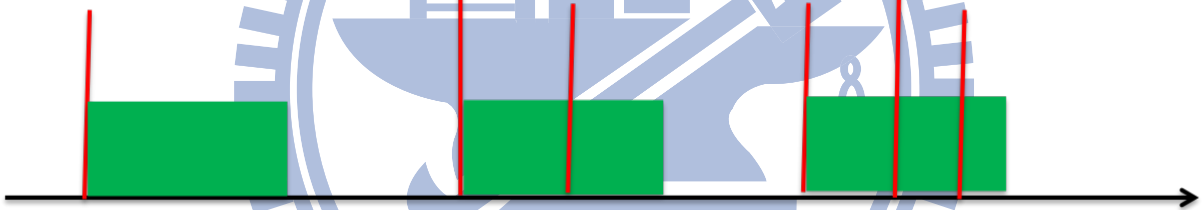

Figure 4.7: Multiplicity cases. The left one is called single event. The middle one is the delay-coincident pair. Three or more singles in a event selection window, for example the right one, is called multi-coincident events.

4.3.1 Low energy cut for prompt signal

In this analysis, the energy selection for prompt signal are between 1.5 MeV and 12 MeV. Figures 4.8 show the prompt and delay energy distribution within the 0.7 MeV and 4 MeV, where the left one is before the vertex cut and the right one is after the vertex cut. From these figures, the singles rate will be larger and increase the statistical error if we include the 0.7 MeV to 1.5 MeV region. Another reason for the low energy cut is that the correlated background from $^{219}\mathrm{Rn} -^{215}\mathrm{Po} -^{211}\mathrm{Pb}$, which emits the low energy $\beta - \alpha$, can affect the accidental background prediction. On the other hand, the lower energy region does not contribute to the IBD detection because the main energy for the reactor

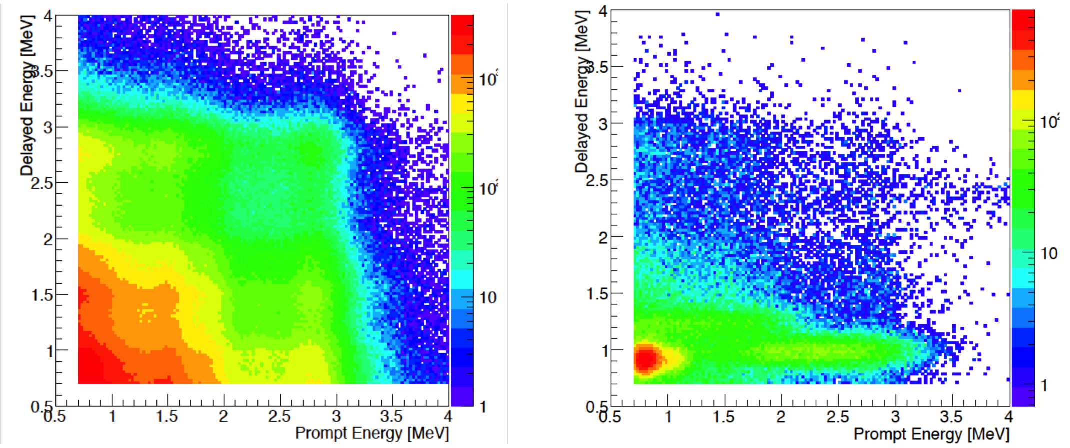

Figure 4.8: Energy distribution before (left) and after (right) the vertex cut in a special low energy 0.7 MeV study.

antineutrino is around 3 MeV to 4 MeV.

4.3.2 Event selection window

The neutron capture time for neutron capture on hydrogen is about 200 μs, and for Gd is about 30 μs. To understand the capture time for neutron capture on hydrogen, the following conditions are the same as Table 4.1 except

- The longer coincident window (T_c): 1500 μs.
- The prompt vertex reconstructed position: $|z| > 1700\ mm$ or $|z| < 1700\ mm$ but $r^2 > 2800 \times 10^3\ mm^2$.

The distribution were fitted with a flat background, N_{bkg}, and an exponential function which has been normalized,

$$F(t) = \frac{N \cdot e^{-\lambda \cdot t}}{\int_{T_-}^{T_+} e^{-\lambda \cdot t} \mathrm{d}t} + N_{bkg}, \tag{4.5}$$

where the integral region is between 0 s and 0.0015 s, λ is the capture time constant. Table 4.2 summaries the fitting results. From these results, the event selection window setting on 400 μs can get most of nH events.

AD NO.	λ	lifetime (μs)
0	4801.00 ± 21.80	208.3
1	4656.82 ± 28.95	214.7
2	4696.60 ± 28.95	212.9
3	4683.87 ± 29.17	213.5
4	4591.33 ± 34.27	217.8
5	4778.08 ± 129.24	209.3
6	4936.50 ± 132.67	202.6
7	4619.14 ± 128.03	216.5
8	4839.49 ± 164.85	206.6

Table 4.2: The summary of the neutron capture time fit. The AD0 is the Monte Carlo result.

4.3.3 Singles

Only one event appearing in the event selection window is called single. The number of singles, $N_{singles}$, is defined as

$$N_{singles} = \frac{N_{singles-up} + N_{singles-low}}{2}, \tag{4.6}$$

where $N_{singles-up}$ is the total number of all sub-events excluding muon events. $N_{singles-low}$ is defined as the number of events which contains only one sub-event and two sub-events with the relative distance larger than 500 mm. Then, the single rate is given by

$$R_s = \frac{N_{singles}}{\text{Live time (Full time} - \text{Veto Time)}}. \tag{4.7}$$

Figure 4.11 is the singles rate from Dec. 24, 2011 to Nov. 30, 2013. The remaining natural radioactivities in the detector is the main contribution to the singles' rate. The rate decreases with the time since the beginning of data taking.

4.4 Distance Cut

Figure 4.13 shows the distribution of the distance between the prompt and delayed signals. The black curve is the distance distribution with the energies of the delayed signals between 6 and 12 MeV. The red one is the distance distribution of those events with the prompt signals greater than 3.5 MeV and the delayed signals less than 3 MeV. For the blue curve, both prompt and delayed signals are less than 3 MeV. It is clear that, for isolating the neutron capture on hydrogen signals, i.e., events described by the red curve, one can impose a distance cut at 500 mm. This cut removes most of the events in blue curve and therefore improve the signal-to-background ratio, as shown in Figure 4.14. The ratio is smaller than 1 at 1000 mm which means the background is larger than signal. However, the ratio is larger than 1 at 500 mm. After applying the distance cut, Figure 4.15 shows a clear structure at 2.2 MeV which is the signature of neutron captured by hydrogen.

4.5 Summary

Table 4.3 shows the summary of the full time, live time, singles rate R_μ and veto time. In addition, the efficiencies are discussed in Chap. 6. After the distance cut, the number of IBD candidates is obtained from the number of events, which pass the prompt (between 1.5 MeV and 12 MeV) and delayed energy (3σ from the neutron capture range) cuts .

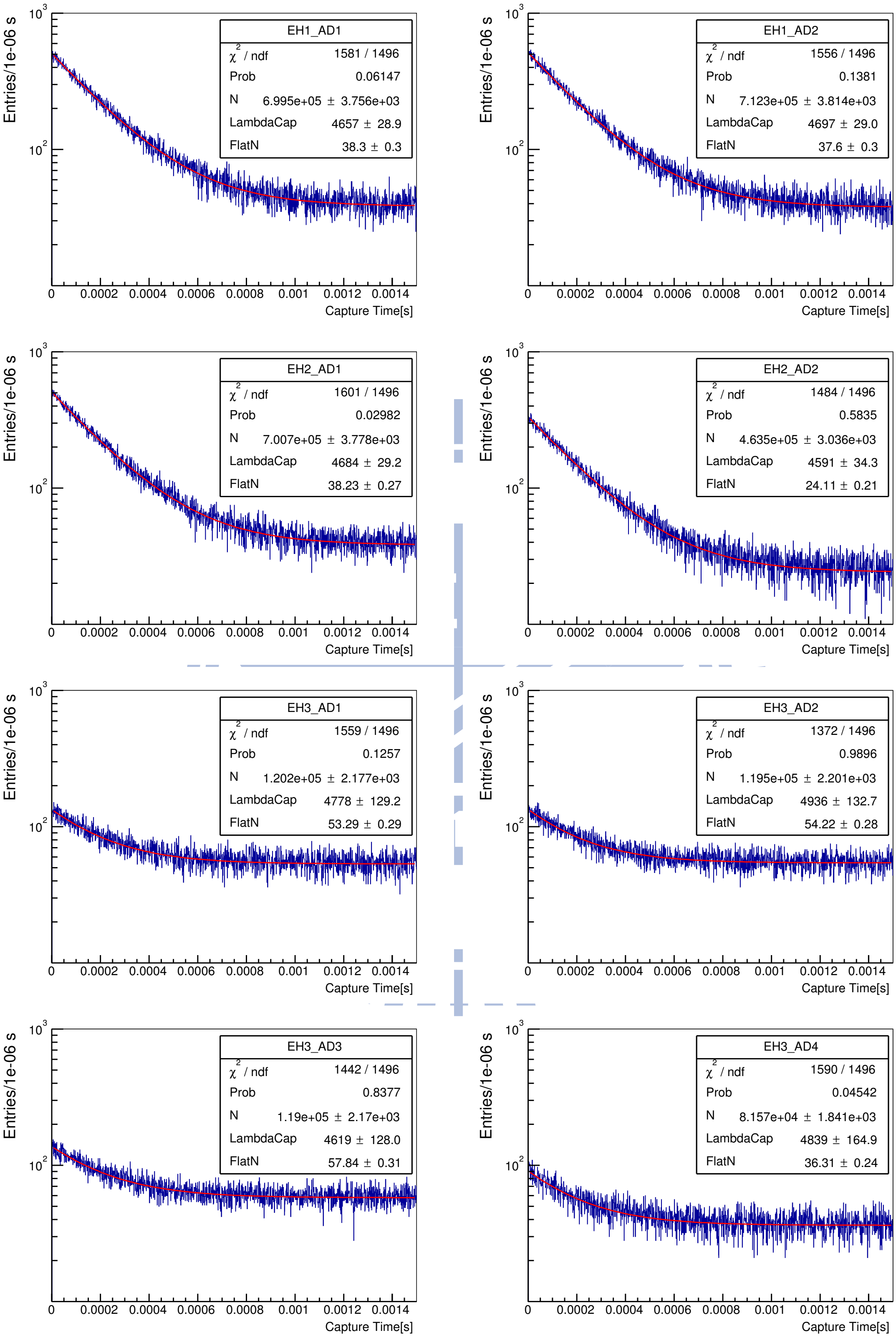

Figure 4.9: The neutron capture time distribution in LS region.

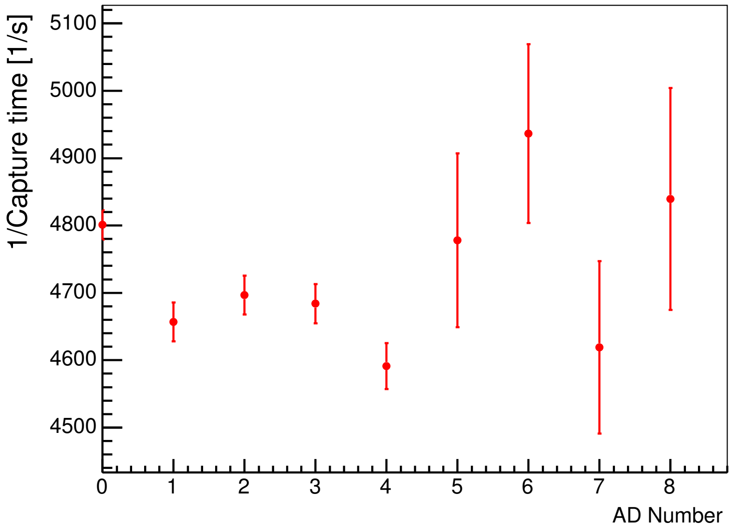

Figure 4.10: The fitting results of neutron capture time.

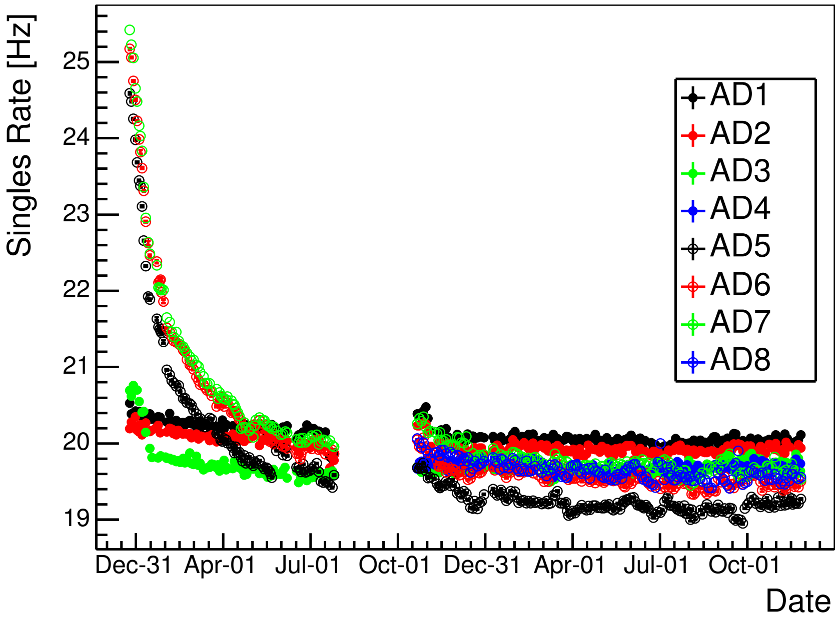

Figure 4.11: Singles' rate [Hz] per day from Dec. 24, 2011 to Nov. 30, 2013.

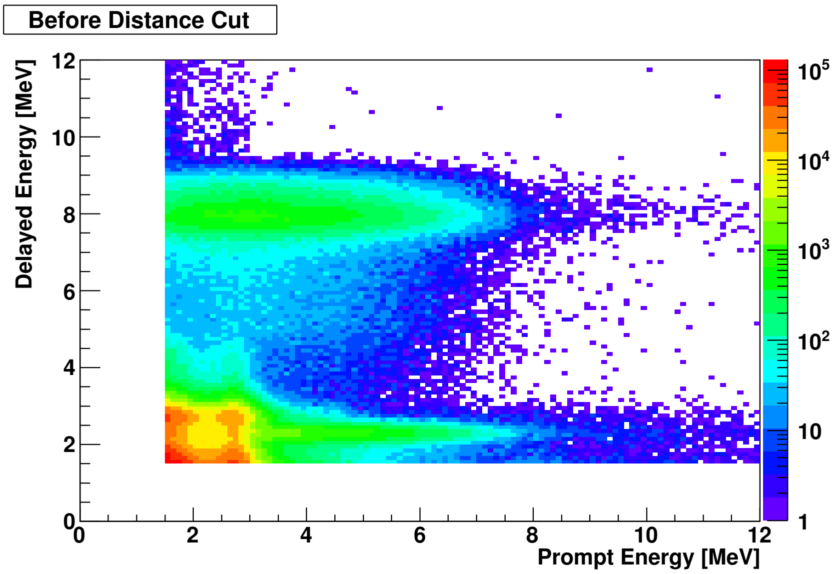

Figure 4.12: The energy distribution of the prompt and delayed coincidence pairs in EH1.

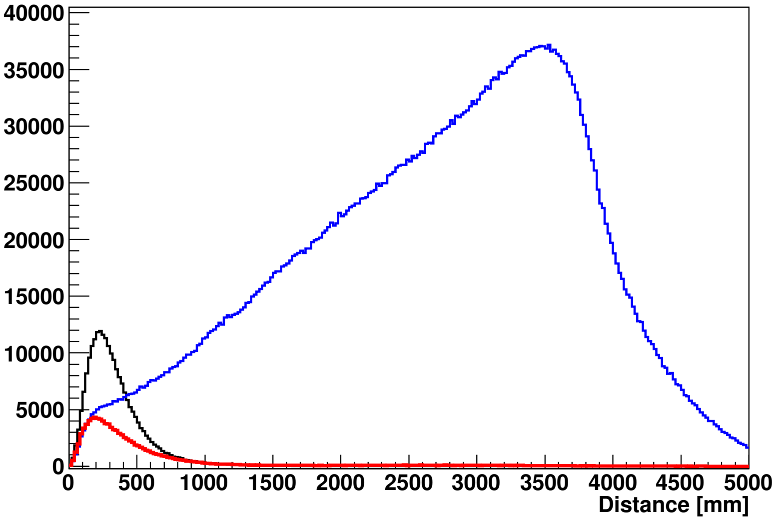

Figure 4.13: The prompt-delayed distance distributions for different energy ranges. Black: E_d within 6 to 12 MeV. Red: E_p greater than 3.5 MeV and E_d are less than 3 MeV. Blue: both E_p and E_d less than 3 MeV.

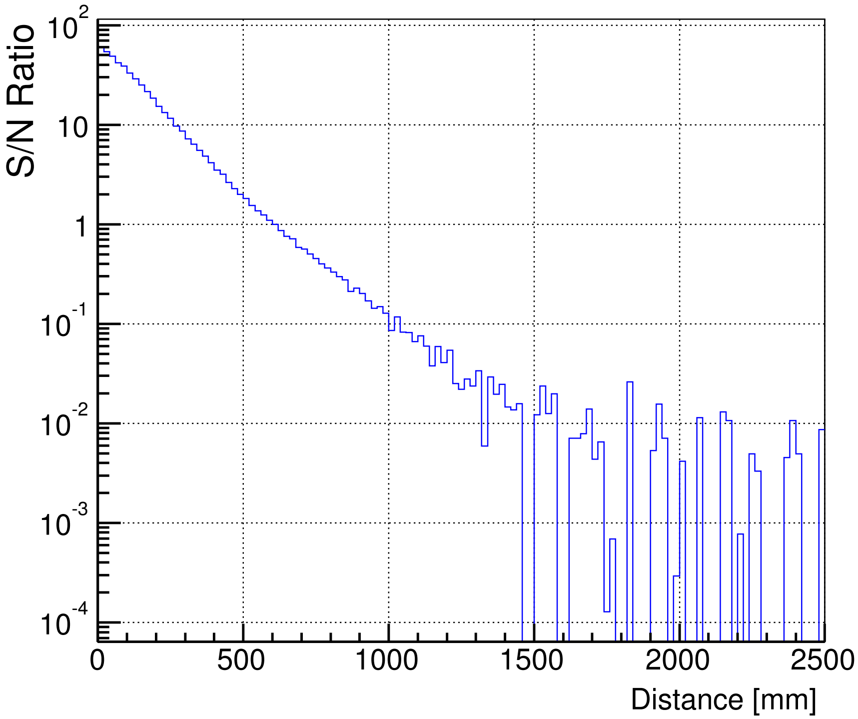

Figure 4.14: The signal to noise ratio versus distance

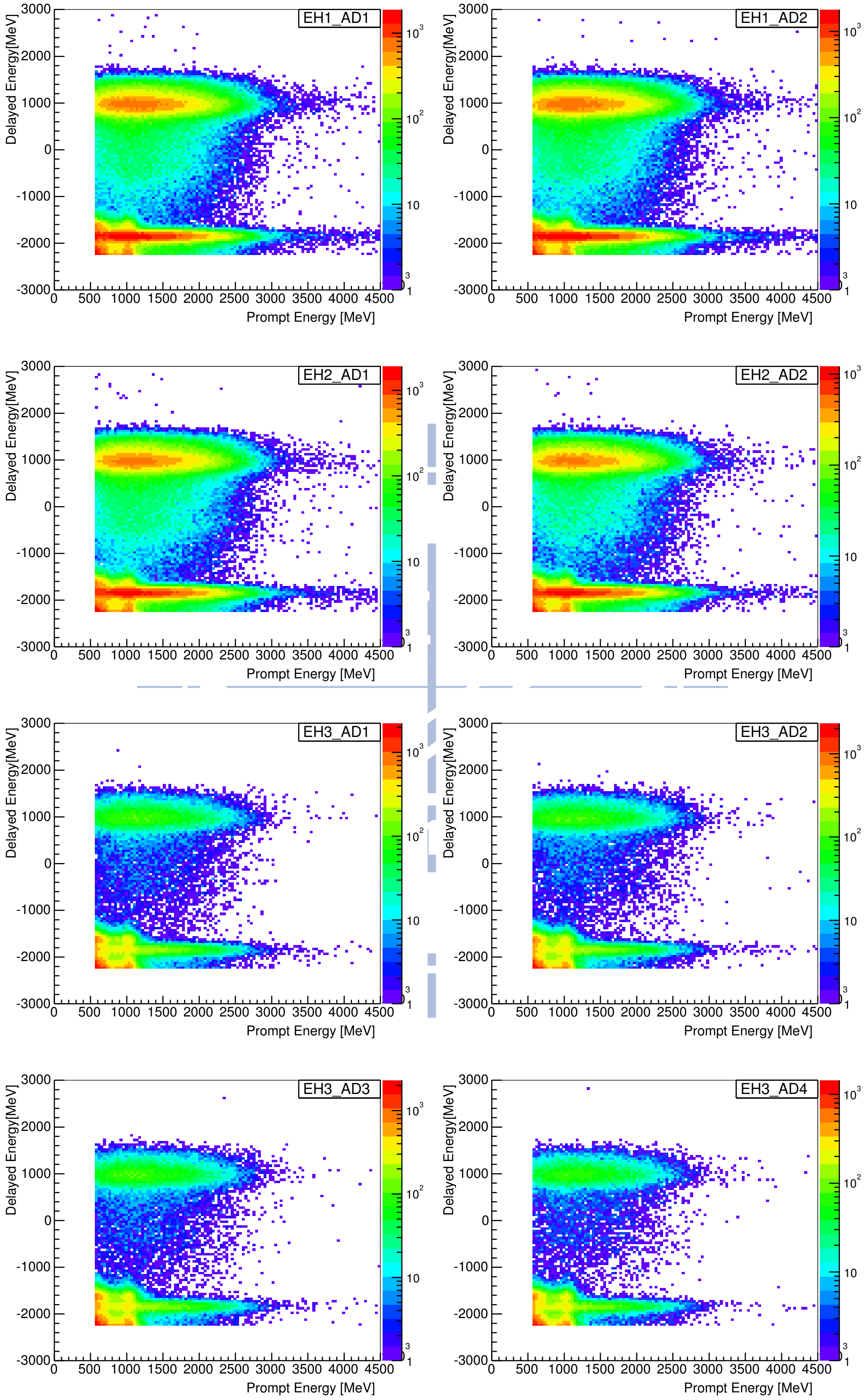

Figure 4.15: The energy distribution of the prompt and delayed coincidence pairs after the distance cut.

Dec 24, 2011 to Jul 28, 2012								
	AD1	AD2	AD3	AD4	AD5	AD6	AD7	AD8
Fulltime (day)	190.9954	190.9954	189.6464	-	189.7857	189.7857	189.7857	-
Livetime (day)	151.7717	151.1194	158.1292	-	186.2796	186.2791	186.2131	-
R_μ (Hz)	201.0335	201.0352	150.6092	-	15.7275	15.7276	15.7275	-
Veto (day)	39.22	39.88	31.52	-	3.51	3.51	3.57	-
ε_μ	0.7946	0.7912	0.8338	-	0.9815	0.9815	0.9812	-
ε_m	0.9836	0.9837	0.9842	-	0.9832	0.9827	0.9827	-
$\varepsilon_\mu \varepsilon_m$	0.7816	0.7783	0.8206	-	0.9651	0.9646	0.9642	-
Oct 19, 2012 to Nov 30, 2013								
Fulltime (day)	374.4473	374.4473	378.4070	378.4070	372.6850	372.6850	372.6850	372.6850
Livetime (day)	297.7808	296.6958	315.3781	315.3216	365.7587	365.7445	365.6710	365.7509
R_μ (Hz)	199.9615	199.9605	149.8041	149.8022	15.7566	15.7567	15.7566	15.7566
Veto (day)	76.67	77.75	63.03	63.09	6.93	6.94	7.01	6.93
ε_μ	0.7953	0.7924	0.8334	0.8333	0.9814	0.9814	0.9812	0.9814
ε_m	0.9844	0.9845	0.9847	0.9846	0.9848	0.9846	0.9844	0.9845
$\varepsilon_\mu \varepsilon_m$	0.7829	0.7801	0.8207	0.8205	0.9665	0.9662	0.9659	0.9662

Table 4.3: The summary of the data taking time, muon veto time and efficiency, multiplicity cut efficiency ε_m (to be discussed in Chap. 6), and IBD candidates.

Chapter 5

Background Study

After applying the antineutrino selections discussed in the previous chapter, the remaining backgrounds can be divided into two categories, uncorrelated background and correlated background. The former background events are 'accidentally' passing the IBD event selection and mimic IBD event. We therefore name this kind of events as accidental background.

Another kind of background is called correlated background. The coincident pairs are from the same event and passing the event selection. These are from fast neutron and β-n decay of the cosmogenic $^9Li/^8He$ source. They provide the prompt- and delayed-like signals. Besides, the gamma emission from the neutron capture also affects the IBD detections. This background can come from the calibration source $^{241}Am -^{13} C$. These are summarized in the Table 5.1. The background rate is calculated by

$$R_i = \frac{N_i}{T_{live} \cdot \varepsilon_{multi}}, \tag{5.1}$$

where i is the type of correlated background, N_i is the number of correlated background, T_{live} is live time and ε_{multi} is the multiplicity cut efficiency.

Backgrounds			Mimic Process	
			Prompt	Delayed
Uncorrelated	Accidental		Any two triggers within the time window	
Correlated	Cosmic Muon	Fast Neuton	Neutron collides/stops in target	Neutron Captures
		^{9}Li/^{8}He	β -decay	
	Calibration source	AmC	Neutron inelastic scattering	

Table 5.1: The IBD background summary.

5.1 Uncorrelated Background

5.1.1 Accidental Background

The accidental backgrounds are from any double coincidence events, which are accidentally passed the IBD selection, and there is no correlation between them. After the distance cut, most accidental backgrounds are suppressed. As shown in Figure 4.15, there still remain some accidental backgrounds. To get more ‘pure’ spectrum, the generated accidental background spectrum are used to be subtracted from the Figure 4.15. Figure 5.1 illustrates the process of generating the accidental background. We first choose a sample of singles from one run and divide it into two parts. The first half is used as the prompt sub-events and the other is used as the delayed sub-events. Those signals are not correlated because they are separated by around ten hours. They are required to pass the relative distance cut since the singles’ rate and spectra are correlated with their vertex positions. For the statistics purpose, we exchange prompt and delayed signals and apply the same IBD cuts again. The generated accidental spectrum is shown in Figure 5.2.

Figure 5.3 shows the process of the accidental background subtraction,

$$\text{Figure } 5.3(c) = \text{Figure } 5.3(a) - A \cdot \text{Figure } 5.3(b), \tag{5.2}$$

where Figure 5.3(a) is the spectrum after the 500 mm distance cut, Figure 5.3(b) is the generated accidental spectrum and Figure 5.3(c) is the background subtracted spectrum. A is the scale factor, which is given by

$$A = \frac{R \cdot T_{live}}{N_{ABS-tot}}, \tag{5.3}$$

where R is the random coincidence rate of two single events given by [32]

$$\begin{aligned} R = R_s \times \Bigg\{ & \frac{R_\mu}{R_s + R_\mu}[1 - \mathrm{e}^{-(R_s+R_\mu)T_c}] + \mathrm{e}^{-(R_s+R_\mu)T_c} \\ & + \frac{R_s}{R_s + R_\mu}\mathrm{e}^{-R_\mu T_c}[1 - \mathrm{e}^{-(R_s+R_\mu)T_c}] - \frac{R_s}{2R_s + R_\mu}\mathrm{e}^{-R_\mu T_c}[1 - \mathrm{e}^{-(2R_s+R_\mu)T_c}] \Bigg\} \\ & \times [R_s T_c \mathrm{e}^{-R_s T_c}], \end{aligned} \tag{5.4}$$

with R_s is the singles rate and $N_{ABS-tot}$ is the total number of accidental background spectrum (ABS).

The number of IBD candidates, N_{IBD}, is calculated from each bin, i, as

$$N_{IBD,i} = N_{dis-cut,i} - A \times N_{ABS-tot,i}, \tag{5.5}$$

where $N_{dis-cut}$ is the number of events after the distance cut.

The ratio of the accidental events which pass the IBD selection, $N_{ABS-cut}$ to $N_{ABS-tot}$ is represented by

$$\varepsilon = \frac{N_{ABS-cut}}{N_{ABS-tot}}. \tag{5.6}$$

So, the subtracted accidental number, N_{acc}, is $R \cdot T_{live} \cdot \varepsilon$.

The uncertainty of $N_{IBD,i}$ is given by

$$E^2_{IBD,i} = N_{dis-cut,i} + A^2 \times N_{ABS-tot,i} + E^2_A \times N^2_{ABS-tot,i}, \tag{5.7}$$

where E is used to represent the error of each term in Eq (5.5) with the same subscript.

The error of scale factor A, E_A, is related to the uncertainty of singles rate, R_s. Singles rate is defined in the previous chapter, which is the average value of the $N_{singles-up}$ and $N_{singles-low}$. Therefore, $N_{singles-up}$ and $N_{singles-low}$ give the intrinsic uncertainties.

There is another pairing method to count the accidental background number. We can move the first N^{th} single events to the end of this singles array, then pairing the prompt and delayed signal with the same IBD selection cuts. After pairing new accidental spectrum, the ε is calculated by Eq (5.6). The N steps random means pairing N times by moving the 1^{st}, 2^{nd}... to the N^{th} single events. The value for ε differs for different step because the singles are the random distribution.

The distance distribution of prompt and delayed signals is used to check the quality of the accidental background subtraction. As shown in Figure 5.5, the black curve is before accidental subtraction, the blue one is from the generated accidental events and the red one is after subtraction. If the subtraction process works well, the entry number should be zero between 2000 mm and 5000 mm, as shown in Figure 5.6.

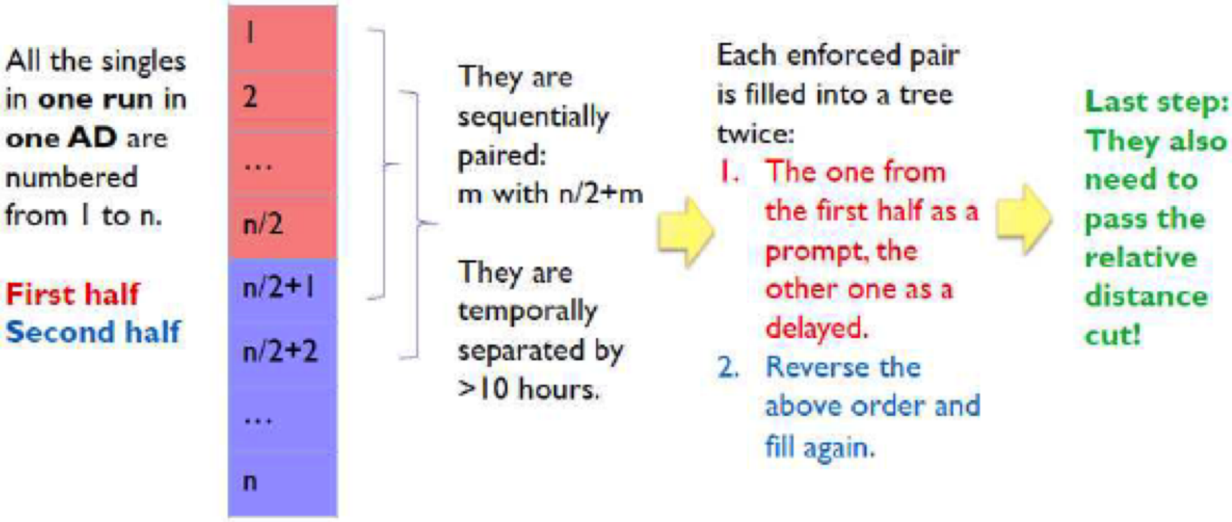

Figure 5.1: The process of generating accidental background events.

Figure 5.7 shows the delayed energy distribution for each detector. We then fit the 2.2 MeV signals with the Crystal ball function, as shown in Figure 5.8. The fitting results are summarized in the Table 5.2 and 5.9.

The Crystal Ball shape is defined by

$$f(x;\mu,\sigma,\alpha,n)=\begin{cases} exp[-\frac{(x-\mu)^2}{2\sigma^2}], & \frac{x-\mu}{\sigma}>-|\alpha| \\ (n/|\alpha|)^n exp(-\frac{\alpha^2}{2})(\frac{n}{|\alpha|}-|\alpha|-\frac{x-\mu}{\sigma}^{-n}), & \frac{x-\mu}{\sigma}\leq-|\alpha| \end{cases} \tag{5.8}$$

AD	mean ± error	sigma ± error
1	2.304021 ± 0.000413	0.138556 ± 0.000373
2	2.306428 ± 0.000417	0.139752 ± 0.000371
3	2.312265 ± 0.000418	0.137387 ± 0.000379
4	2.319766 ± 0.000516	0.137291 ± 0.000465
5	2.312939 ± 0.001500	0.139935 ± 0.001528
6	2.314307 ± 0.001503	0.136600 ± 0.001498
7	2.316229 ± 0.001545	0.141588 ± 0.001562
8	2.321682 ± 0.001928	0.144360 ± 0.002000

Table 5.2: Summary of the nH peak and sigma.

The prompt energy distributions after applying the delayed 3 σ energy cuts are shown in Figure 5.10. These are the IBD candidates. The vertex distribution of IBD candidates

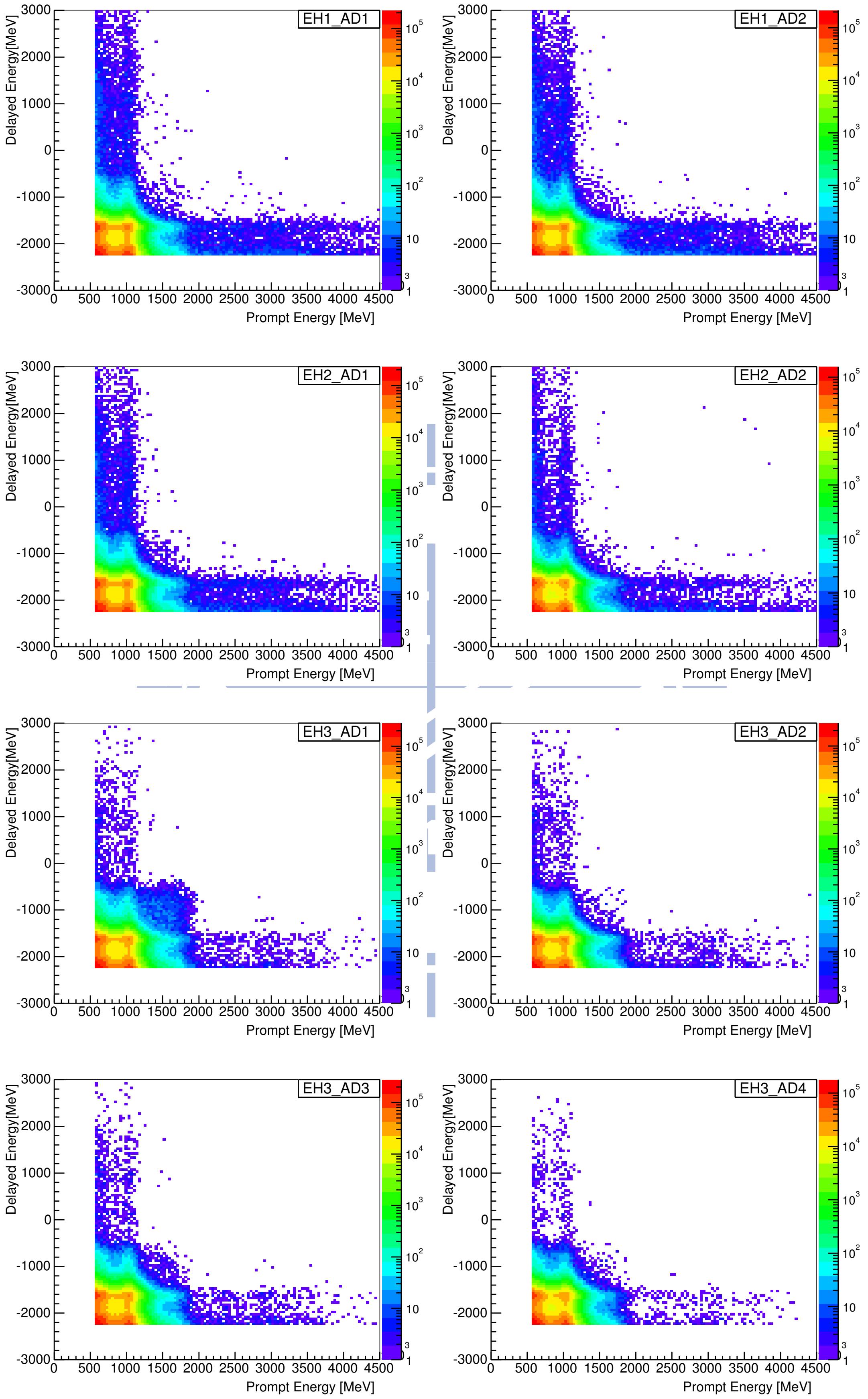

Figure 5.2: The energy distribution of the generated accidental background for each detector.

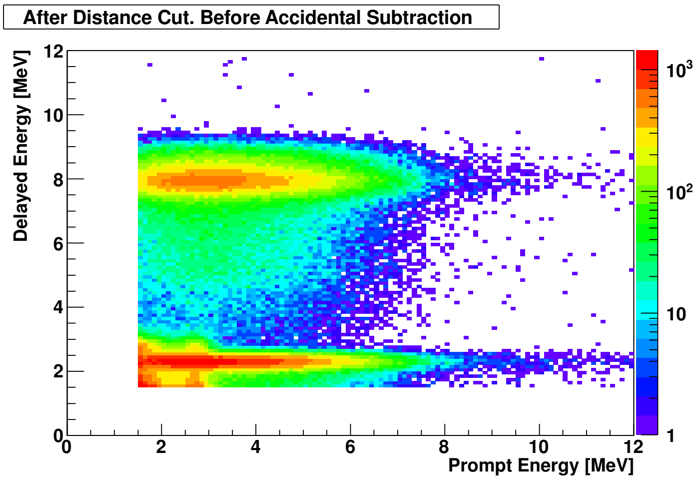

(a) Energy distribution after the distance cut

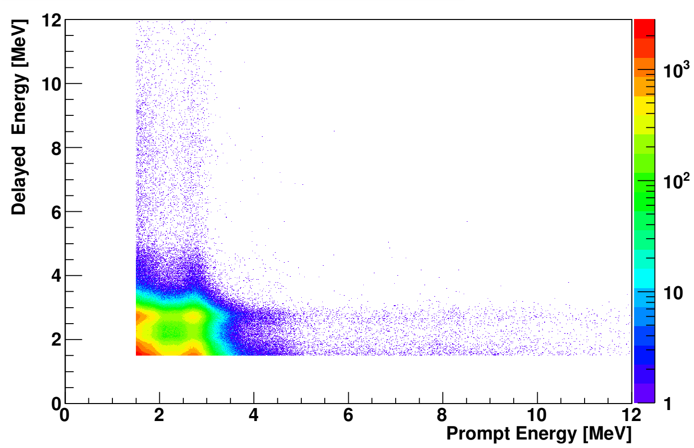

(b) Generated accidental background

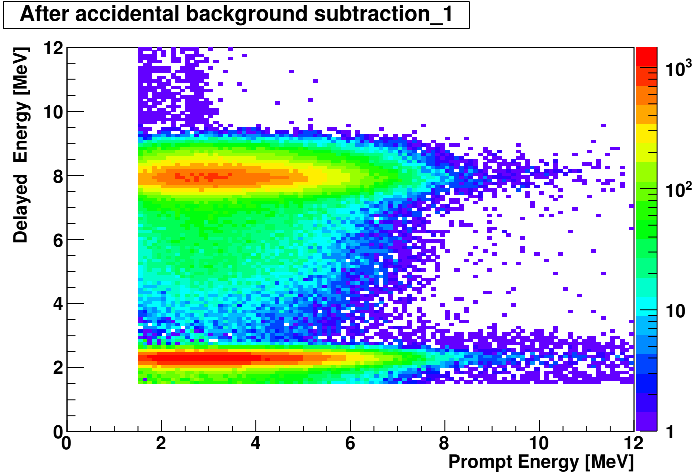

(c) Energy distribution after the background subtraction

Figure 5.3: The energy distribution for the process of accidental background subtraction: $(a) - A \cdot (b) = (c)$.

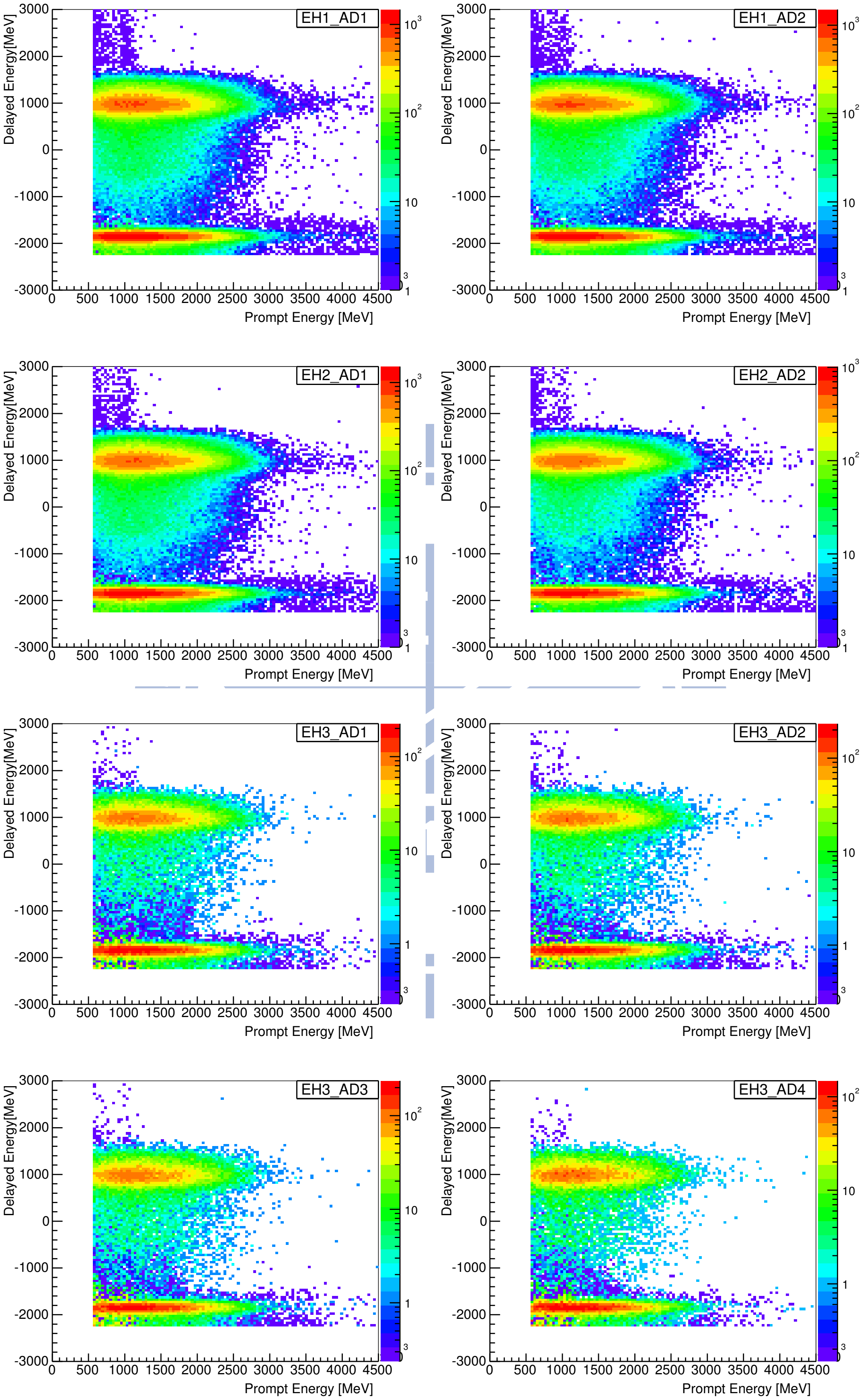

Figure 5.4: The energy distribution after the accidental subtraction for each detector.

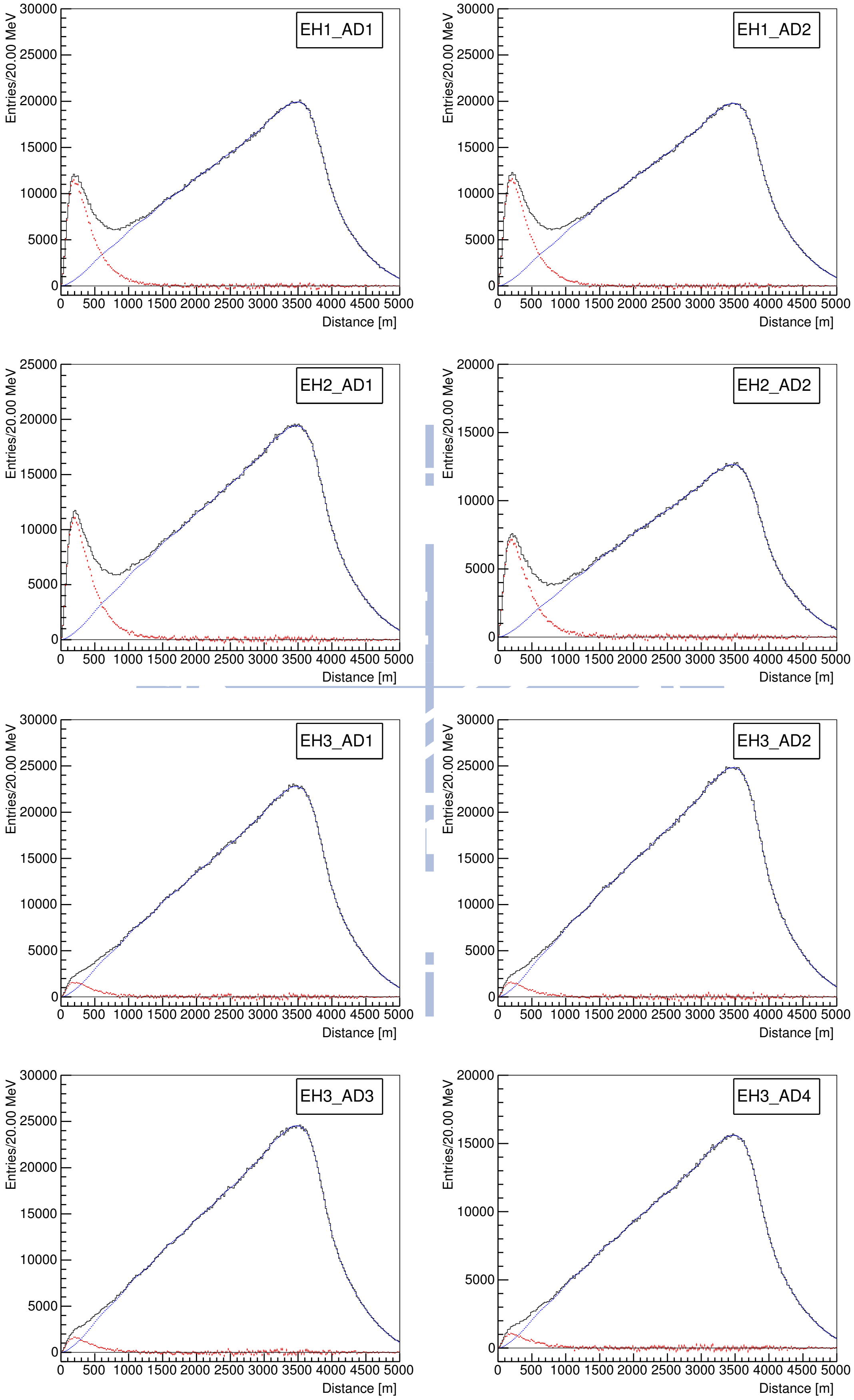

Figure 5.5: The comparison of prompt and delayed signal distributions. Black curve is before accidental subtraction. Blue curve is the generated accidental events. Red curve is after accidental subtraction.

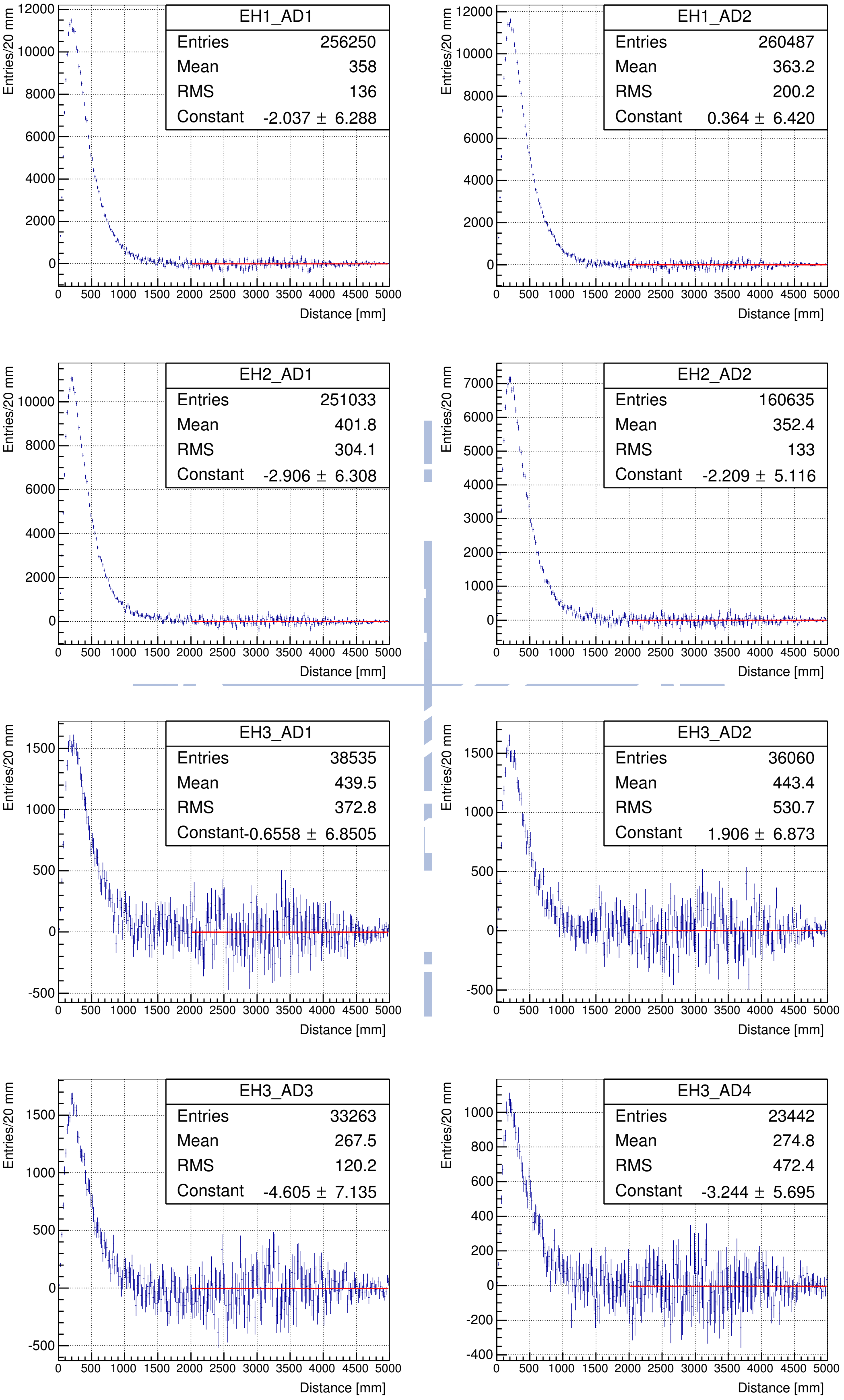

Figure 5.6: The distribution of distances between prompt and delayed signals after accidental background subtraction for each detector.

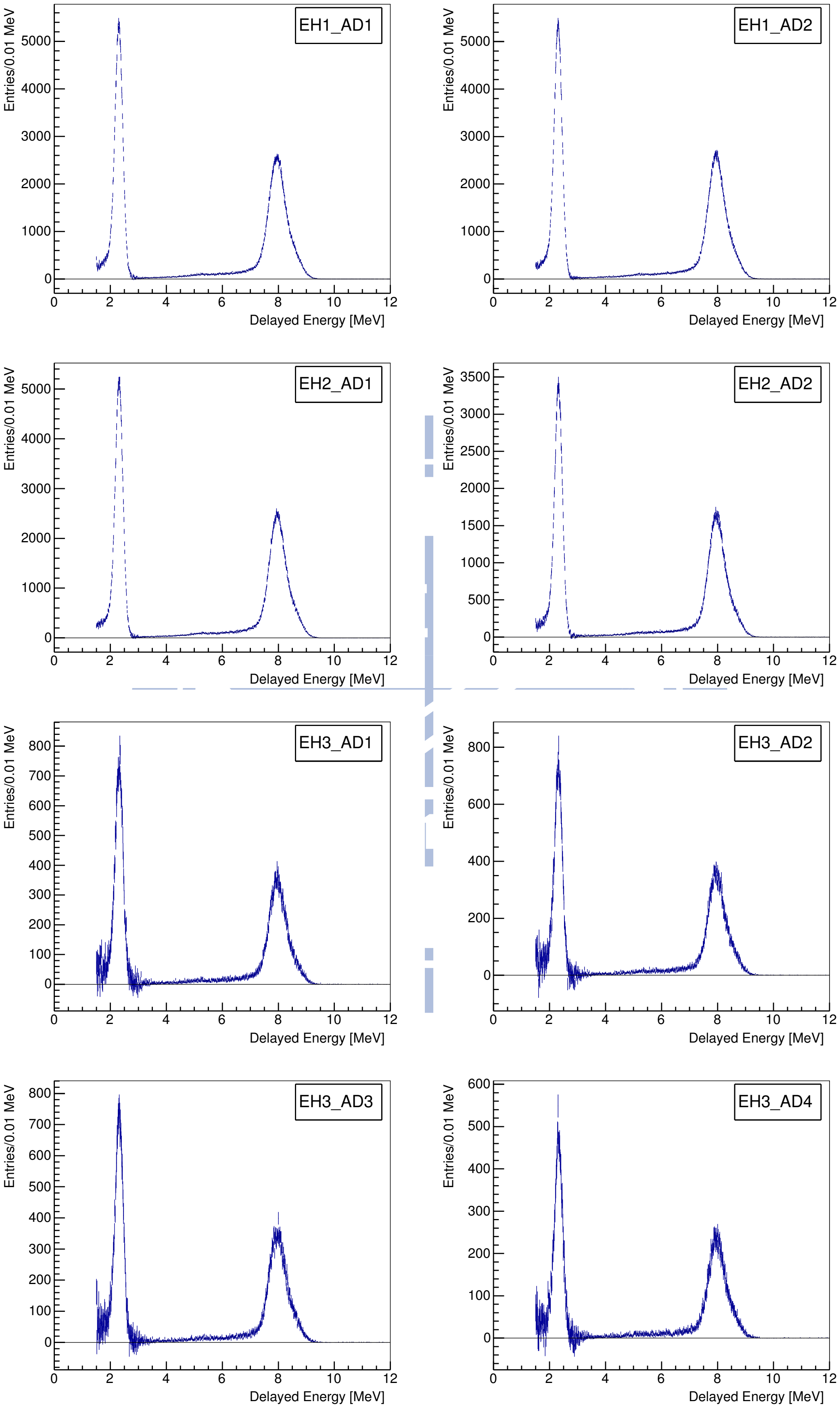

Figure 5.7: The delayed energy distribution.

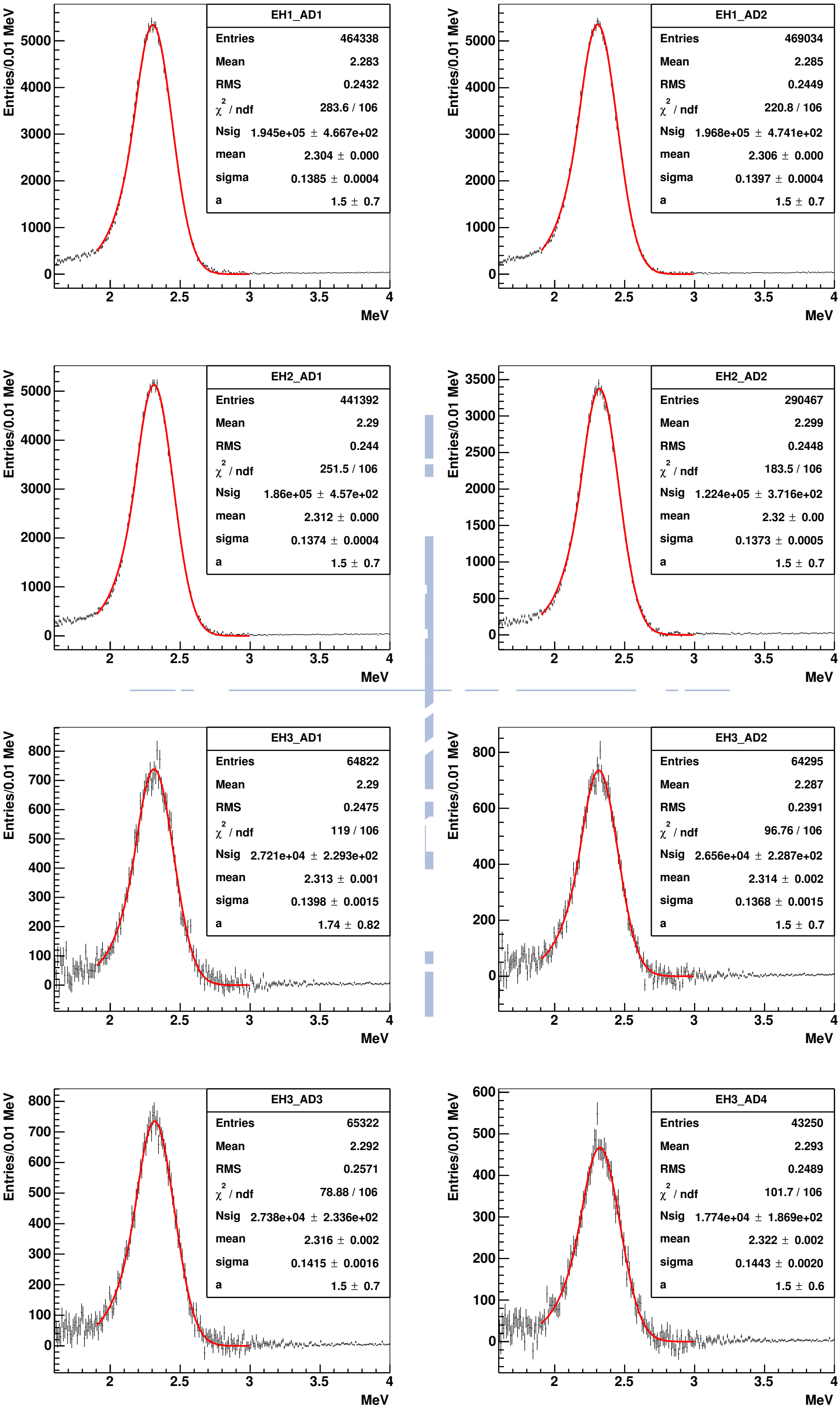

Figure 5.8: The fitting to 2.2 MeV signal with the crystal ball function.

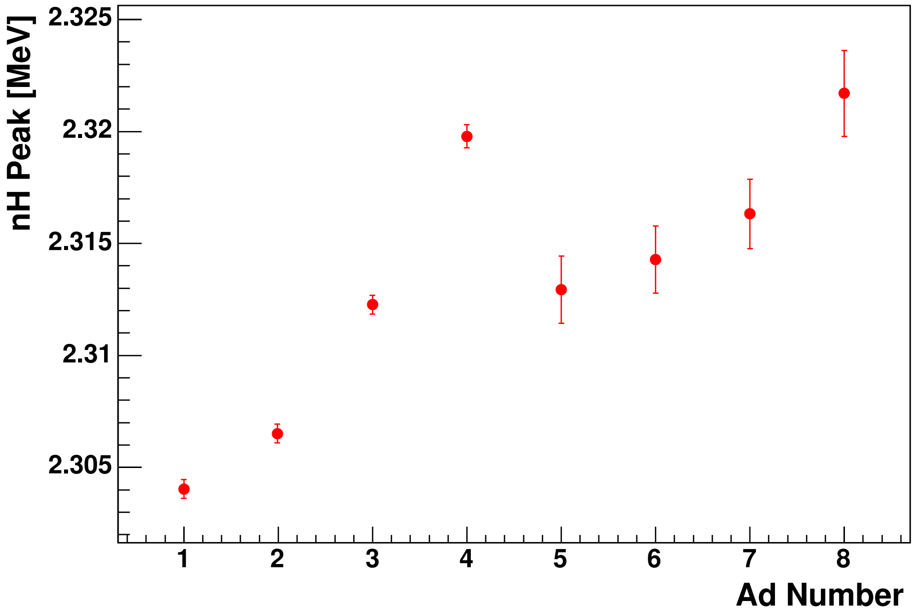

(a) nH mean for each AD

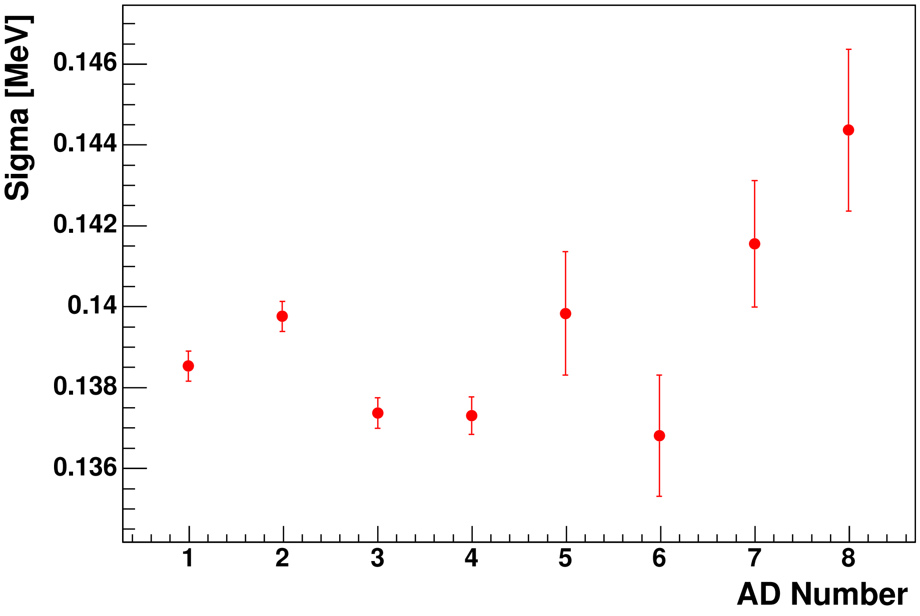

(b) Sigma for each AD

Figure 5.9: The summary of 2.2 MeV signal peaks and the associated widths.

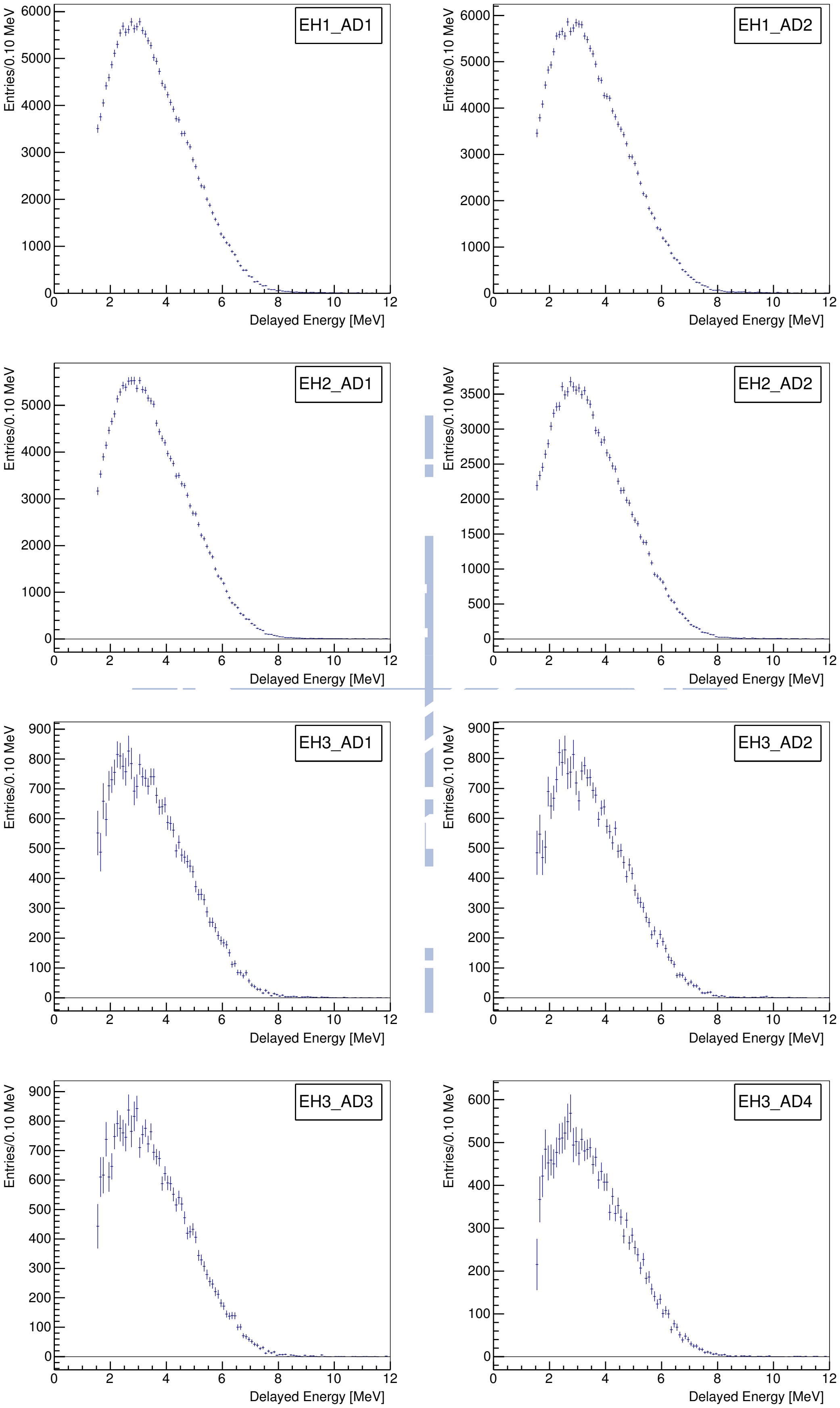

Figure 5.10: The prompt energy distributions for each AD.

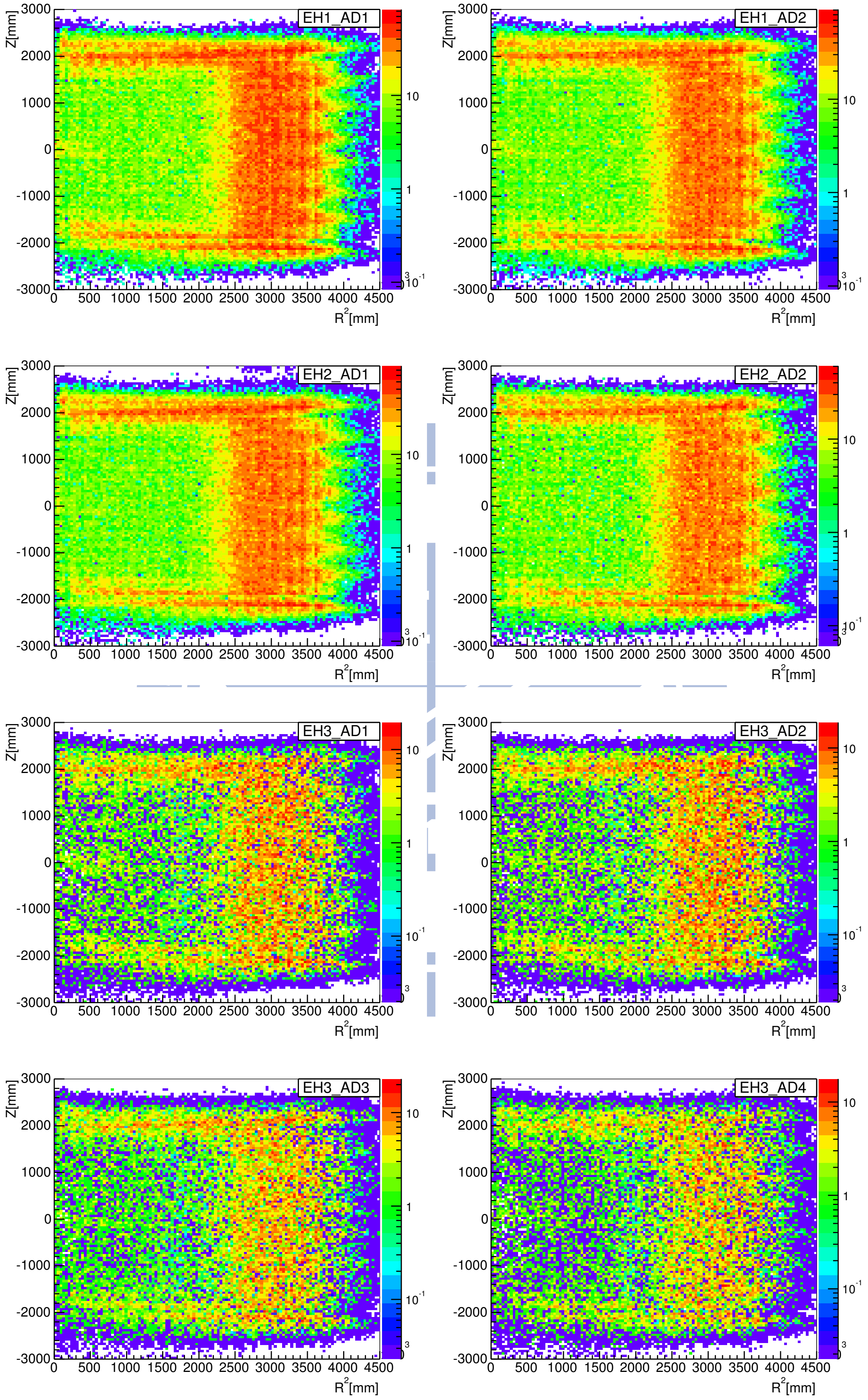

Figure 5.11: The vertex distribution of IBD candidates in each AD.

are shown in Figure 5.11.

5.2 Correlated Background

5.2.1 Fast neutron

Energetic neutrons can be produced by cosmic muons via spallation. Before neutron is thermalized, it deposits energy by the elastic scattering with proton. This process gives the prompt-like signal and the thermalized neutron captured on gadolinium or hydrogen gives the delayed signal. These prompt and delayed signals mimic IBD events.

There are timing relations between muons and the neutron produced in the detector. It is easy to remove such neutron background in the detector by the timing coincidence. Some of the neutrons which enter the detector are produced in the rock surrounding the water pool. The parent muons in such a case are tagged by the water veto system. Such neutrons are referred to as fast neutrons which do not satisfy the above timing coincidence. One can estimate the number of fast neutrons from the IBD candidates by the extrapolation method. The event selection is the same as IBD selection except that the prompt energy cut is set at 100 MeV. We then fit the prompt energy spectrum from 20 MeV to 100 MeV and then extrapolate the fitted function to lower energies. We calculate the area of the fitted function between 1.5 MeV and 12 MeV for estimating the event number of fast neutrons.

The fitting function is

$$f(E;\lambda) = \frac{N_{pow} \cdot E^{\lambda}}{\int_{1.5}^{12} E^{\lambda} \mathrm{d}E}, \tag{5.9}$$

where N_{pow} is the event number of fast neutrons, E is energy and λ is the power law constant. The fitting results are shown in Figure 5.12. The fast neutron rate can be calculated by Eq (5.1).

On the other, the first order polynomial, Eq (5.10), is used to estimate the systematic error, which is the difference between errors from N_{pow} and N_{pol1}. The total error is $\sqrt{\sigma^2_{N_{pow}} + \sigma^2_{sys}}$.

$$f(E;S) = \frac{N_{pol1} \cdot (S \cdot E + 1)}{\int_{1.5}^{12} (S \cdot E + 1) \mathrm{d}E}. \tag{5.10}$$

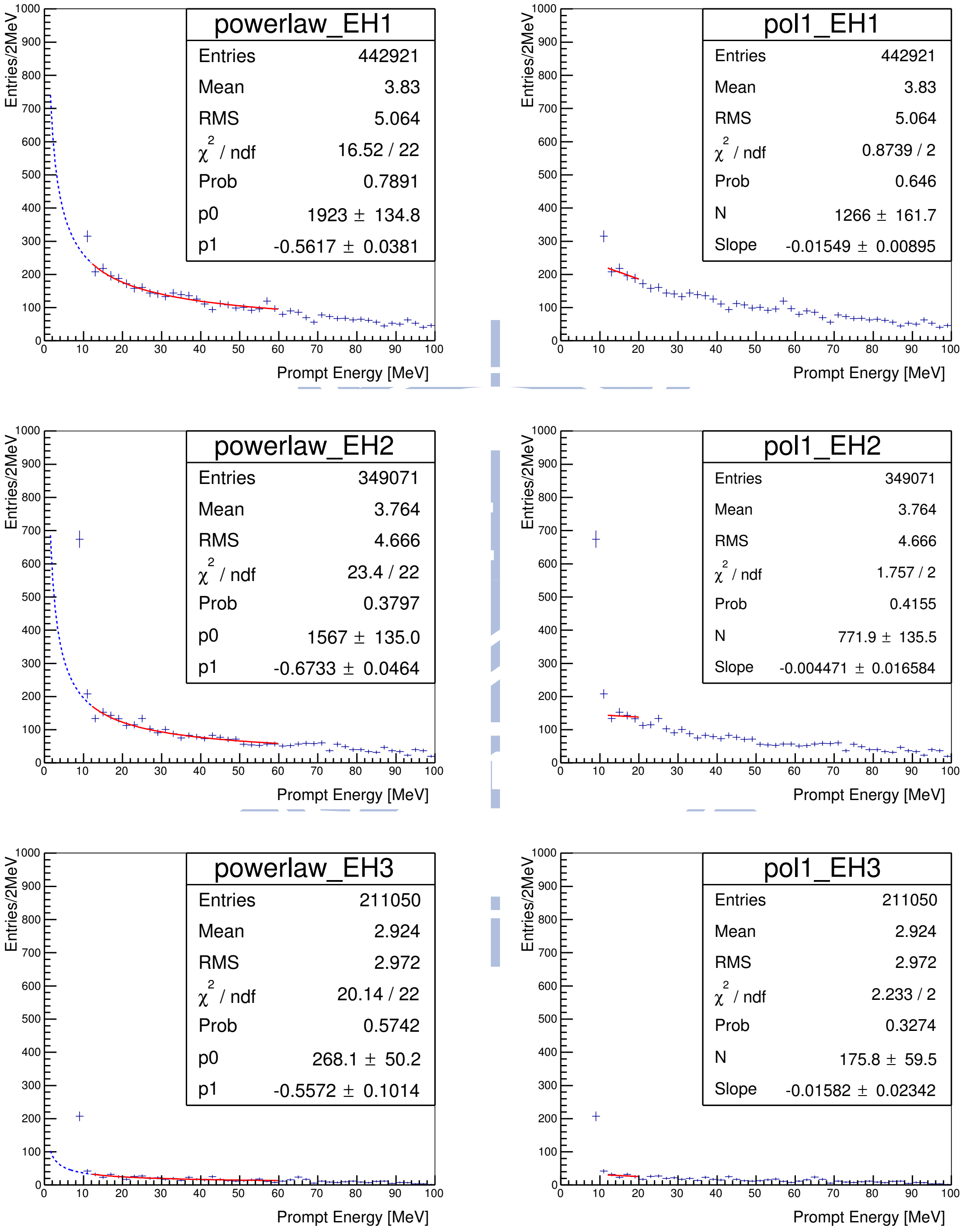

Figure 5.12: Fast neutron fitting results. The red curve is the fitting range and the blue one is the extrapolated curve.

		EH1	EH2	EH3
N_{6AD}	Eq (5.9)	601.899 ± 75.2179	226.807 ± 45.9474	83.6951 ± 29.0545
	Pol1	462.604 ± 91.0539	141.283 ± 55.5341	53.4328 ± 33.8179
λ		-0.5585 ± 0.0678	-0.5524 ± 0.1098	-0.5954 ± 0.1864
Rate		2.0193 ± 0.2579	1.4578 ± 0.3017	0.1523 ± 0.0536
N_{8AD}	Eq (5.9)	1320.95 ± 111.894	1347.98 ± 128.321	184.718 ± 41.062
	Pol1	800.702 ± 133.678	630.799 ± 123.6	122.303 ± 48.8155
λ		-0.5631 ± 0.0460	-0.6997 ± 0.0511	-0.5415 ± 0.1205
Rate		2.2571 ± 0.1948	2.1706 ± 0.2068	0.1282 ± 0.0290
N_{6+8}	Eq (5.9)	1922.84 ± 134.805	1567.15 ± 134.961	268.149 ± 50.1711
	Pol1	1265.72 ± 161.749	771.855 ± 135.455	175.806 ± 59.4557
λ		-0.5617 ± 0.0381	-0.6733 ± 0.0464	-0.5572 ± 0.1014
Rate		2.1768 ± 0.1556	2.0179 ± 0.1738	0.1348 ± 0.0256

Table 5.3: Summary of the fast neutron number and rate estimation

5.2.1.1 Verification of the fast neutron spectrum shape

Eq (5.9) can be verified by the fast neutron spectrum, shown in Figure 5.14. The fast neutron events are selected from muons tagged only by outer water pool (OWP) with the following additional requirements:

- There is no any IWS or AD muon events 10 μs before an OWS muon;
- There is no any IWS or AD muon between the OWS muon and the AD signal in a time window.

The muon types are classified as follows:

- Both OWP and IWP Muon: the number of PMT hit is greater than 20.
- AD muon: the total visible energy deposit is more than 100 MeV in an AD
- Shower muon: the total visible energy deposit is more than 2.5 GeV in an AD

The selection criteria of fast neutron events are as follows:

- The same as IBD selection except the prompt energy cut which is set at 100 MeV.
- The AD re-trigger cut: time to previous AD muon greater than 12 μs.
- Double muon cut: A muon passing through the detector can induce one or more neutrons. These neutrons can be captured by Gd or H, as shown in Figure 5.13(b). The double muon events are shown when the time interval is greater than 0.6 μs.

To remove these, it requires that the prompt signal to previous OWS muon is less than 0.6 μs.

- Stop muon cut: The low energy muon which enters into the detector and decays there is called "stop muon". Figure 5.13(c) is the delayed events versus the delayed time to previous OWS tagged muon. There are a lot of events with energy larger than 20 MeV and extending to 60 MeV when the time interval is less than 10 μs. These are mainly from the stop muon events. To remove these events, one requires that the delayed signal to previous OWS muon is greater than 10 μs.

5.2.2 $^{8}He/^{9}Li$

In addition to neutrons, cosmic muons also produce radioactive isotopes via their interactions with nuclei in the liquid scintillatior. It is worth noting that the long-lived radioisotopes, $^{9}Li(\tau_{1/2} = 178.3ms, Q = 13.6MeV)$ and $^{8}He(\tau_{1/2} = 118.5ms, Q = 10.7MeV)$, can give correlated beta-neutron signals and fake IBD events.

The time distribution of ^{9}Li decays can be described by an exponential function

$$f_0(t) = \lambda_{Li} \mathrm{e}^{-\lambda_{Li} t}, \tag{5.11}$$

where t is the time to the last muon which produces ^{9}Li, and $\lambda_{Li} = (1/257.2) \cdot ms^{-1}$ is the decay constant.

The probability density function (p.d.f) of ^{9}Li decays after a muon that produces this ^{9}Li is given by

$$f_1(t) = \lambda_{Li} \mathrm{e}^{-\lambda_{Li} t} \cdot \mathrm{e}^{-\lambda_\mu t}, \tag{5.12}$$

where t is time to the last muon and $\mathrm{e}^{-\lambda_\mu t}$ is the probability for not having additional muons between the last muon and time t.

If the ^{9}Li event is not from the previous muon, but from the muon which is earlier than the previous muon with the time between these two muons as t_1, the p.d.f of ^{9}Li decays is given by

$$f_2(t) = \int_0^\infty \lambda_\mu \, \mathrm{d}t_1 \cdot \lambda_{Li} \mathrm{e}^{-\lambda_{Li}(t+t_1)} \cdot \mathrm{e}^{-\lambda_\mu t} = \lambda_\mu \times \lambda_{Li}/(\lambda_\mu + \lambda_{Li}) \mathrm{e}^{-(\lambda_{Li}+\lambda_\mu)t} \tag{5.13}$$

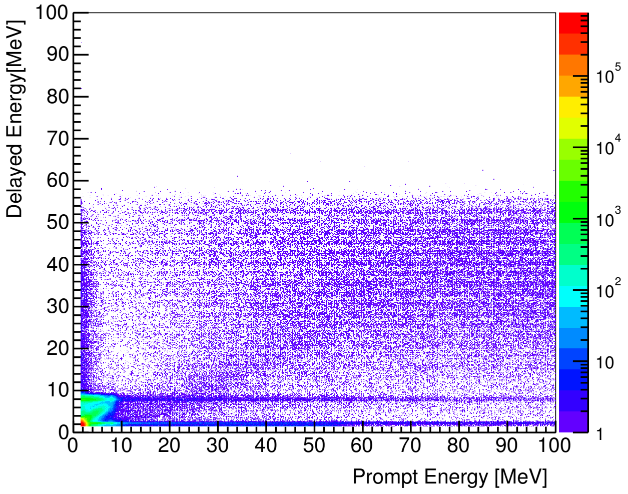

(a) Energy distribution for OWS tagged muon induced events.

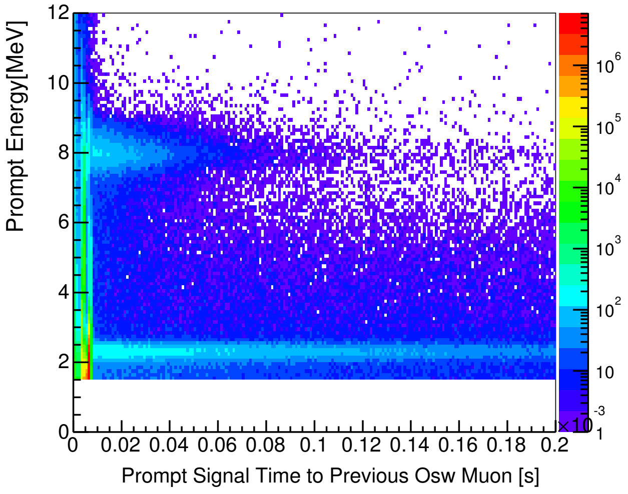

(b) Prompt events versus the prompt time to previous OWS tagged muon

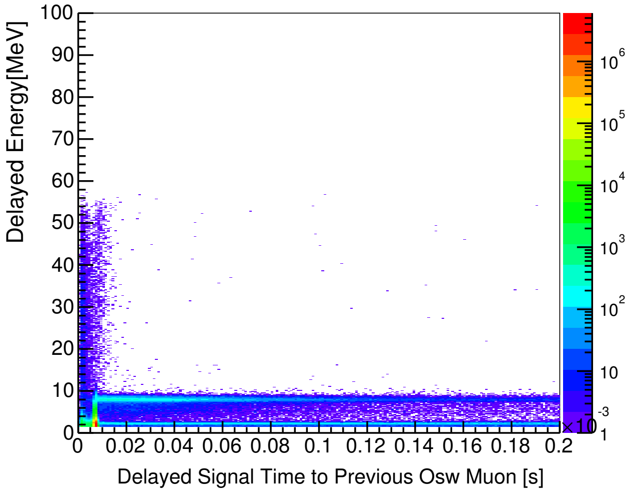

(c) Delayed events versus the prompt time to previous OWS tagged muon

Figure 5.13: OSW tagged muon induced neutrons.

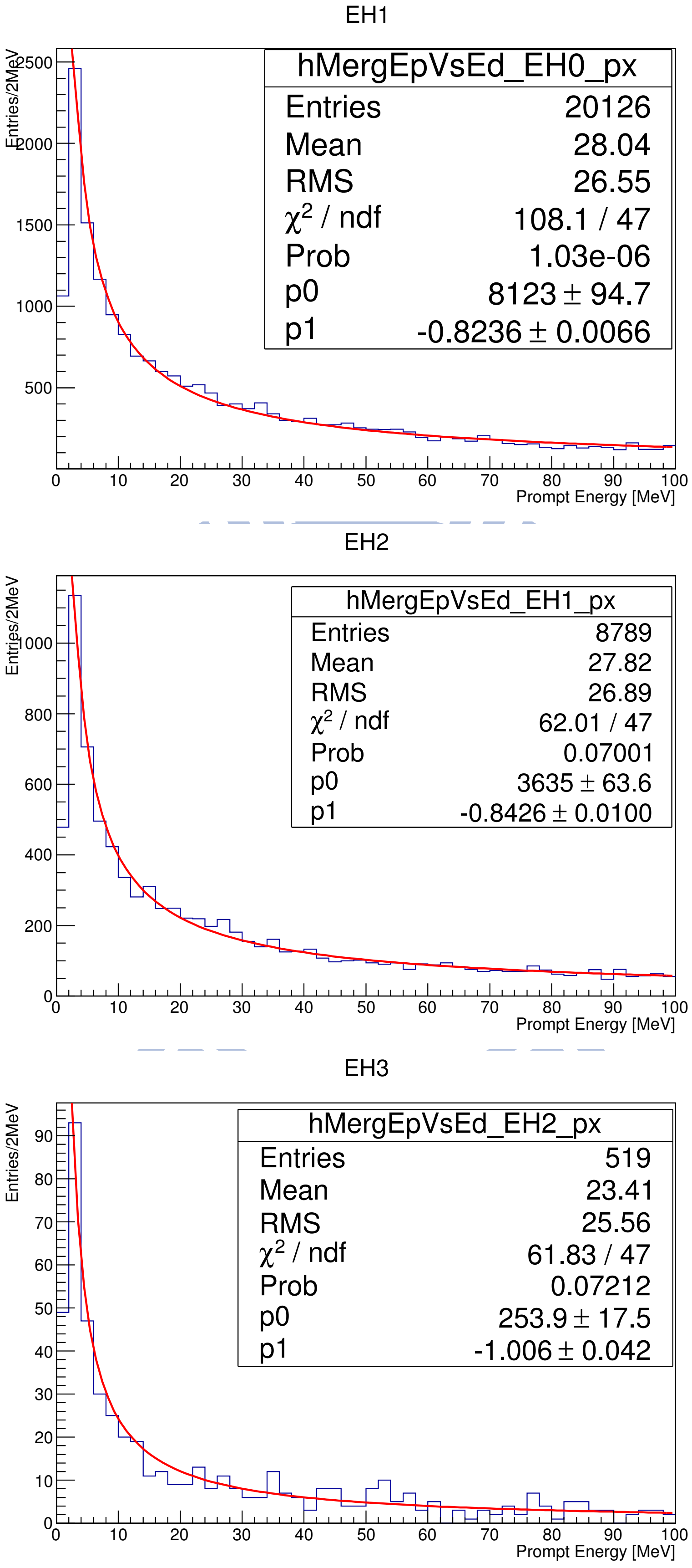

Figure 5.14: Fittings to fast neutrons from muons tagged only by outer water pool (OWP).

Obviously, ^9Li can be produced by even earlier muons. Hence one should sum over an infinite series of pdf. It can be shown that

$$f_{Li}(t) \equiv f_1(t) + f_2(t) + f_3(t) + ... = (\lambda_{Li} + \lambda_\mu)\mathrm{e}^{-(\lambda_{Li}+\lambda_\mu)t}. \tag{5.14}$$

On the another hand, for the IBD and accidental events, the p.d.f of such events is given by

$$f_{IBD+Acc}(t) = \lambda_\mu \cdot \mathrm{e}^{-\lambda_\mu t}, \tag{5.15}$$

where t is the time to the last muon.

At time t, the number of ^9Li, IBD and accidental events can then be written as

$$N_{event}(t) = N_{Li}(\lambda_{Li} + \lambda_\mu) \cdot \mathrm{e}^{-(\lambda_{Li}+\lambda_\mu)t} + N_{IBD+Acc}\lambda_\mu \cdot \mathrm{e}^{-\lambda_\mu t}. \tag{5.16}$$

To estimate the number of ^9Li events, we vary t and fit the event counts for different t using Eq (5.16), shown in Figure 5.15. The ^9Li events are selected by the tagged muon which requires at least one trigger with energy larger than 1.8 MeV within the 20 μs and 200 μs after an AD muon.

5.2.3 $^{241}Am -^{13}C$ source

As mentioned in the previous chapter, the calibration sources are stored in the ACUs on the top of each detector. The neutron source, $^{241}Am -^{13}C$, emits neutrons which inelastically scatter with steel and then captured by nuclei, such as Fe, Cr, Mn or Ni. This process emits many gammas and mimics IBD events. From the Figure 5.16, which shows the z distribution of the neutron-like signal, the asymmetric feature can be used to estimate the background rate from $^{241}Am -^{13}C$ source.

Figure 5.17 shows the neutron-like spectrum within the 6 and 12 MeV. The spectrum difference (red) between the top half (blue) and the bottom half (green) of the detector is the contribution from the AmC source. The correlated AmC background can be estimated by

$$Bkgs(normal) = F(strong\ AmC) \cdot N_{n-like}, \tag{5.17}$$

where N_{n-like} is the number of subtracted results within the 6 MeV to 12 MeV, $F(strong\ AmC) =$

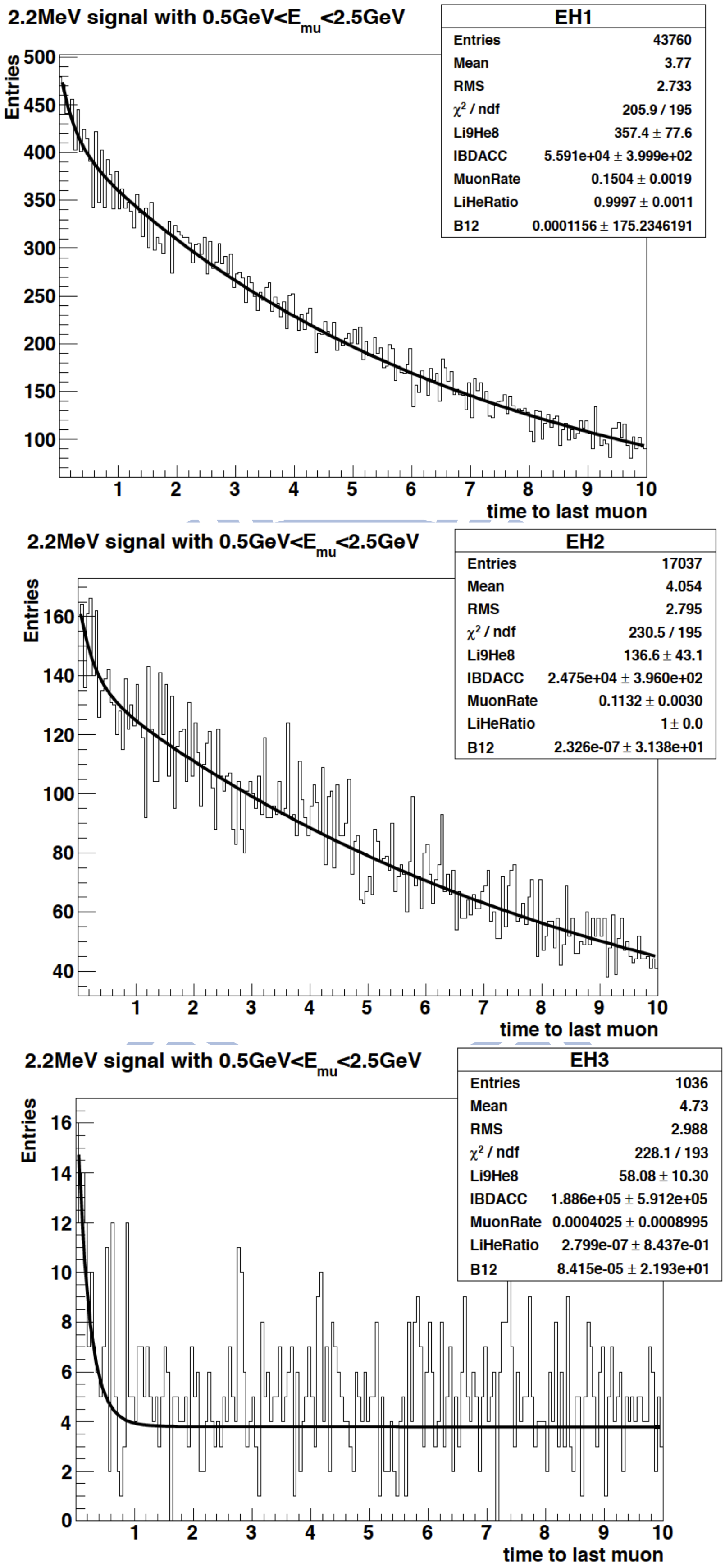

Figure 5.15: ^{9}Li fitting results for each experimental hall.

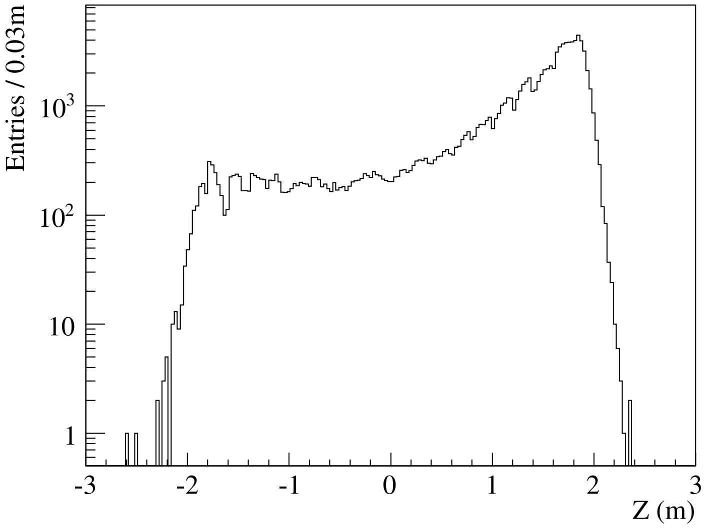

Figure 5.16: The distribution of the neutron-like signals on the Z direction from the normal physics run. The center of the detector is at $Z = 0$ m [27].

3.36854×10^{-4} is the scaling factor which is from the strong AmC source study. The study of strong AmC source has been done by our collaborator.

Table 5.5 is the summary of the background rates for each detector.

	AD1	AD2	AD3	AD4	AD5	AD6	AD7	AD8
N_{6AD}	37156 ± 351.377	35184 ± 348.525	40280 ± 326		35810 ± 211.367	34150 ± 208.355	33792 ± 205.811	
R_{6AD}	0.0838	0.0797	0.0872		0.0658	0.0628	0.0622	
N_{8AD}	55327 ± 473.406	58837 ± 477.706	53318 ± 431.771	62554 ± 440.831	18704 ± 185.844	14265 ± 174.118	13592 ± 172.945	23372 ± 199.244
R_{8AD}	0.0636	0.0679	0.0578	0.0679	0.0175	0.0133	0.0127	0.0219
N_{6+8}	92483 ± 589.558	94021 ± 591.332	93598 ± 541.019	62554 ± 440.831	54514 ± 281.45	48415 ±271.531	47384 ± 268.827	23372 ±199.244
R_{6+8}	0.0704	0.0718	0.0676	0.0679	0.0338	0.0300	0.0294	0.0219

Table 5.4: The summary of the $^{241}Am -^{13}C$ background number and rates for each AD and data taking period.

5.3 Summary

Table 5.5 is the summary of the background rates for each detector.

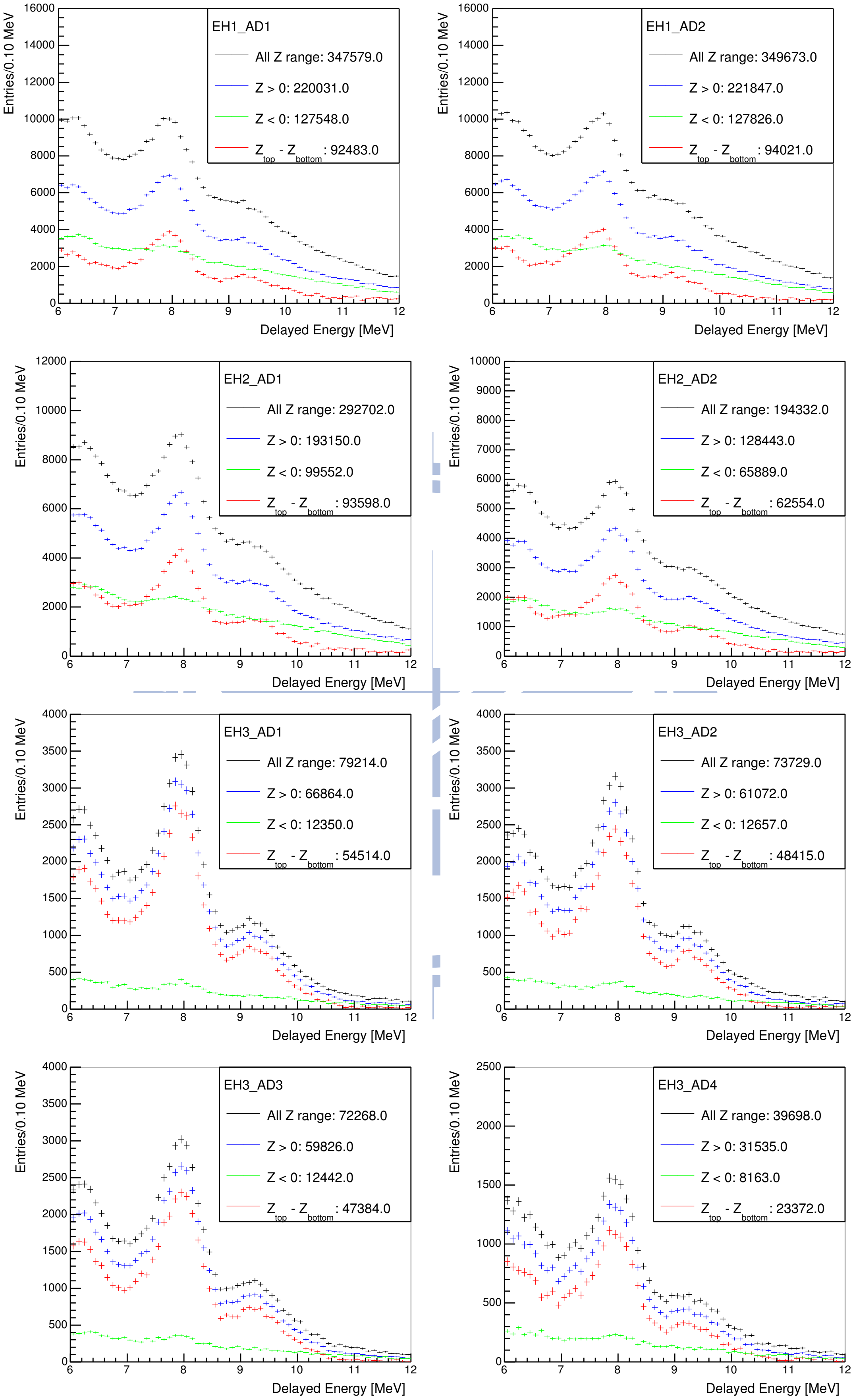

Figure 5.17: The spectrum of neutron-like signals with different selections on Z-position. The black points are total signals without position cuts. The blue points are from the top half of detector, $Z > 0$ m; the greens are from the bottom half of detector, $Z < 0$ m. The points in red are the difference between the blue and green spectra.

Rate	Data Set	AD1	AD2	AD3	AD4	AD5	AD6	AD7	AD8
$R_{Acc.}$	6AD	64.96 ± 0.13	64.06 ± 0.13	57.62 ± 0.11	-	62.10 ± 0.06	64.05 ± 0.06	68.20 ± 0.07	-
	8AD	58.91 ± 0.11	58.07 ± 0.11	54.06 ± 0.09	52.71 ± 0.09	52.64 ± 0.04	52.83 ± 0.04	56.73 ± 0.05	56.74 ± 0.05
R_{FastN}	6AD	2.09 ± 0.27	2.09 ± 0.27	1.37 ± 0.29	-	0.10 ± 0.04	0.10 ± 0.04	0.10 ± 0.04	-
	8AD	2.18 ± 0.76	2.18 ± 0.76	2.02 ± 1.03	2.02 ± 1.03	0.14 ± 0.06	0.14 ± 0.06	0.14 ± 0.06	0.14 ± 0.06
$R_{^9Li}$	6AD	5.81 ± 1.39	5.81 ± 1.39	3.57 ± 1.13	-	0.54 ± 0.12	0.54 ± 0.12	0.54 ± 0.12	-
	8AD	1.70 ± 0.73	1.70 ± 0.73	1.46 ± 0.72	1.46 ± 0.72	0.15 ± 0.05	0.15 ± 0.05	0.15 ± 0.05	0.15 ± 0.05
R_{AmC} (1/d)	6AD	0.09 ± 0.03	0.09 ± 0.03	0.09 ± 0.03	-	0.06 ± 0.02	0.06 ± 0.02	0.06 ± 0.02	-
	8AD	0.08 ± 0.04	0.08 ± 0.04	0.07 ± 0.04	0.08 ± 0.04	0.02 ± 0.01	0.02 ± 0.01	0.01 ± 0.01	0.02 ± 0.01

Table 5.5: The summary of the background rates. Data set: '6AD' is from Dec 24, 2011 to Jul 28, 2012. '8AD' is from Oct 19, 2012 to Nov 30, 2013.

Chapter 6

Efficiency Study

The total number of the detected delayed coincident events, N_{det}, is

$$N_{det} = \phi \cdot \sigma \cdot \varepsilon_{\mu} \cdot \varepsilon_{m} \cdot \left[\sum_{v}^{3m,4m,Acry.} N_{p,v} \cdot f_{v} \cdot \varepsilon_{ep,v} \cdot \varepsilon_{ed,v} \cdot \varepsilon_{t,v} \right] \cdot \varepsilon_{d} \tag{6.1}$$

where ϕ is neutrino flux; σ is cross section; ε_{μ} is muon veto efficiency; ε_{m} is multiplicity cut efficiency; ε_{d} is the distance cut efficiency; $N_{p,v}$ is the number of protons; f is the hydrogen capture fraction; ε_{ep} is the prompt energy cut efficiency; ε_{ed} is the delayed energy cut efficiency and ε_{et} is the timing cut efficiency.

6.1 Muon veto efficiency

The muon veto efficiency is calculated by Eq (4.3). The full time is the time interval between DAQ start time and DAQ stop time. Figure 4.5 shows the muon veto efficiency for each ADs from Dec 24, 2011 to Nov 30, 2013. It was very stable. Those value are summarized in Table 4.3.

6.2 Multiplicity cut efficiency

The multiplicity cut efficiency can be precisely calculated using singles' rate and muon rate as follows [32]:

$$\begin{aligned}\varepsilon_m = \Bigg\{ & \frac{R_\mu}{R_s + R_\mu}[1 - e^{-(R_s+R_\mu)T_c}] + e^{-(R_s+R_\mu)T_c} \\ & + \frac{R_s}{R_s + R_\mu} e^{-R_\mu T_c}[1 - e^{-(R_s+R_\mu)T_c}] - \frac{R_s}{2R_s + R_\mu} e^{-R_\mu T_c}[1 - e^{-(2R_s+R_\mu)T_c}] \Bigg\} \\ & \times e^{-R_s T_c},\end{aligned} \tag{6.2}$$

where R_μ is the effective muon rate, R_s is the singles' rate and T_c is the coincident windows. The multiplicity cut efficiency for each run is calculated and shown in Figure 6.1.

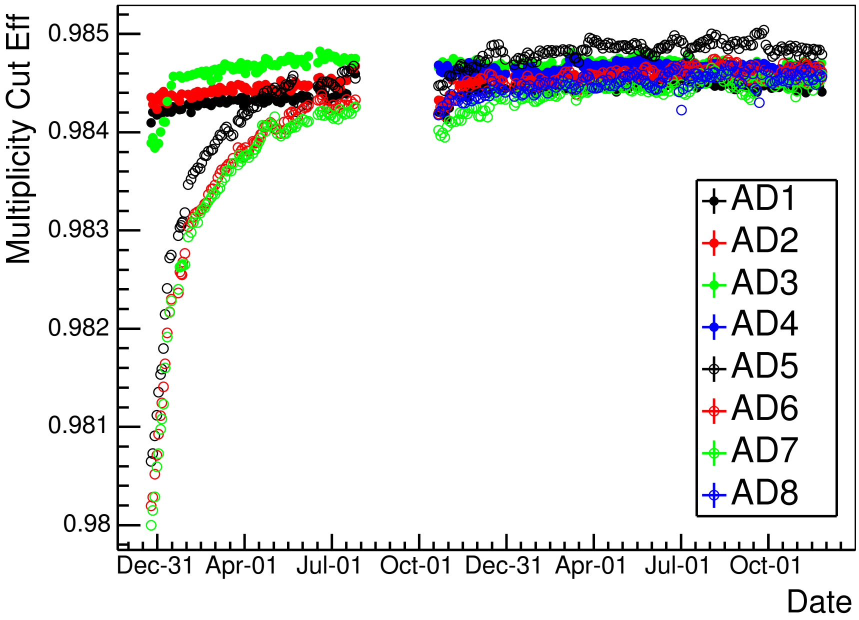

Figure 6.1: Multiplicity cut efficiency per day from Dec. 24, 2011 to Nov. 30, 2013.

6.3 Energy cut efficiency

The energy cut efficiency is divided into two parts, the prompt energy cut and the delayed energy cut. Both prompt and delayed energy cut efficiencies, ε_{ep} and ε_{ed}, are obtained by simulations.

The Monte-Carlo process is based on the Daya Bay official package, *NuWa*. The energy cut efficiencies for prompt and delay signals are defined by

$$\varepsilon_p = \frac{N(nH\ capture; E_p > 1.5MeV)}{N(total\ nH\ capture)} \tag{6.3}$$

$$\varepsilon_d = \frac{N(E_d\ in\ 3\sigma\ range; E_p > 1.5MeV)}{N(nH\ capture; E_p > 1.5MeV)} \tag{6.4}$$

Correlated uncertainty For nH capture peak, there are slight differences between LS region, Gd-LS region and MC. Both prompt and delayed energies from Monte-Carlo are scaled to the data for calculating the efficiencies. Then, the difference between the data and Monte-Caro gives correlated uncertainties. The results are shown in Table 6.1.

	$\frac{N_{nH-cap}}{N_{total}}$	ε_p	ε_d
GdLS	0.1563	0.9646	0.9677
LS	0.9582	0.9442	0.6776
After energy rescaling			
GdLS	0.1563	0.9518	0.9695
LS	0.9582	0.9297	0.6799

Table 6.1: The results on energy cut efficiencies.

Uncorrelated uncertainty The relative difference on nH/nGd ratios[1]between AD1 and AD2 are taken as the uncorrelated uncertainty. The average nH/nGd is about one which indicates that the spallation neutrons mainly come from outside of the AD. They have more chances to be captured in the LS region. This is the region where the energy leakage and energy resolution effects are more significant to the 3σ energy cut efficiency. For normal IBD neutrons induced by reactor neutrinos, they are more uniformly distributed in the AD. Hence it is believed that the difference observed in nH/nGd for different ADs in spallation neutron sample is more severe than IBD neutrons. Therefore, 0.5% is a conservative estimation of the uncertainty in 3σ delayed energy cut efficiency. Since this uncertainty comes from the measurement of spallation neutrons which enter into the entire detection volume, we assign 0.5% as the uncertainty of energy cut efficiency in both LS and GdLS regions. The final result is shown in Table 6.7.

---

[1] nH/nGd ratio: the ratio of the nH signal and nGd signal. nH: The number of the nH signal range within the 3 σ region from the peak. nGd: The number of the nGd signal within 6 MeV and 12 MeV.

6.3.1 nH to nGd ratio by spallation neutron

Assuming the same muon flux for the ADs in the same experimental hall and the same Gd target mass, nGd is a good anchoring point for confirming the identicalness of n-H selection with a floating 3 sigma energy cut. To have a solid measurement of the identicalness of energy cut efficiency, the nH to nGd ratio is used.

Spallation neutron events selection

Muon identification is different from IBD event selection, which requires that the PMT hit number for IWS or OWS is larger than 20, the charge sum in each AD (QSumAD) is larger than 50 MeV. For shower muon, the energy deposits in an AD should be larger than 2.5 GeV. The event selection window is 2500 μs. In the event selection window, the first part is the signals window, which is between 20 μs and 700 μs. The other part is the background window, which is between 700 μs and $\sim$ 1400 μs. One can get the spallation neutron spectrum by background subtraction.

Fitting methods

In this study, the fitting function consists of two parts, signal and background, as defined in Eq. (6.5). The functions are normalized in the fitting range. The signal plus background is given by

$$\frac{N_1 \cdot f_{sig}}{\int_{E_-}^{E_+} f_{sig}} + \frac{N_2 \cdot f_{bkg}}{\int_{E_-}^{E_+} f_{bkg}}, \tag{6.5}$$

where N_1 is number of signal, N_2 is number of background, f_{sig} is the signal shape function, f_{bkg} is the background shape function, E_+ and E_- are upper and lower limits of the fitting range.

For n-H capture, f_{sig} is the Crystal Ball shape function,

$$f_{sig} = f(x;\mu,\sigma,\alpha,n) = \begin{cases} \exp\left(-\frac{(x-\mu)^2}{2\sigma^2}\right), & \frac{x-\mu}{\sigma} > -|\alpha| \\ (n/|\alpha|)^n \exp(-\frac{\alpha^2}{2})(\frac{n}{|\alpha|} - |\alpha| - \frac{x-\mu}{\sigma}^{-n}). & \frac{x-\mu}{\sigma} \leq -|\alpha| \end{cases} \tag{6.6}$$

Since this function is composed of a Gaussian and a power low, the parameters, μ, σ, α, n, are defined as usual.

The background shape functions are exponential function, Eq. (6.7), and second order polynomial function, Eq. (6.8).

$$f_{bkg} = \exp(p_1 \cdot x). \tag{6.7}$$

$$f_{bkg} = a_1 x^2 + b_1 x + 1. \tag{6.8}$$

For n-Gd capture, there are two kinds of gadolinium isotopes, ^{155}Gd and ^{157}Gd, which capture neutron in ADs. The shape can be described by two crystal ball functions, Eq. (6.9), known as double crystal ball function.

$$\begin{aligned} f_{dCB}(x;\mu,\sigma,\alpha,n) &= N_{^{157}Gd} \cdot f_{CB1}(x;\mu_1,\sigma_1,\alpha_1,n_1) + N_{^{155}Gd} \cdot f_{CB2}(x;\mu_2,\sigma_2,\alpha_2,n_2) \\ &= N_{^{157}Gd} \cdot f_{CB1}(x;\mu_1,\sigma_1,\alpha_1,n_1) + N_{^{157}Gd} \cdot C_N \cdot f_{CB2}(x;\mu_2,\sigma_2,\alpha_2,n_2) \\ &= N \cdot [f_{CB1}(x;\mu_1,\sigma_1,\alpha_1,n_1) + C_N \cdot f_{CB2}(x;\mu_2,\sigma_2,\alpha_2,n_2)]. \end{aligned} \tag{6.9}$$

Hence, the signal shape function becomes

$$f_{sig} = f_{CB1}(x;\mu_1,\sigma_1,\alpha_1,n_1) + C_N \cdot f_{CB2}(x;\mu_2,\sigma_2,\alpha_2,n_2) \tag{6.10}$$

To simplify the fitting function, the relative abundance, neutron capture cross-sections and binding energies of the capture products (or gamma energies) for these isotopes are considered, which were shown in Table 6.2. The relations between parameters are

- The peak position μ: $\mu_1 = \mu \cdot 7.94 \cdot S$, $\mu_2 = \mu \cdot 8.54 \cdot S$, where $S = \dfrac{60900 \cdot 0.1480 + 254000 \cdot 0.1565}{60900 \cdot 0.1480 \cdot 8.54 + 254000 \cdot 0.1565 \cdot 7.94}$
- Resolution: $\sigma_1 = \sigma_2 \cdot C_\sigma$, where $C_\sigma = \sqrt{8.54/7.94}$
- $\alpha = \alpha_1 = \alpha_2$ and $n = n_1 = n_2$.
- $C_N = \dfrac{60900 \cdot 0.1480}{254000 \cdot 0.1565}$

The background shape function for the nGd case is the first order polynomial function,

$$f_{bkg} = p_1 \cdot x + 1. \tag{6.11}$$

isotope	abundance	$\sigma(n_{th}, \gamma)$	E_γ
^{155}Gd	14.80 %	60,900 b	8.5364 MeV
^{157}Gd	15.65 %	254,000 b	7.9374 MeV

Table 6.2: Gadolinium isotopes abundance, capture cross-section and energies [33].

The fitting range for nH capture is from 0.8 MeV to 3.5 MeV; for nGd is from 6.0 MeV to 12.0 MeV. The fitting results are shown in Figs. 6.2, 6.3 and 6.4. The neutron capture peak and sigma are summarized in the Tables 6.3, 6.4 and Figure 6.5.

AD number	nH Mean (exp) +/- err	nH Mean (pol2) +/- err	nGd Mean +/- err
1	2.3081 ± 0.0003	2.3090 ± 0.0003	8.0926 ± 0.0004
2	2.3111 ± 0.0003	2.3121 ± 0.0003	8.0909 ± 0.0004
3	2.3170 ± 0.0003	2.3177 ± 0.0003	8.1027 ± 0.0004
4	2.3253 ± 0.0003	2.3260 ± 0.0004	8.1034 ± 0.0005
5	2.3260 ± 0.0007	2.3273 ± 0.0008	8.1232 ± 0.0011
6	2.3273 ± 0.0008	2.3287 ± 0.0008	8.1208 ± 0.0011
7	2.3301 ± 0.0008	2.3315 ± 0.0008	8.1244 ± 0.0011
8	2.3346 ± 0.0010	2.3359 ± 0.0010	8.1253 ± 0.0014

Table 6.3: Summary of neutron capture peak.

AD number	nH Sigma (exp) +/- err	nH Sigma (pol2) +/- err	nGd Sigma +/- err
1	0.1440 ± 0.0003	0.1432 ± 0.0003	0.2958 ± 0.0004
2	0.1451 ± 0.0003	0.1441 ± 0.0003	0.2967 ± 0.0004
3	0.1424 ± 0.0003	0.1418 ± 0.0004	0.2927 ± 0.0004
4	0.1422 ± 0.0004	0.1414 ± 0.0004	0.2928 ± 0.0005
5	0.1443 ± 0.0008	0.1429 ± 0.0010	0.2991 ± 0.0012
6	0.1444 ± 0.0009	0.1425 ± 0.0009	0.3026 ± 0.0012
7	0.1476 ± 0.0008	0.1459 ± 0.0010	0.3048 ± 0.0012
8	0.1504 ± 0.0011	0.1476 ± 0.0012	0.3070 ± 0.0015

Table 6.4: Summary of neutron capture sigma.

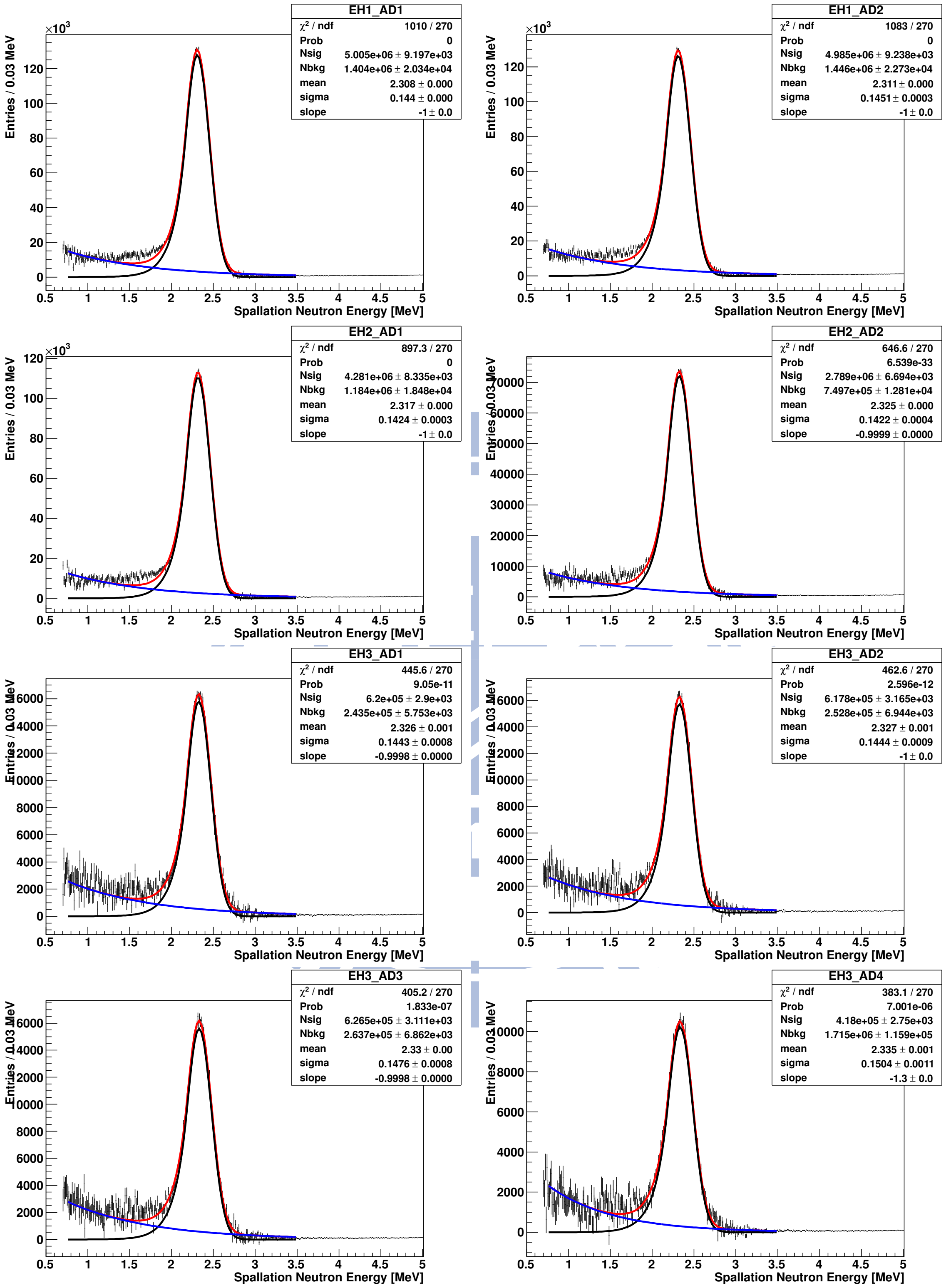

Figure 6.2: The energy peak of spallation neutrons captured by hydrogen. Signal time window: 20 ∼ 700 μs, n-H capture peak fitted with crystal ball and exponential background functions for 8 ADs.

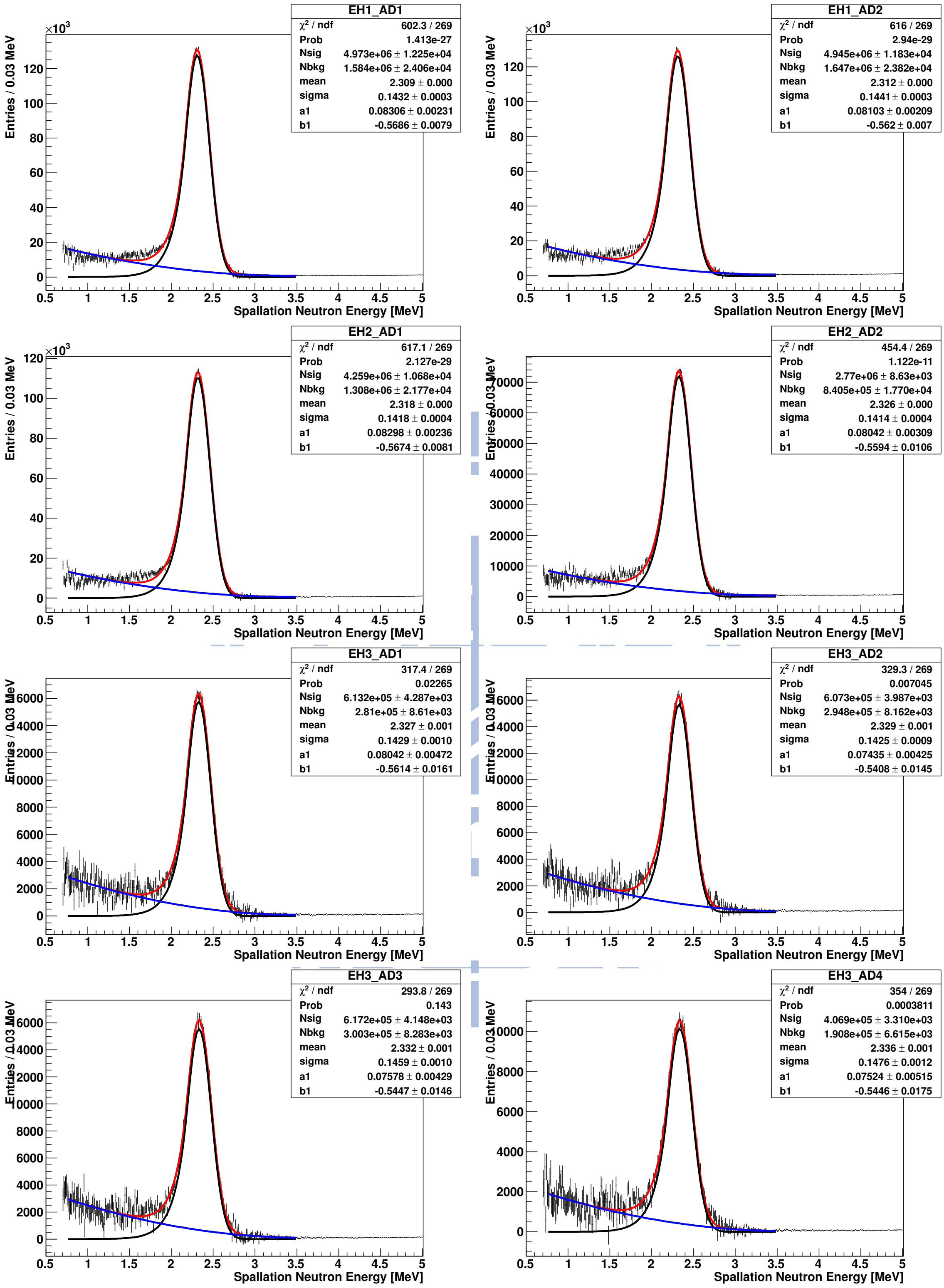

Figure 6.3: The energy peak of spallation neutrons captured by hydrogen. Signal time window: 20 ∼ 700 μs, n-H capture peak with crystal ball and second-order polynomial background functions for 8 ADs.

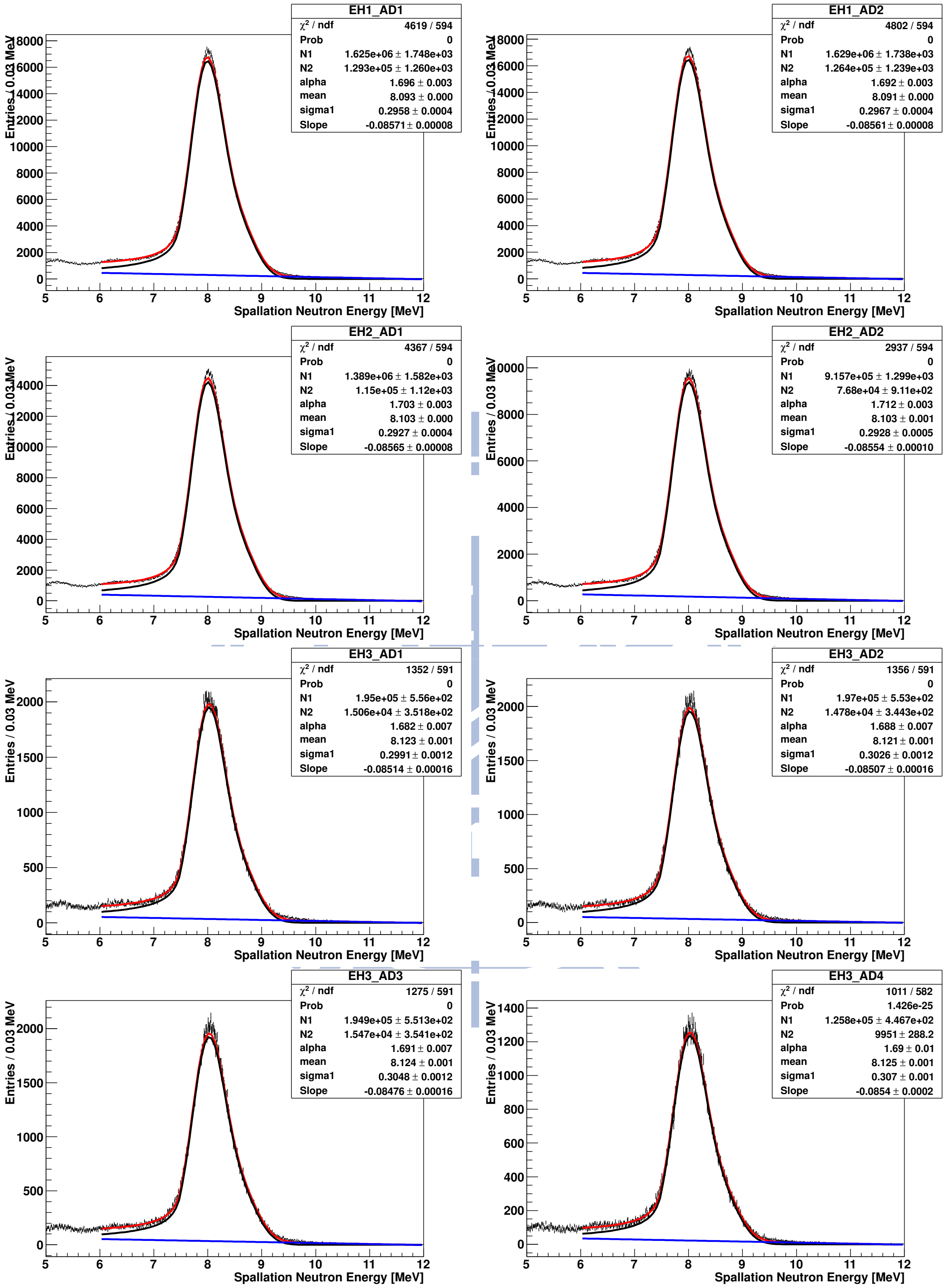

Figure 6.4: The energy peak of spallation neutron captured by gadolinium. Signal time window: 20 ∼ 700 μs, n-Gd capture peak fitted with double crystal ball and 1st-order polynomial background functions for 8 ADs.

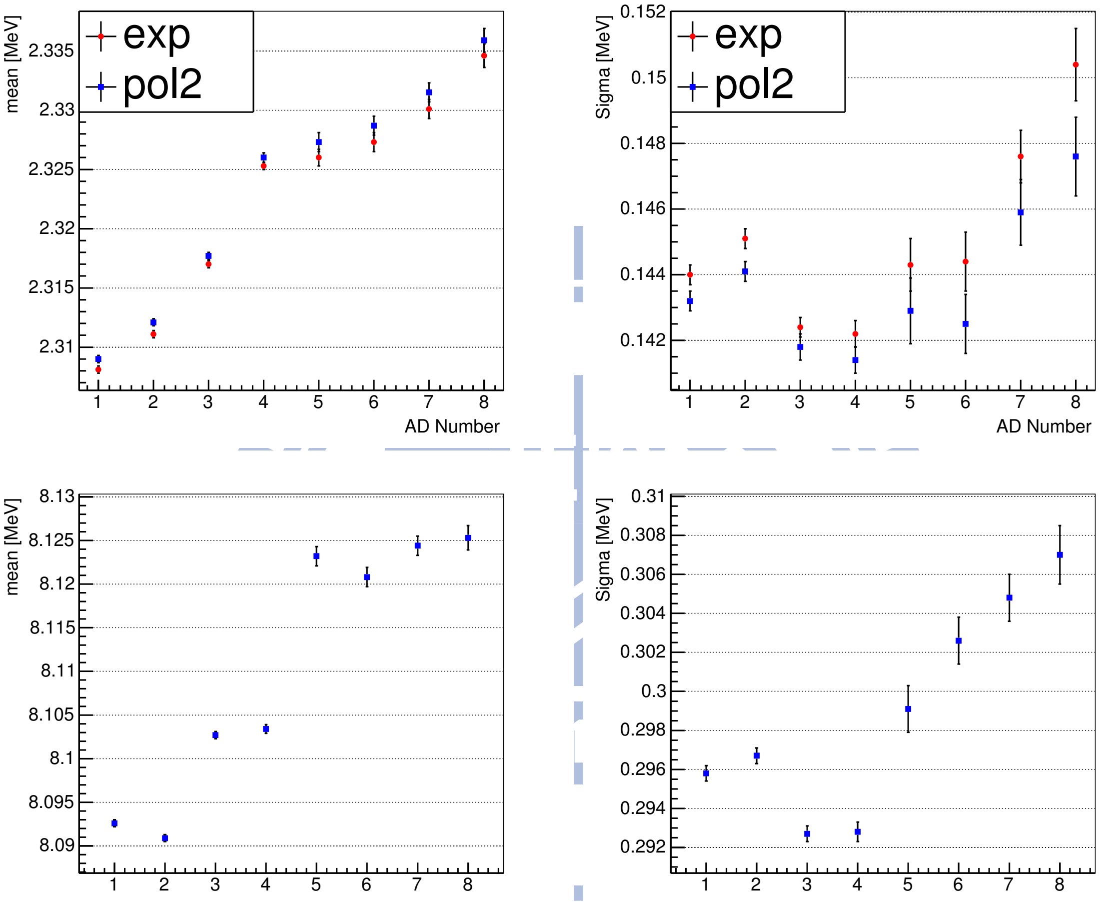

Figure 6.5: Signal time window: $20 \sim 700\ \mu s$. The left column shows the mean of the energy peak while the left column shows the width of the peak. The top panel shows the fitting to the energy peak of nH capture events with background modeled by exponential function and second-order polynomial function, respectively. The bottom panel shows the fitting to the energy peak of nGd capture events with background modeled by first-order polynomial function.

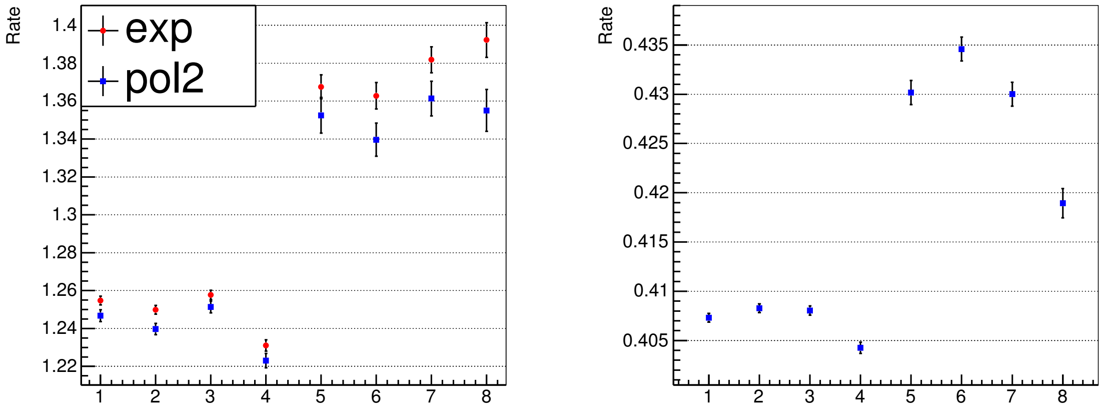

Figure 6.6: Signal time window: 20 $\sim$ 700 μs. The nH (left) and nGd (right) capture rates in different ADs.

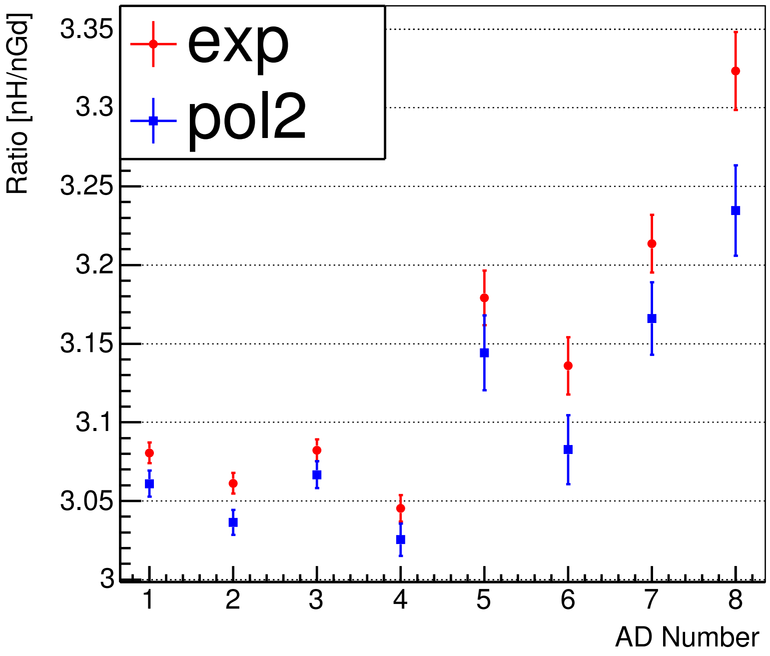

Figure 6.7: The nH to nGd ratio. Signal time window: 20 $\sim$ 700 μs.

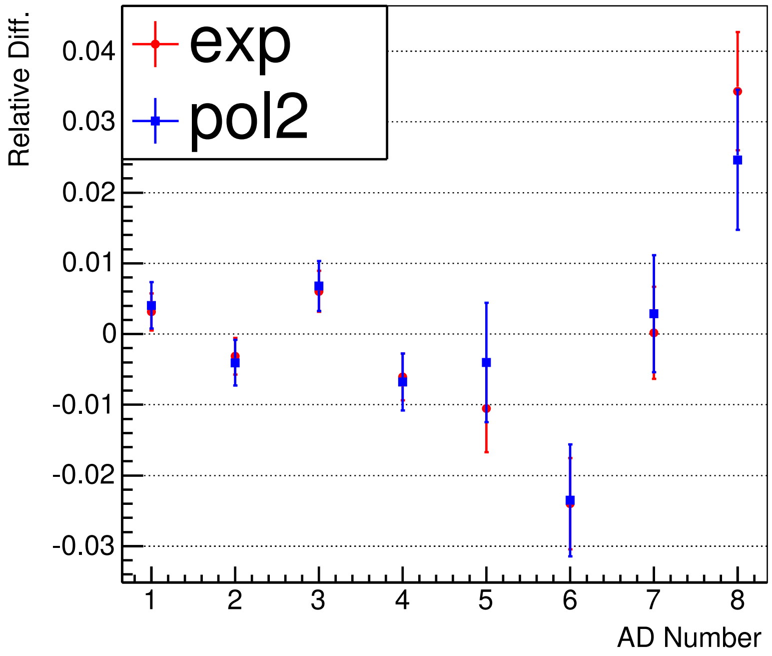

Figure 6.8: Relative difference of nH to nGd ratio between site average value and each AD for different models of background function.

Spallation Neutron Rate

We can calculate spallation neutron rate by

$$\text{Rate} = \frac{\text{Number of Signal}}{\text{Live Time}}, \tag{6.12}$$

where the live time is defined by

$$\text{LiveTime} = \text{Signal time Window} \cdot \text{Number of Net Muon}. \tag{6.13}$$

The Net Muon is defined at Figure 4.4(b). The spallation neutron rate are summarized in the Table 6.5 and Figure 6.6.

Spallation Neutron Ratio

The spallation neutron nH to nGd ratio is defined by

$$R = \frac{N_{nH}}{N_{nGd}} \tag{6.14}$$

The nH to nGd ratios are summarized in Table 6.6 and Figure 6.7. Figure 6.8 shows the relative difference between AD1 and AD2 for each time window. The relative difference is defined by

$$\text{Relative Difference} = \frac{AD_i - AD_{avg}}{AD_{avg}}. \tag{6.15}$$

AD number	nH Rate (exp) +/- err	nH Rate (pol2) +/- err	nGd Rate +/- err
1	1.2547 ± 0.0023	1.2468 ± 0.0031	0.4073 ± 0.0004
2	1.2498 ± 0.0023	1.2397 ± 0.0030	0.4083 ± 0.0004
3	1.2577 ± 0.0024	1.2514 ± 0.0031	0.4080 ± 0.0005
4	1.2311 ± 0.0030	1.2230 ± 0.0038	0.4043 ± 0.0006
5	1.3676 ± 0.0063	1.3525 ± 0.0095	0.4302 ± 0.0012
6	1.3628 ± 0.0070	1.3397 ± 0.0088	0.4346 ± 0.0012
7	1.3818 ± 0.0069	1.3614 ± 0.0091	0.4300 ± 0.0012
8	1.3923 ± 0.0091	1.3551 ± 0.0110	0.4189 ± 0.0015

Table 6.5: Summary of spallation neutron rate[Hz].

AD number	Ratio (exp) +/- err	Ratio(pol) +/- err
1	3.0805 ± 0.0066	3.0610 ± 0.0082
2	3.0612 ± 0.0065	3.0363 ± 0.0080
3	3.0823 ± 0.0070	3.0667 ± 0.0084
4	3.0452 ± 0.0085	3.0254 ± 0.0104
5	3.1792 ± 0.0173	3.1442 ± 0.0237
6	3.1359 ± 0.0183	3.0826 ± 0.0220
7	3.2135 ± 0.0184	3.1660 ± 0.0231
8	3.3234 ± 0.0248	3.2346 ± 0.0287

Table 6.6: Summary of the ratio $R \equiv N_{nH}/N_{nGd}$.

The relative difference 0.005 will be used for calculating the uncorrelated uncertainty of ADs. The energy cut efficiencies are shown in Table 6.7.

	ε_p	ε_d
GdLS	0.9518 ± 0.0128(cor.) ± 0.0048 (unc.)	0.9695 ± 0.0018(cor.) ± 0.0048 (unc.)
LS	0.9297 ± 0.0145(cor.) ± 0.0046 (unc.)	0.6799 ± 0.0023(cor.) ± 0.0034 (unc.)

Table 6.7: The energy cut efficiencies and their uncertainties.

6.3.2 Understanding the energy cut and energy leakage

To understand the physics of energy leakage and find out the dominant physics mechanisms, we first look into the relation between neutron captured position and its energy.

From the neutron captured by hydrogen vertex, the captured points are near the acrylic edge for the low energy neutrons (<0.5 MeV). If the energy leakage is related to the neutron capture position as implied by the above low energy region, the detector geometry is important to the energy cut. However, from the Monte Carlo results, we attribute the energy leakage mechanism to the outward-emitted gammas. Moreover, the gamma path length is not the main reason for the energy leakage. Figure 6.9 depicts the detector. The green dot is the neutron capture point. The green arrow is neutron position vector on radial direction, e.g. $(r_x, r_y, 0)$, and the red one is the gamma direction vector, e.g. (g_x, g_y, g_z). ϕ is the angle between these two vectors. l is the path length of gamma. To determine the gamma direction, we calculate $\cos\phi$, which is defined by

$$\cos\phi = \frac{(r_x, r_y, 0)\cdot(g_x, g_y, g_z)}{\sqrt{r_x^2 + r_y^2}\cdot\sqrt{g_x^2 + g_y^2 + g_z^2}}, \tag{6.16}$$

where r_x and r_y are the components of the neutron position vector, g_x, g_y and g_z are the components of the gamma direction vector.

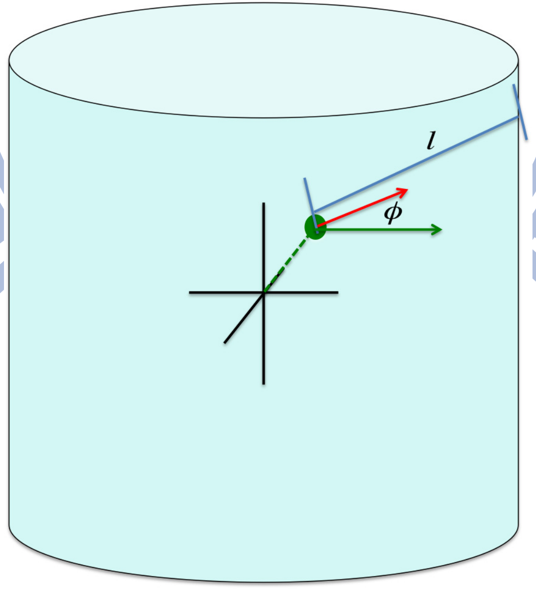

Figure 6.9: The green dot is the neutron capture point. The green arrow is neutron position vector and the red one is the gamma direction vector. ϕ is the angle between these two vectors. l is the path length of gamma.

The relation between neutron energy and the gamma path length is shown in Figure 6.10, while the relation between neutron energy and $\cos\phi$ is shown in Figure 6.11. For lower energy, the possible path length is shorter than 400 mm and gamma is emitted outward ($\cos\phi \sim 1$). In other words, the energy leakage depend both on the gamma path length and the gamma emission direction. These results indicate that the energy leakage is more correlated to the gamma emission direction than the neutron capture position. This feature occurs for each detector.

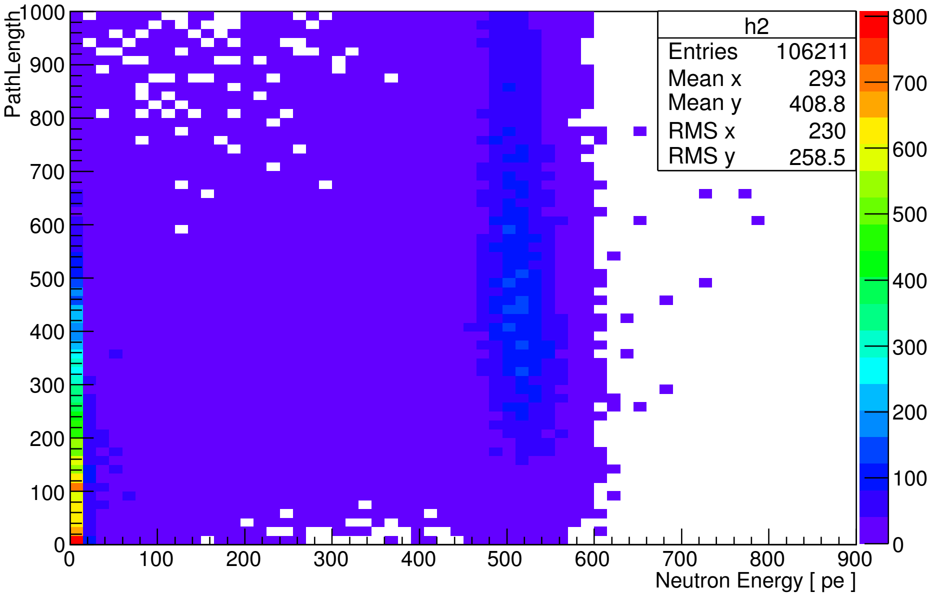

Figure 6.10: The relation between neutron energy and the gamma path length.

Furthermore, from the Monte Carlo simulation results of varying the detector geometry, density and optical properties, the efficiency of the 3 σ cut around the 2.2 MeV nH capture peak stays almost the same. This means that the energy cut efficiency is not sensitive to the above physics quantities. Therefore, for the uncorrelated systematic error of nH delayed-signal energy cut, the geometry effect can be ignored.

To determine the prompt energy cut efficiency (ε_{ep}), the leakage and the energy scale with resolution effects are considered. About 99% of positrons lose their kinetic energies by depositing their energies to the medium first and annihilate with electrons at rest. So, the average positron range is much shorter than the 2.2 MeV gamma. After the IBD selection cuts, most selected events are away from the 4 m vessel edge. Figure 6.12 is the leakage fraction of LS IBD events after delayed energy cut from Monte-Carlo simulations. It shows that the leakage fraction is 1%. Therefore, for the prompt signal, the difference

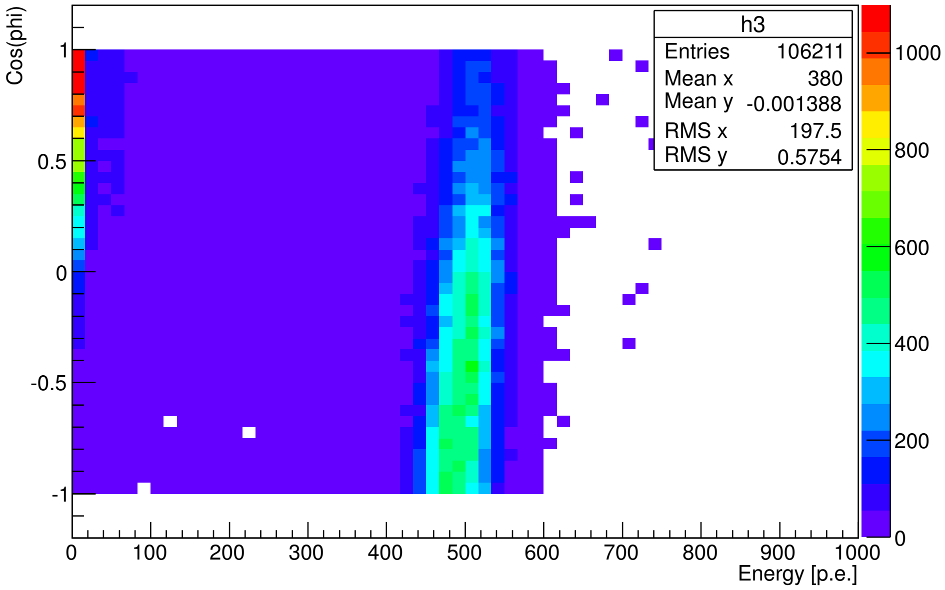

Figure 6.11: The relation between neutron energy and $\cos\phi$.

on the energy cut efficiency caused by the difference on the energy leakage is negligible.

6.4 Lifetime cut efficiency

The lifetime cut efficiency, ε_t, is obtained by Monte-Carlo method. The correlated uncertainty of this quantity is 0.75% which is obtained by the relative difference between Monte-Carlo result and data. For the uncorrelated uncertainty, we consider the neutron capture time τ approximated by:

$$\frac{1}{\tau} = \frac{\upsilon}{\lambda} = \upsilon n_i \sigma_i(\upsilon), \tag{6.17}$$

where υ is the neutron velocity and λ is the neutron mean free path. The mean free path of a particle is related to the number density of nucleus, n_i, and its cross section, σ, at υ. These are the sources for the uncorrelated uncertainty of ε_t.

The chemical measurement gives the density difference of LS and the differences on the fractions of hydrogen and carbon between different ADs. The former is less than 0.1% which contributes to the uncorrelated uncertainty and the later is less than 0.3%. In addition, the timing precision of the electronics contributes 0.1% to the uncorrelated

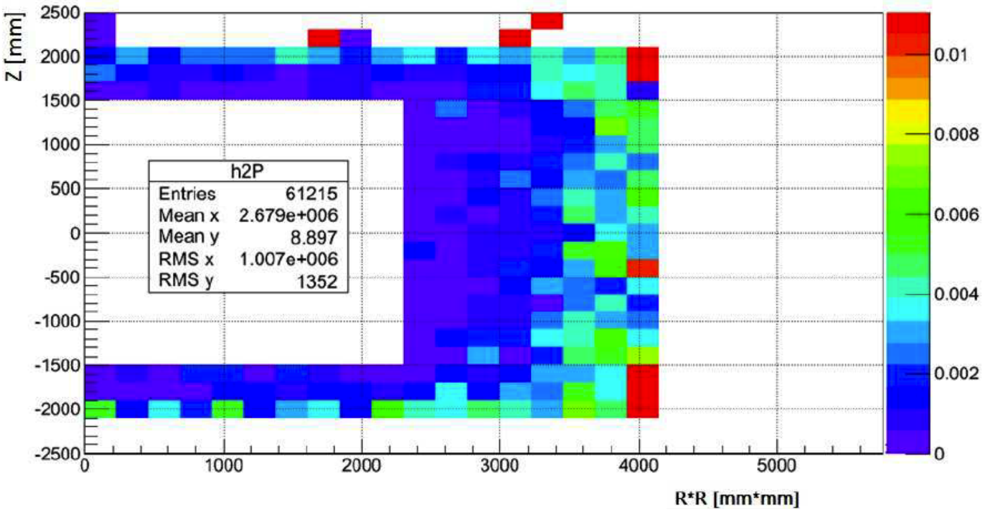

Figure 6.12: MC study of the leakage fraction of LS IBD events after delayed energy cut.

uncertainty. This result, as shown in Figure 6.17, has been validated with the ^{214}Bi. Hence, the total uncorrelated uncertainty for the lifetime cut efficiency is 0.14%.

6.5 Distance cut efficiency

The distance cut efficiency is calculated from the Figure 5.6, which is defined as

$$\varepsilon_d = \frac{N[0,l]}{N(all)}, \tag{6.18}$$

where l is the cut value, $N[0,l]$ is the number of events between 0 and l mm, and $N(all)$ is the total numbers between 0 and 2000 mm.

Figure 6.13 shows the results for each AD. Figure 6.14 is the comparison between near and far site ADs. Figure 6.15 and Figure 6.16 show the difference between AD1 and other ADs and between near and far site detectors. The uncorrelated uncertainty was estimated to be 0.4%, which comes from the uncertainty of the vertex reconstruction bias and the resolution.

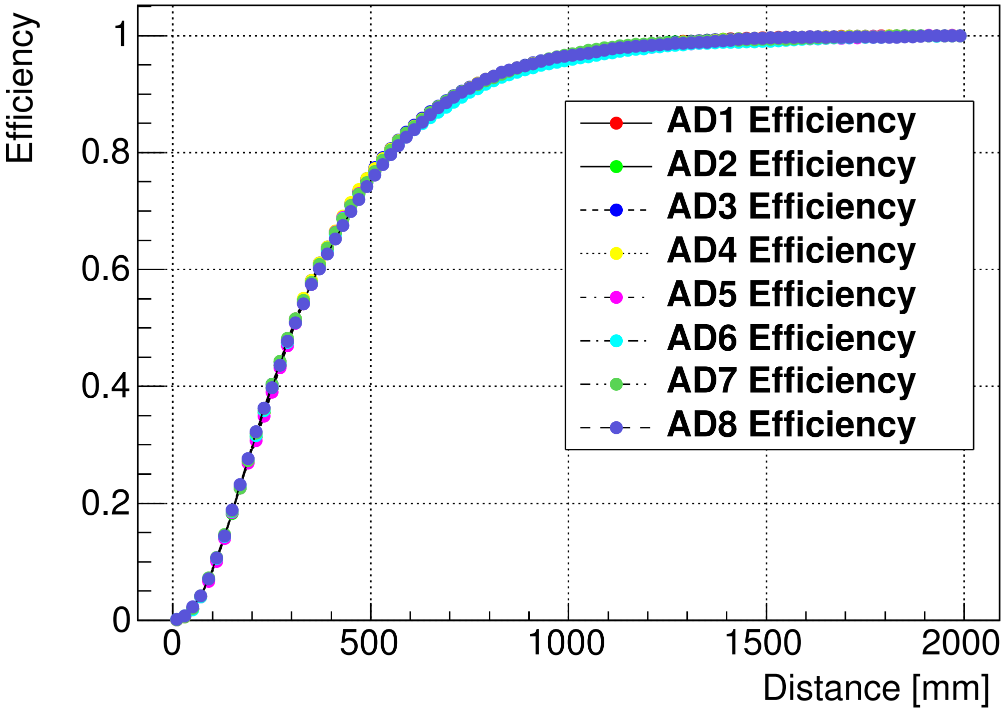

Figure 6.13: The distance cut efficiency for each detector.

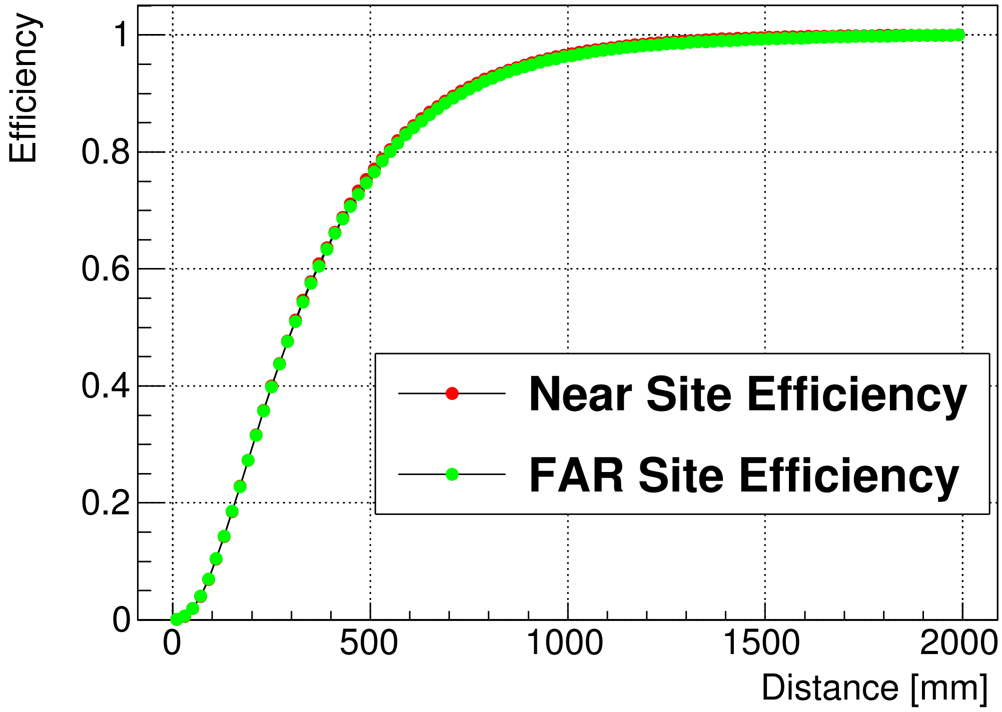

Figure 6.14: The distance cut efficiency at near and far detectors.

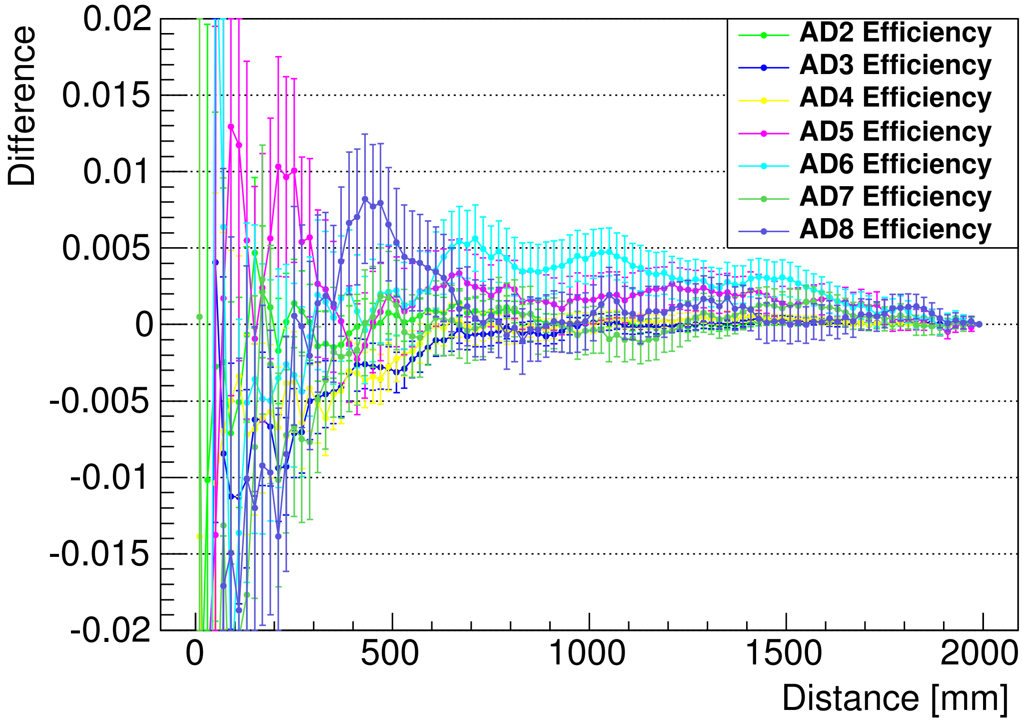

Figure 6.15: The acceptance difference of distance cut efficiency between AD1 and other ADs.

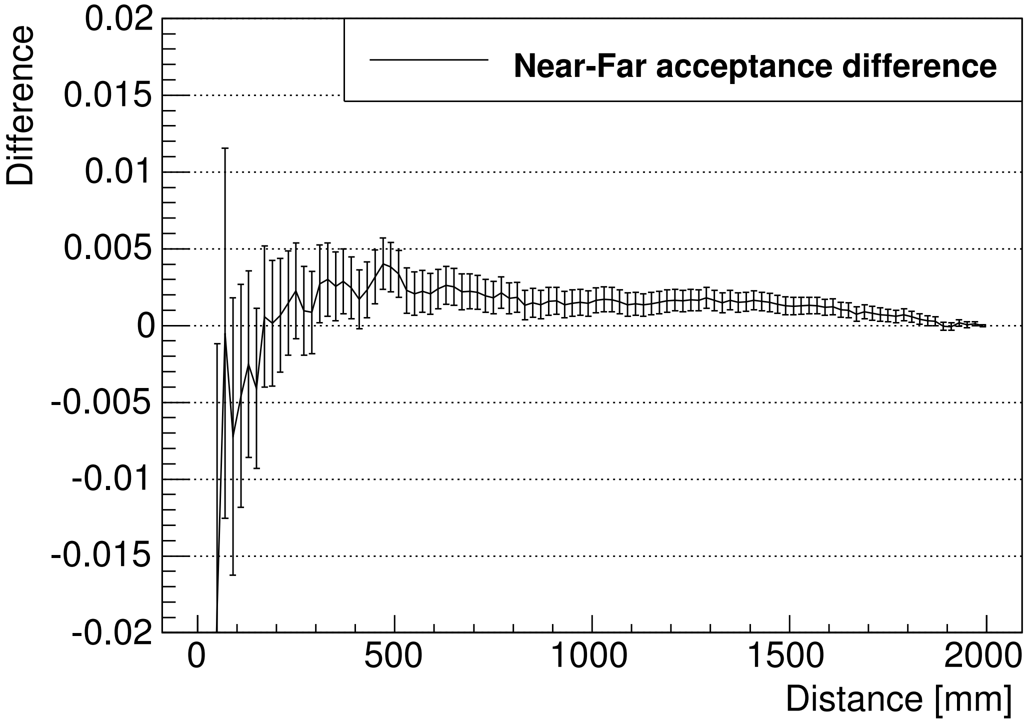

Figure 6.16: The acceptance difference of distance cut efficiency for near and far sites.

6.6 Verification by the radioactive nuclide: $^{214}Bi -^{214} Po$

The $^{214}Bi -^{214} Po$ is one of environmental radioactive backgrounds. It comes from ^{238}U and ^{222}Rn decays. ^{214}Bi and ^{214}Po emit β^- and α, respectively. These form the prompt-delayed coincidence pair. The lifetime is 164 μs. The event selection for $^{214}Bi -^{214} Po$ are:

- Prompt energy (β^-): 1.4 MeV $< E <$ 3.4 MeV.
- Delayed energy (α): 0.8 MeV $< E <$ 1.2 MeV.
- Event selection window: 10 $\mu s < T_c <$ 400 μs.
- Distance between prompt and delayed signals $<$ 0.5 m.

The signals locate in the low energy range so the accidental subtraction and distance cuts are needed. The lifetime cut efficiency and distance cut efficiency can be calculated by the same methods in IBD case. Figures 6.17 and 6.18 show the difference of lifetime cut efficiency between each AD and AD1 and between near and far detectors. The differences between the lifetime cut efficiencies are less than 0.0014. For far site detectors, the statistics is less than near site detectors, so the difference between the lifetime cut efficiencies are slightly higher than 0.0014. However, the differences between near detectors and far detectors are still less than 0.0014.

On the other hand, there is a good verification for distance cut efficiency by using the $^{214}Bi -^{214} Po$ source. As shown in Figures 6.19, 6.20, 6.21 and 6.22, the differences in distant cut efficiencies are less than 0.005 difference and agree with the IBD results.

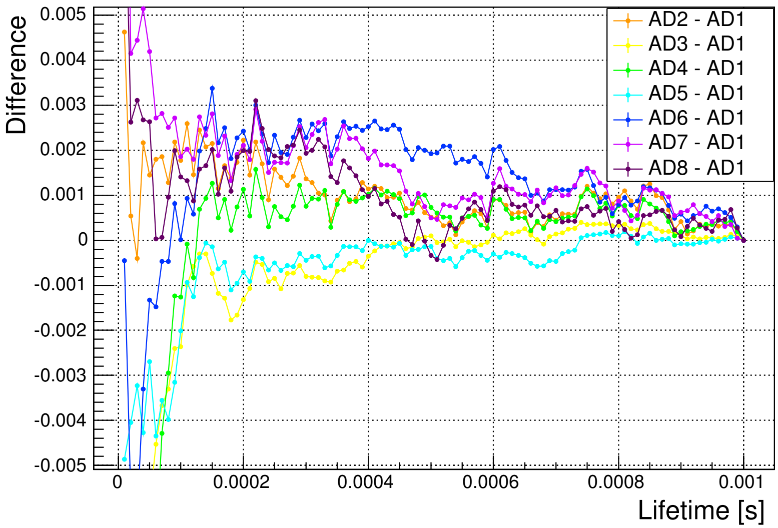

Figure 6.17: Difference of lifetime cut efficiency of $^{214}Bi -^{214} Po$ source between each AD and AD1.

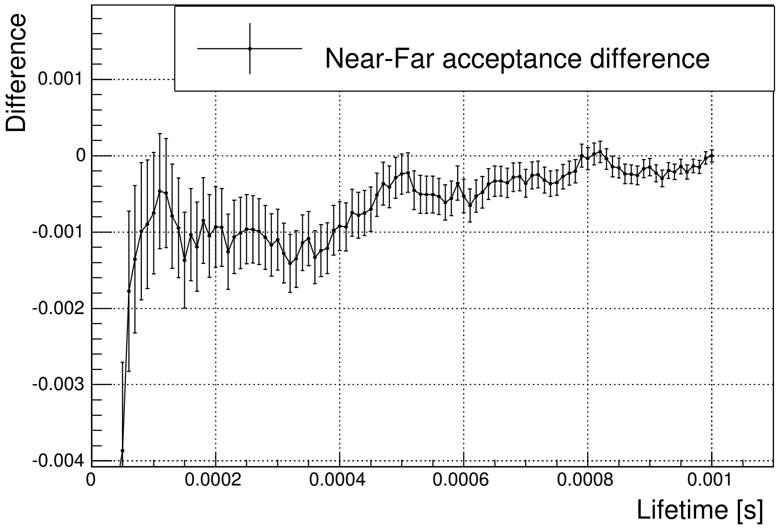

Figure 6.18: Difference of average lifetime cut efficiency of $^{214}Bi -^{214} Po$ source between near site ADs and far site ADs.

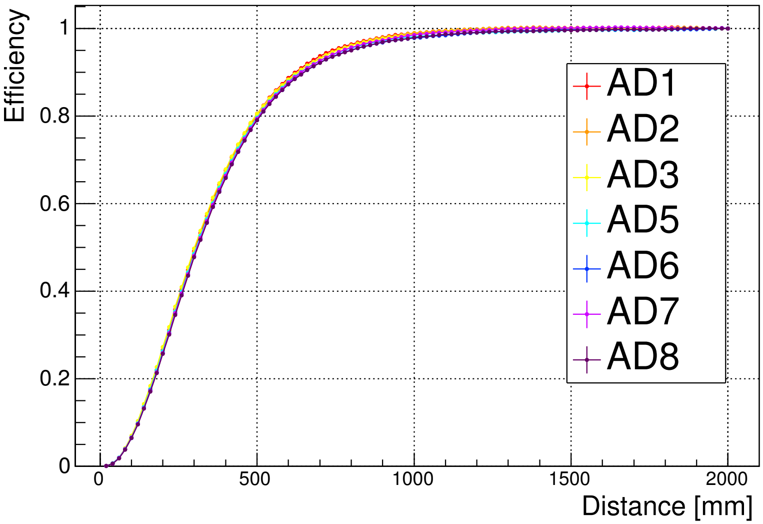

Figure 6.19: Distance cut efficiency of $^{214}Bi - ^{214}Po$ source between each AD.

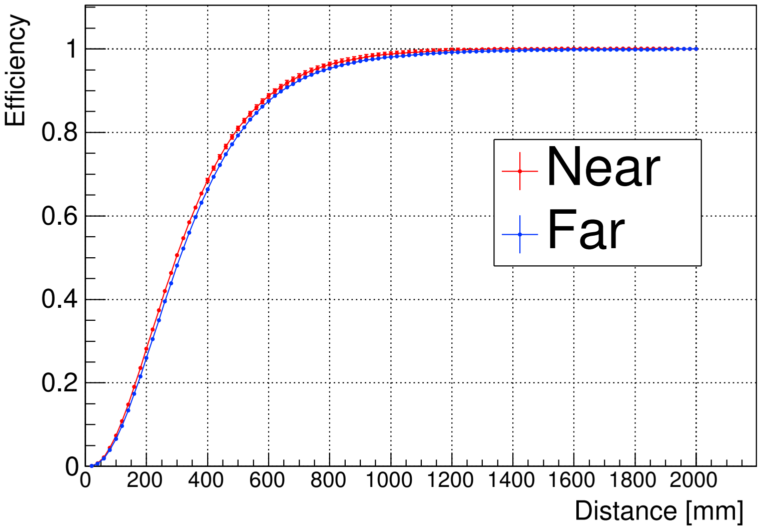

Figure 6.20: Distance cut efficiency of $^{214}Bi - ^{214}Po$ source between near site ADs and far site ADs.

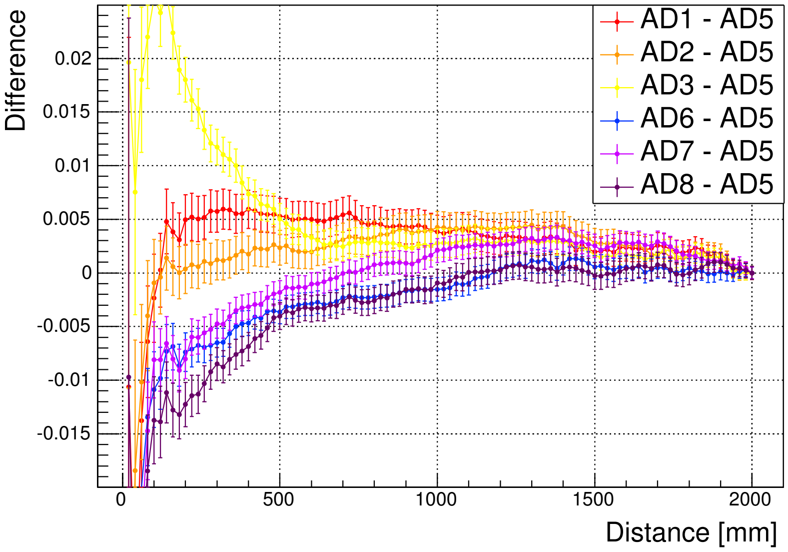

Figure 6.21: Difference of distance cut efficiency of ${}^{214}Bi - {}^{214}Po$ source between each AD and AD5.

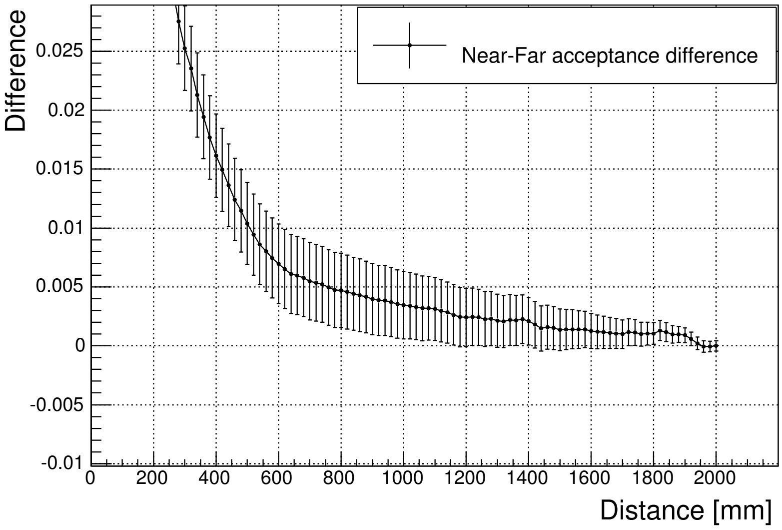

Figure 6.22: Difference of distance cut efficiency of ${}^{214}Bi - {}^{214}Po$ source between near site ADs and far site ADs.

Chapter 7

Neutrino Oscillation Measurement

The observed rate of IBD candidates and the predicted IBD rate are used to extract the mixing angle θ_{13} by the Pearson's chi-squared test, which also known as the chi-squared goodness-of-fit test. This analysis method is called "rate analysis".

The rate measurement was discussed in Chapter 4, and the backgrounds are discussed Chapter 5. The detection efficiencies are estimated in Chapter 6. These results are summarized in Table 7.1 and Table 7.2. Figure 7.1 shows the IBD rate for each detector. The predicted IBD rate from the reactors are discussed in this Chapter. After IBD event prediction, the chi-squared model is introduced and the mixing angle θ_{13} is extracted.

7.1 Signal prediction

For a simplified case with only one reactor and one detector, the total number of IBD events observed can be expressed as:

$$N_{IBD} = \sum_{i}^{NBins} \sigma_i \cdot \phi_i \cdot \frac{1}{4\pi l^2} \cdot t \cdot N_P \cdot f_H \cdot \varepsilon, \tag{7.1}$$

where σ is the IBD reaction cross section; ϕ is the neutrino flux from the reactor which is energy dependent and suppressed by the baseline, l, summarized in Table 7.3; t is the data-taking time, shown in Table 7.1; N_P is the number of protons; f_H is the fraction of captures on hydrogen and ε is the detection efficiency.

The neutron capture on hydrogen process can occur in GdLS, LS and Acrylic regions.

	AD1	AD2	AD3	AD4	AD5	AD6	AD7	AD8
Fulltime (d)	565.4361	565.4361	568.0185	568.0185	562.4139	562.4139	562.4139	562.4139
Livetime (d)	449.4485	447.8241	473.3918	483.4036	551.9756	551.9621	551.8261	553.1068
R_μ (Hz)	200.3232	200.3233	150.0765	150.0866	15.7478	15.7479	15.7478	15.7478
Veto (d)	115.99	117.61	94.63	84.61	10.44	10.45	10.59	9.31
ε_μ	0.7949	0.7920	0.8334	0.8510	0.9814	0.9814	0.9812	0.9835
ε_m	0.9844	0.9845	0.9846	0.9908	0.9844	0.9841	0.9839	0.9912
$\varepsilon_\mu \varepsilon_m$	0.7825	0.7797	0.8206	0.8432	0.9661	0.9658	0.9654	0.9748
Candidates	217613±466	219721±469	208606±457	136718±370	56880±238	56106±237	59230±243	38037±195
Acc. Bkg.	26227.61±49.37	25736.30±48.47	25318.10±42.87	16364.88±28.51	29894.74±21.36	30039.52±21.55	32206.76±22.76	20430.99±16.25
R_{ACC} (1/d)	59.28 ± 0.11	58.37 ± 0.11	54.32 ± 0.09	34.17 ± 0.06	55.02 ± 0.04	55.30 ± 0.04	59.32 ± 0.04	37.27 ± 0.03
Can.-Acc.	191385±469	193985±471	183288±459	120353±371	26985±255	26066±253	27023±260	17606±204
R_{FastN} (1/d)	2.18 ± 0.76	2.18 ± 0.76	2.02 ± 1.03	1.32 ± 0.67	0.14 ± 0.06	0.14 ± 0.06	0.14 ± 0.06	0.09 ± 0.04
R_{Li9} (1/d)	1.70 ± 0.73	1.70 ± 0.73	1.46 ± 0.72	0.95 ± 0.47	0.15 ± 0.05	0.15 ± 0.05	0.15 ± 0.05	0.10 ± 0.03
R_{AmC} (1/d)	0.08 ± 0.04	0.08 ± 0.04	0.08 ± 0.04	0.05 ± 0.03	0.03 ± 0.02	0.03 ± 0.02	0.03 ± 0.02	0.02 ± 0.01
IBD	189632±662	192238±662	181631±744	119242±540	26809±259	25892±256	26849±264	17492±206
R_{IBD} (1/d)	428.61 ± 1.50	436.03 ± 1.50	389.69 ± 1.60	248.96 ± 1.13	49.34 ± 0.45	47.67 ± 0.45	49.45 ± 0.46	31.91 ± 0.36

Table 7.1: Summary of the hydrogen capture data sample.

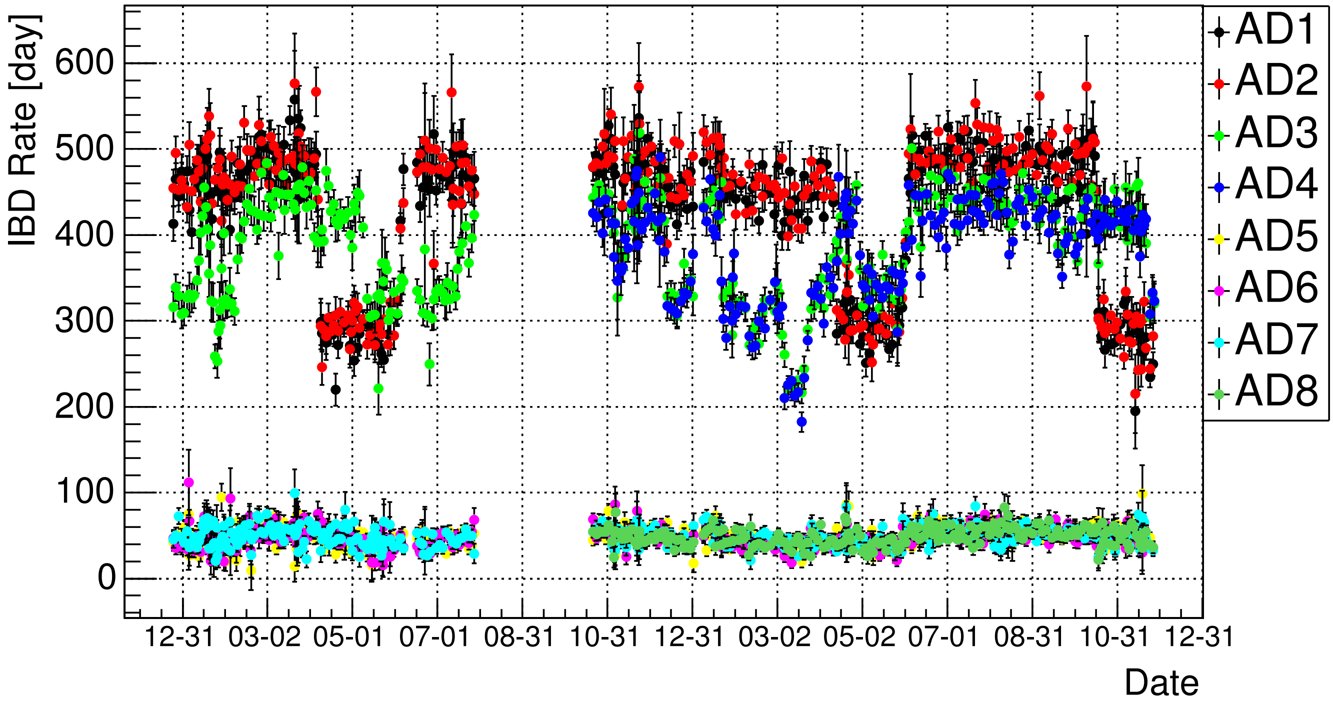

Figure 7.1: IBD rate for each detector from Dec 24, 2011 to Nov 30, 2013.

	GdLS	LS	Acrylic
Capture fraction	0.1502	0.9580	0.0288
ε_{ep}	0.9518 ± 0.0128(cor.) ± 0.0048 (unc.)	0.9297 ± 0.0145(cor.) ± 0.0046 (unc.)	
ε_{ed}	0.9695 ± 0.0018(cor.) ± 0.0048 (unc.)	0.6799 ± 0.0023(cor.) ± 0.0034 (unc.)	
ε_{T}	0.9889 ± 0.0014	0.8403 ± 0.0014	
ε_{d}	0.7527 ± 0.004		0.0046

Table 7.2: Summary of the efficiencies.

The fraction of neutron captured by hydrogen and the detection efficiency in the above three zones are different. Therefore, the above formula is changed into

$$N_{IBD} = \sum_{i}^{NBins} \sigma_i \cdot \phi_i \cdot \frac{1}{4\pi l^2} \cdot t \cdot \sum_{v}^{GdLS,LS,Acry.} (N_{P,v} \cdot f_{H,v} \cdot \varepsilon_v), \tag{7.2}$$

where the N_P, f_H and ε all carry the volume subscript, v.

For the real case, there are 6 reactors which contribute to IBD events detected by each detector. Hence the predicted number of IBD events can be written as

$$N_{predict} = \sum_{r}^{Reactors} N_{IBD,r}. \tag{7.3}$$

Combining Eq (6.1) and Eq (7.1), (7.2) and (7.4), the number of IBD events is rewritten as,

$$N_{predict} = \sum_{r}^{Reactors} \sum_{i}^{NBins} \sigma_{r,i} \cdot \phi_{r,i} \cdot \frac{1}{4\pi l_{r,i}^2} \cdot t \cdot \left\{ \varepsilon_\mu \cdot \varepsilon_m \cdot \left[\sum_{v}^{GdLS,LS,Acry.} N_{P,v} \cdot f_{H,v} \cdot \varepsilon_{ep,v} \cdot \varepsilon_{ed,v} \cdot \varepsilon_{t,v} \right] \cdot \varepsilon_d \right\} \tag{7.4}$$

	D1	D2	L1	L2	L3	L4
AD 1	362.38	371.763	903.466	817.158	1353.62	1265.32
AD 2	357.94	368.414	903.347	816.896	1354.23	1265.89
AD 3	1332.48	1358.15	467.574	489.577	557.579	499.207
AD 4	1337.43	1362.88	472.971	495.346	558.707	501.071
AD 5	1919.63	1894.34	1533.18	1533.63	1551.38	1524.94
AD 6	1917.52	1891.98	1534.92	1535.03	1554.77	1528.05
AD 7	1925.26	1899.86	1538.93	1539.47	1556.34	1530.08
AD 8	1923.15	1897.51	1540.67	1540.87	1559.72	1533.18

Table 7.3: The baseline [m] between ADs and reactor cores. Reactors are grouped into three reactor complex: Daya Bay(D1,D2), Ling Ao I (L1,L2) and Ling Ao II(L3, L4)

f_H, hydrogen capture fraction

Both of $f_{H,GdLS}$ and $f_{H,LS}$ are obtained by MC simulations. The former, $f_{H,GdLS}$, is $(15.63 \pm 0.12)\%$ and the later, $f_{H,LS}$, is $(95.81 \pm 0.006)\%$, as shown in Table 6.1.

Cross section

The differential cross section of inverse beta decay process is from Ref. [34],

$$\frac{\mathrm{d}\sigma}{\mathrm{d}\cos\theta} = \frac{\sigma_0}{2}[(f^2+3g^2)+(f^2-g^2)\upsilon_e^{(1)}\cos\theta]E_e^{(1)}p_e^{(1)} - \frac{\sigma_0}{2}\left[\frac{\Gamma}{M}\right]E_e^{(0)}p_e^{(0)}, \tag{7.5}$$

where

$$\begin{aligned} \Gamma &= 2(f+f_2)g\left[(2E_e^{(0)}+\Delta)(1-\upsilon_e^{(0)}\cos\theta)-\frac{m_e^2}{E_e^{(0)}}\right] \\ &+ (f^2+g^2)\left[\Delta(1-\upsilon_e^{(0)}\cos\theta)+\frac{m_e^2}{E_e^{(0)}}\right] \\ &+ (f^2+3g^2)\left[(E_e^{(0)}+\Delta)\left(1-\frac{1}{\upsilon_e^{(0)}}\cos\theta\right)-\Delta\right] \\ &+ (f^2-g^2)\left[(E_e^{(0)}+\Delta)\left(1-\frac{1}{\upsilon_e^{(0)}}\cos\theta\right)-\Delta\right]\upsilon_e^{(0)}\cos\theta, \end{aligned} \tag{7.6}$$

$f = 1$, $g = 1.26$, $\Delta = M_n - M_p$, $E_e^{(0)} = E_\nu - \Delta$,

$$E_e^{(1)} = E_e^{(0)} \left[1 - \frac{E_\nu}{M}(1 - v_e^{(0)} \cos\theta) \right] - \frac{y^2}{M}, \tag{7.7}$$

and $y^2 = (\Delta^2 - m_e^2)/2$.

The cross section of inverse beta decay process is shown in Figure 7.2, which is given by integrating Eq. 7.5.

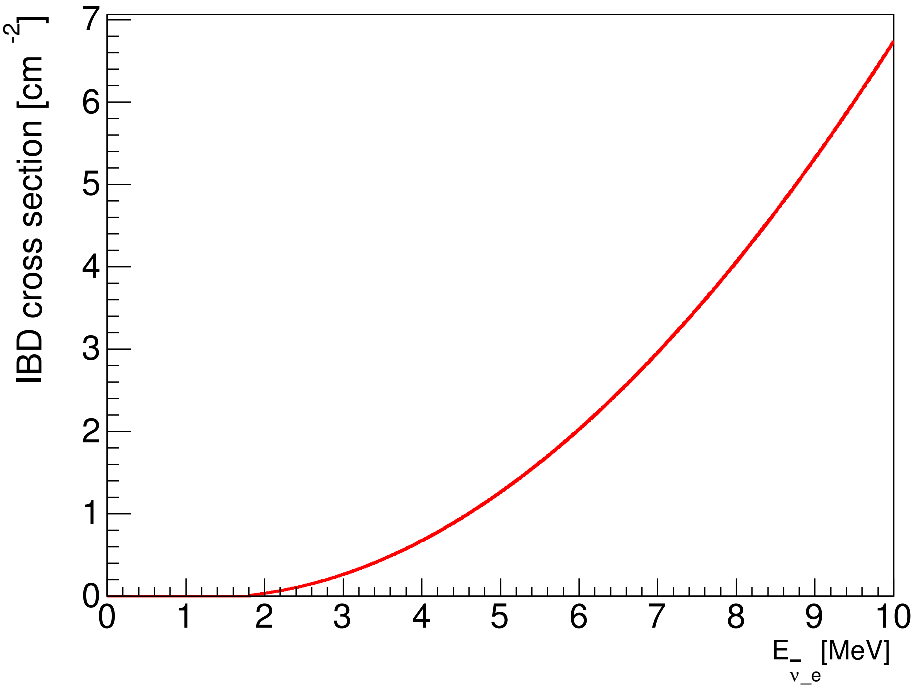

Figure 7.2: The cross section of inverse beta decay.

Flux

Generally, a fresh fuel rod contains four main fissile nuclei, ^{235}U, ^{238}U, ^{239}Pu and ^{241}Pu. On average, each fission releases about 200 MeV of energy and six neutrinos. For a typical reactor (3 GW$_{\text{th}}$), it emits $(5 \sim 6) \times 10^{20}$ antineutrinos per second.

In the real case, the neutrino flux from the reactor is time dependent. The instantaneous anti-neutrino flux $\phi(E_\nu)$ for a reactor core is

$$\phi(E_\nu) = \frac{W_{th}}{\sum_i (f_i/F) e_i} \sum_i^{isotopes} \left(\frac{f_i}{F} \right) s_i(E_\nu), \tag{7.8}$$

where W_{th} is the reactor thermal power, for Daya Bay experiment is about 2.85 $\mathrm{GW_{th}}$, f_i/F is the fractional contribution for each isotope, e_i is the average energy released by each isotope in a fission, as shown in Table 7.4, and $s_i(E_\nu)$ is the average energy spectrum from each isotope in a fission. There are many experimental groups to measure the anti-neutrino spectrum for each isotope, such as ILL [35] [36] [37], Bugey3 [38] and Huber [39]. For the theoretical calculation, Vogel and Mueller et al. [40] have a good prediction on ^{238}U.

To precisely determine the neutrino flux, one needs the instantaneous fission fraction and the thermal power information. Such information is provided by the power plant company. During the analysis process, this information is blinded.

	^{235}U	^{238}U	^{239}Pu	^{241}Pu
Fraction of Isotope	64 %	8 %	25 %	3 %
Energy per Fission [MeV]	201.92 ±0.46	205.52±0.96	209.99±0.60	213.60 ±0.65

Table 7.4: The fraction and energy per fission of each isotope for the fuel rod [41].

Number of target protons

The number of target protons is calculated by $N_{TP} = m_{target} \cdot N_P$, where m_{target} is the target mass. Table 7.5 shows the target mass of GdLS and LS for each AD. These are recorded in Daya Bay Target Proton Service. During the liquid filling, there were measured by a Coriolis meter. N_P is the proton density and defined by

$$N_P = \frac{f_H}{m_H} \cdot N_A, \tag{7.9}$$

where N_A is Avogadro's Number, f_H is the hydrogen mass fraction and $m_H = 1.00794\ g/mol$ is the average proton mass.

	$m_{target,GdLS}$	$N_{TP,GdLS}$	$m_{target,LS}$	$N_{TP,LS}$
AD1	19941±0.9	1.42957029e30	21573.5±42	1.53517025e30
AD2	19966±0.9	1.43136254e30	21519.6±42	1.53133474e30
AD3	19891± 3	1.42584241e30	21587.2±42	1.53614515e30
AD4	19944±	1.42978536e30	21499.9±	1.52637488e30
AD5	19913±1	1.42756297e30	21566.2±42	1.53465079e30
AD6	19991±1.9	1.43301141e30	21408.8±42	1.52345020e30
AD7	19892±0.9	1.42598579e30	21652.6±42	1.54079902e30
AD8	19931	1.42885339e30	21524.5	1.52812541e30

Table 7.5: The target mass [kg] for each AD.

Volumn	Proton density ($10^{25} protons/kg$)
GdLS	7.169±0.034
LS	7.116±0.043
Acrylic	4.78

Table 7.6: Proton density.

7.2 Extraction of θ_{13}

The χ^2 function with the correlated systematic errors is quoted from Ref. [23] and the form is

$$\chi^2 = \sum_{d=1}^{N_{AD}} \frac{[M_d - T_d(1 + \varepsilon + \sum_r \omega_r^d \alpha_r + \varepsilon_d) - B_d(1 + \eta_d)]^2}{(\sigma_d^M)^2 + (\sigma_d^B)^2} + \sum_r \frac{\alpha_r^2}{\sigma_r^2} + \sum_{d=1}^{N_{AD}} \left(\frac{\varepsilon_d^2}{\sigma_d^2} + \frac{\eta_d^2}{(\sigma_d^B)^2} \right), \tag{7.10}$$

where M_d are the measured IBD candidates of the dth AD with accidental background subtracted, B_d is the sum of other background, σ_d^M is the corresponding error for M_d, σ_d^B error for B_d, T_d is the prediction from neutrino flux, proton number, cross section, efficiency, and neutrino oscillation parameter etc. σ_r is the uncorrelated reactor uncertainty, σ_d is the uncorrelated uncertainty of the detection efficiency which is the quadratic sum of all uncorrelated uncertainties of the efficiency. The parameter σ_d^B is the quadratic sum of the background uncertainties. The corresponding pull parameters are (α_r,ε_d and η_d). The detector- and reactor-related correlated uncertainties were not included in the analysis. The absolute normalization ε was determined from the fit to the data. The parameter ω_r^d is the fraction of IBD event contribution from the rth reactor to the dth AD determined by baselines and reactor fluxes. In all these parameters, only σ_d^M and σ_d are larger than the nGd analysis. σ_d^M is limited by the accidental background and statistics. σ_d may be

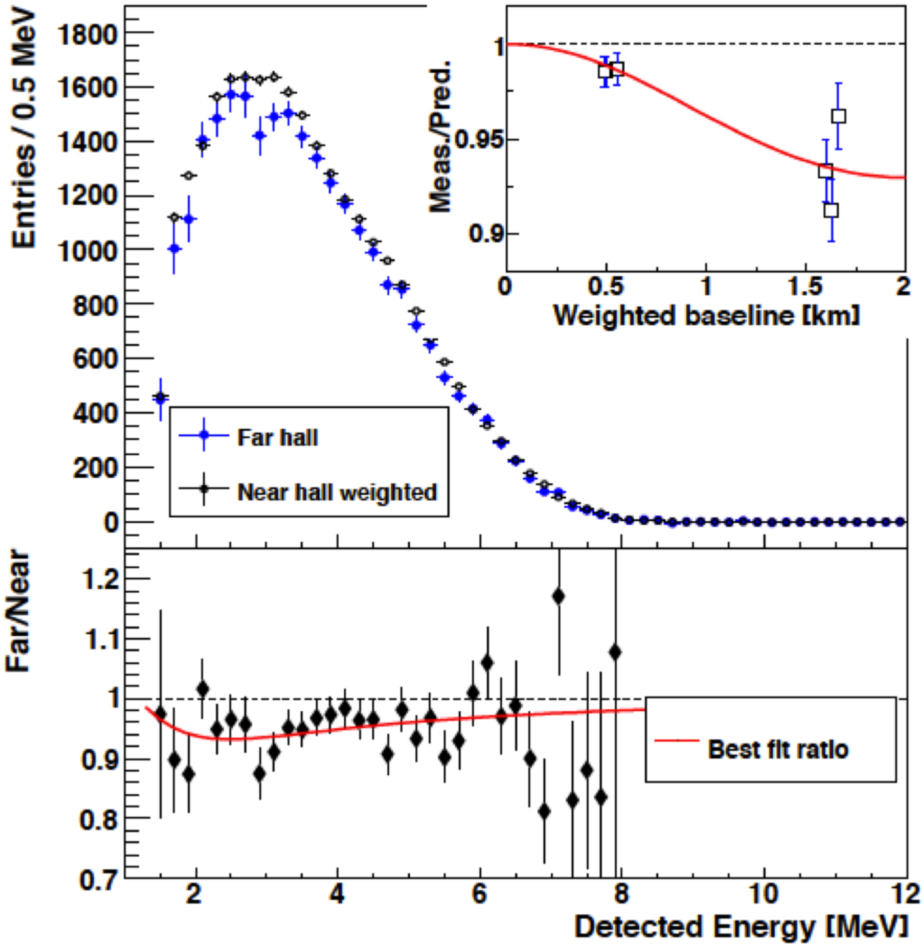

Figure 7.3: Top: The detected prompt energy spectrum by the far hall ADs (blue) and the expected prompt energy spectrum from extrapolating the near hall measurements without the effect of neutrino oscillation (open circle). Bottom: The near-to-far ratio with best fit θ_{13}. Insert: The ratio of the measured to the predicted rates in each AD.

improved by further studies.

Results

Using the analysis package, *MINUIT*, to fit this model with the six-detector period (Dec 24, 2011 to July 28, 2012), the best-fit value for θ_{13} is

$$\sin^2 2\theta_{13} = 0.083 \pm 0.018,\ \ \chi^2/ndf = 4.6/4. \tag{7.11}$$

where $|\Delta m^2_{31}|$ is taken from MINOS [18]. The near-to-far ratio with the best fit θ_{13} is shown in Figure 7.3.

In nH fit, if only statistical uncertainties are considered, the uncertainty of $\sin^2 2\theta_{13}$ in nH analysis is 0.015 which is the same as the neutron captured by Gd analysis; if one considers all uncoupled errors with respect to nGd analysis, the uncertainty of $\sin^2 2\theta_{13}$ is 0.017.

The mixing angle measurement by combining nH and nGd analyses is

$$\sin^2 2\theta_{13} = 0.089 \pm 0.008. \tag{7.12}$$

By using the data from Dec 24, 2011 to Nov 30, 2013 and the updated background estimation, the preliminary result for the best-fit value of θ_{13} is

$$\sin^2 2\theta_{13} = 0.0707 \pm 0.0113,\ \ \chi^2/ndf = 5.2/4. \tag{7.13}$$

where $|\Delta m^2_{31}|$ is taken from MINOS [18].

Chapter 8

Conclusion

With the optimized baseline and functionally identical detectors and the extensive analysis efforts, the mixing angle θ_{13} has been measured precisely at Daya Bay experiment.

This study used different and independent methods to measure the mixing angle θ_{13} with the neutron captured on hydrogen signals. The clear electron anti-neutrino disappearance is observed! The best-fit value θ_{13} mixing angle is

$$\sin^2 2\theta_{13} = 0.083 \pm 0.018, \ \ \chi^2/ndf = 4.6/4. \tag{8.1}$$

where $|\Delta m^2_{31}|$ is taken from MINOS [18].

This results gives a strong confidence for the earlier results from Daya Bay.

The mixing angle measurement is improved by combining nH and nGd measurements, which gives

$$\sin^2 2\theta_{13} = 0.089 \pm 0.008. \tag{8.2}$$

Results with more statistics and the prediction on the future sensitivity

With more statistics (data set from Dec 24, 2011 to Nov 30, 2013) and the updated background estimation, the preliminary result for the best-fit value of θ_{13} is

$$\sin^2 2\theta_{13} = 0.0707 \pm 0.0113, \ \ \chi^2/ndf = 5.2/4. \tag{8.3}$$

where $|\Delta m^2_{31}|$ is taken from MINOS [18].

The current error for the Daya Bay results is dominated by the statistical uncertainty. Assuming the reactor thermal power is 2.85 GW_{th} and all the efficiencies are the same as

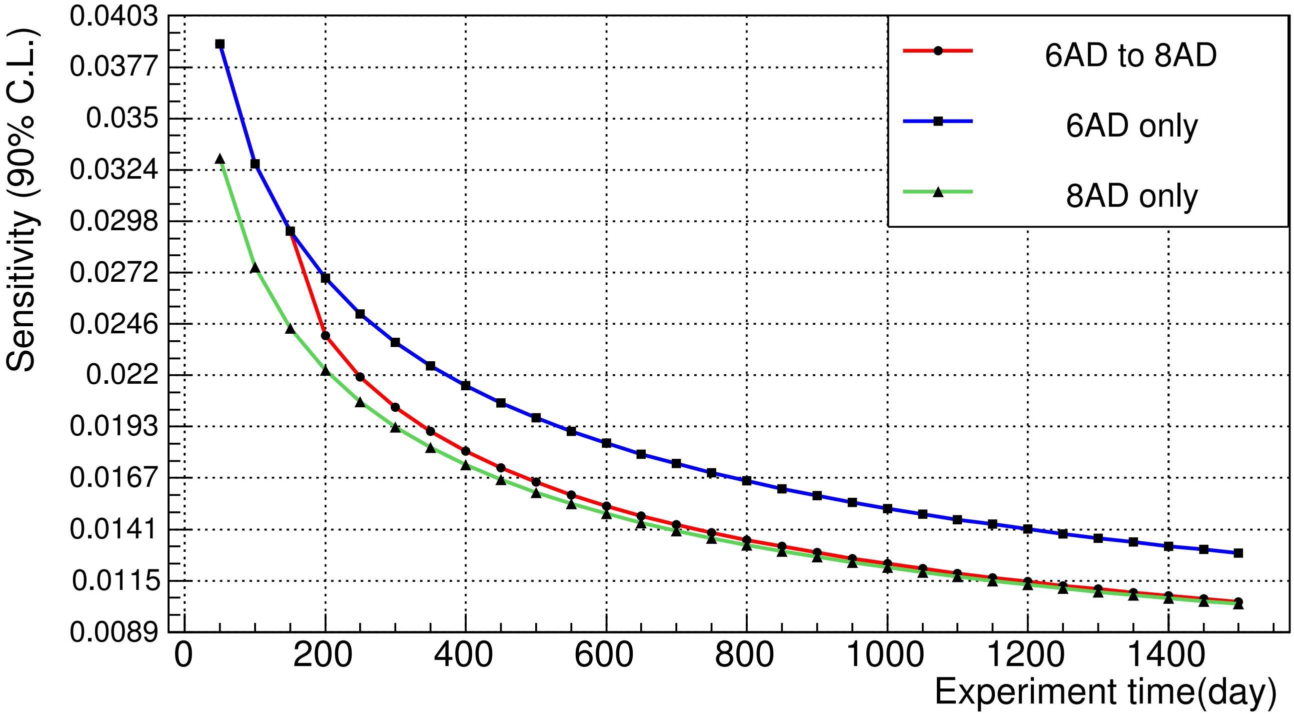

Figure 8.1: Projected sensitivity to $\sin^2 2\theta_{13}$.

before, Figure 8.1 shows the projected uncertainty.

Future plan

As it is discussed in Chapter 3, the energy distribution depends on the vertex. The energy leakage is very serious in LS region. It is worth understanding the non-uniformity in the LS region. On the other hand, the energy non-linearity also affects the energy cuts and impacts on the number of IBD events. The analysis of the missing angle θ_{13} based on the non-linearity and non-uniformity is knows as "spectral measurement" or "shape anslysis". The Daya Bay collaboration has published results on the spectral measurement with nGd signals [42]. The spectral measurement with nH signals is on the progress.

Bibliography

[1] K. Zuber, "Neutrino Physics", Second Edition, Talor & Francis(2012).

[2] John N. Bahcall, Phys. Rev. Lett., **12**, Number 11, 300-302 (16 March 1964).

[3] Raymond Davis, Jr., Phys. Rev. Lett., **12**, Number 11, 303-305 (16 March 1964)

[4] B. T. Cleveland, T. Daily, R. Davis, Jr., J. R. Distel, K. Lande, C. K. Lee, P. S. Wildenhain and J. Ullman, Astrophys. J. **496**, 505 (1998).

[5] Z. Maki, M. Nakagawa and S. Sakata, Prog. Theor. Phys. **28**, 870 (1962).

[6] Y. Fukuda *et al.* [Super-Kamiokande Collaboration], Phys. Rev. Lett. **81**, 1562 (1998) [hep-ex/9807003].

[7] C. Giunti and C. W. Kim, "Fundamentals of Neutrino Physics and Astrophysics", Oxford University Press (2007).

[8] http://pdg.lbl.gov

[9] S. Abe *et al.* [KamLAND Collaboration], Phys. Rev. Lett. **100**, 221803 (2008) [arXiv:0801.4589 [hep-ex]].

[10] P. Adamson *et al.* [MINOS Collaboration], Phys. Rev. D **82**, 051102 (2010) [arXiv:1006.0996 [hep-ex]].

[11] P. Adamson *et al.* [MINOS Collaboration], Phys. Rev. Lett. **110**, no. 17, 171801 (2013) [arXiv:1301.4581 [hep-ex]].

[12] D. S. Ayres *et al.* [NOvA Collaboration], hep-ex/0503053.

[13] `http://j-parc.jp/researcher/Hadron/en/pac_0606/pdf/p11-Nishikawa.pdf`

[14] K. Abe *et al.* [T2K Collaboration], Phys. Rev. Lett. **112**, 061802 (2014) [arXiv:1311.4750 [hep-ex]].

[15] X. Guo *et al.* [Daya-Bay Collaboration], hep-ex/0701029.

[16] F. Ardellier *et al.* [Double Chooz Collaboration], hep-ex/0606025.

[17] J. K. Ahn *et al.* [RENO Collaboration], arXiv:1003.1391 [hep-ex].

[18] P. Adamson *et al.* [MINOS Collaboration], Phys. Rev. Lett. **106**, 181801 (2011) [arXiv:1103.0340 [hep-ex]].

[19] M. Apollonio *et al.* [CHOOZ Collaboration], Eur. Phys. J. C **27**, 331 (2003) [hep-ex/0301017].

[20] Daniel A. Dwyer, Physics of the Dark Universe **Volume 4**, September 2014, Pages 31-35

[21] K. Abe *et al.* [T2K Collaboration], Phys. Rev. Lett. **107**, 041801 (2011) [arXiv:1106.2822 [hep-ex]].

[22] P. Adamson *et al.* [MINOS Collaboration], Phys. Rev. Lett. **107**, 181802 (2011) [arXiv:1108.0015 [hep-ex]].

[23] F. P. An *et al.* [DAYA-BAY Collaboration], Phys. Rev. Lett. **108**, 171803 (2012) [arXiv:1203.1669 [hep-ex]].

[24] F. P. An *et al.* [DAYA-BAY Collaboration], Nucl. Instr. Meth A **685**, 78-97 (2012) [arXiv:1202.6181 [hep-ex]].

[25] Raymond Hei Man Tsang, PhD Thesis,“Discovery of non-zero neutrino mixing angle θ_{13} using Daya Bay Antineutrino Detectors”, California Institute of Technology Pasadena, California (2013).

[26] E. H. Bellamy, G. Bellettini, F. Gervelli, M. Incagli, D. Lucchesi, C. Pagliarone, F. Zetti and Y. .Budagov *et al.*, Nucl. Instrum. Meth. A **339**, 468 (1994).

[27] F. P. An *et al.* [Daya Bay Collaboration], Chin. Phys. C **37**, 011001 (2013) [arXiv:1210.6327 [hep-ex]].

[28] Zeyuan Yu et al., Anti-neutrino Detector Energy Response, Daya Bay DocDB-7314, 2011.

[29] Yasuhiro Nakajima, Vertex reconstruction using charge templates for AdSimple reconstruction package, Daya Bay DocDB-7536, 2012.

[30] C-J Lin et al., The AdSimple Reconstruction, Daya Bay DocDB-7334-v2, 2013.

[31] Bryce Richard Littlejohn, PhD Thesis,"Observation of Antineutrino Disappearance at the Daya Bay Experiment", University of Wisconsin-Madison (2012).

[32] J. Yu, Z. Wang and S. Chen, arXiv:1301.5085 [physics.ins-det].

[33] Evaluated Nuclear Data File (ENDF): https://www-nds.iaea.org/exfor/endf.htm

[34] P. Vogel and J. F. Beacom, Phys. Rev. D **60**, 053003 (1999) [hep-ph/9903554].

[35] K. Schreckenbach, G. Colvin, W. Gelletly and F. Von Feilitzsch, Phys. Lett. B **160**, 325 (1985).

[36] F. Von Feilitzsch, A. A. Hahn and K. Schreckenbach, Phys. Lett. B **118**, 162 (1982).

[37] A. A. Hahn, K. Schreckenbach, G. Colvin, B. Krusche, W. Gelletly and F. Von Feilitzsch, Phys. Lett. B **218**, 365 (1989).

[38] B. Achkar, R. Aleksan, M. Avenier, G. Bagieu, J. Bouchez, R. Brissot, J. F. Cavaignac and J. Collot *et al.*, Phys. Lett. B **374**, 243 (1996).

[39] P. Huber, Phys. Rev. C **84**, 024617 (2011) [Erratum-ibid. C **85**, 029901 (2012)] [arXiv:1106.0687 [hep-ph]].

[40] P. Vogel, G. K. Schenter, F. M. Mann and R. E. Schenter, Phys. Rev. C **24**, 1543 (1981).

[41] V. I. Kopeikin et al. Reactor as a source of antineutrinos: Thermal fission energy, Physics of Atomic Nuclei, **67**(10):1892, 2004.

[42] F. P. An *et al.* [Daya Bay Collaboration], Phys. Rev. Lett. **112**, 061801 (2014) [arXiv:1310.6732 [hep-ex]].